Helmholtz-Zentrum Dresden-Rossendorf (HZDR)

Coordination of Trivalent Lanthanum and Cerium, and Tetravalent Cerium and Actinides (An = Th(IV), U(IV), Np(IV)) by a 4-Phosphoryl 1H-Pyrazol-5-olate Ligand in Solution and the Solid State

Zhang, J.; Wenzel, M.; Schnaars, K.; Hennersdorf, F.; Schwedtmann, K.; März, J.; Roßberg, A.; Kaden, P.; Kraus, F.; Stumpf, T.; Weigand, J. J.;

ARTICLE

Coordination of Trivalent Lanthanum and Cerium, and Tetravalent Cerium and Actinides (An = Th(IV), U(IV), Np(IV)) by a 4-Phosphoryl 1H-Pyrazol-5-olate Ligand in Solution and the Solid State

Jianfeng Zhang,[a] Marco Wenzel,[a] Kathleen Schnaars,[a] Felix Hennersdorf,[a] Kai Schwedtmann,[a] Juliane März,[b] André Rossberg,[b] Peter Kaden,[b] Florian Kraus,[c] Thorsten Stumpf,[b] and Jan J. Weigand*[a]

Structural investigations of three actinide(IV) 4-phosphoryl 1H-pyrazol-5-olate complexes (An = Th(IV), U(IV), Np(IV)) and their cerium(IV) analogue display the same metal coordination in the solid state. The mononuclear complexes show the metal centre in a square antiprismatic coordination geometry composed by the two O-donor atoms of four deprotonated ligands. Detailed solid state analysis of the U(IV) complex shows that in dependence of the solvent used altered arrangements are observable, resulting in a change in the coordination polyhedron of the U(IV) metal centre to bi-capped trigonal prismatic. Further, single crystal analyses of the La(III) and Ce(III) complexes show that the ligand can also act as a neutral ligand by protonation of the pyrazoyl moiety. All complexes were comprehensively characterized by NMR, IR and Raman spectroscopy. A single resonance in each of the ^{31}P NMR spectra for the La(III), Ce(III), Ce(IV), Th(IV) and Np(IV) complex indicates the formation of highly symmetric complex species in solution. Extended X-ray absorption fine structure (EXAFS) investigations provide evidence for the same local structure of the U(IV) and Np(IV) complex in toluene solution, confirming the observations made in the solid state.

Introduction

Understanding the coordination chemistry of actinides has important applications in spent nuclear fuel processing, waste disposal, and environmental monitoring to prevent the release and migration of these metal ions.[1-4] Despite numerous reports on structural analyses of actinide(IV) complexes in very recent years,[5-24] there are only very few examples focusing on a detailed investigation of their coordination in solution.[25,26] For practical applications, such as separation processes, the coordination in solution is of particular interest as it can be significantly different from that in the solid state.[27] Thus, a large variety of ligands have been studied in solvent extraction,[28] among which organophosphorous compounds,[29-33] carbamoylmethylphosphine oxides,[34] phosphoramides,[35] amides,[36-39] diglycolamides,[40, 41] functionalized ionic liquids,[42] and Schiff base ligands[43] and also acyl pyrazolones[44-46] have been applied. Those investigations always aim to achieve high strength and selectivity of the complex formation by ensuring that the donor atom types and their dispositions meet the requirements of the targeted metal.[47] In this context, acyl pyrazolone ligands have been proposed as powerful platforms for metal coordination and potential application in separation processes, but limited studies focus on the coordination of actinides.[48, 49] 4-Phosphoryl pyrazolones are promising alternatives to acyl pyrazolones, however, their coordination behaviour towards *f*-elements is essentially unknown.[50, 51]

In this contribution, we report on the synthesis of diisopropyl-(5-hydroxy-3-methyl-1-(p-tolyl)-1H-pyrazol-4-yl)phosphonate (H**L**) and its coordination behaviour towards the tetravalent lanthanide Ce(IV) and the actinides Th(IV), U(IV) and Np(IV) in the solid state and in solution. Further, solutions of the U(IV) and Np(IV) complex are examined in detail using extended X-ray absorption fine structure (EXAFS) spectroscopy. The results indicate that the structural features of actinide(IV) complexes are essentially the same both in toluene solution and in the solid state.

Results and Discussion

The synthesis of the ligand H**L** requires a three step synthesis starting with a modified *Michaelis-Arbuzov*-reaction of triisopropyl phosphite with methyl bromoacetate to the phosphorylated acetate **1**.[52] Following the protocol of *Corbel* and co-workers,[53] the β-dicarbonyl functionalized phosphonate **2** is readily obtained in an acceptable yield (66%) and subsequently converted to H**L** with *p*-tolylhydrazine hydrochloride (Scheme 1) (ESI†).[54] However, the isolated compound H**L**, obtained in 67% yield, shows only a moderate purity of 91%. All classical methods to purify this ligand, including chromatography and recrystallization, failed. Nevertheless, H**L** readily forms the stable La(III) complex [La**L**$_3$H**L**]·3CH$_3$CN·4H$_2$O (**3**·3CH$_3$CN·4H$_2$O, Fig. 1) upon reaction with LaCl$_3$·7H$_2$O in an aqueous CH$_3$CN solution in the presence of NaOH (Scheme S1, ESI†) in 96% yield. The extraction of a
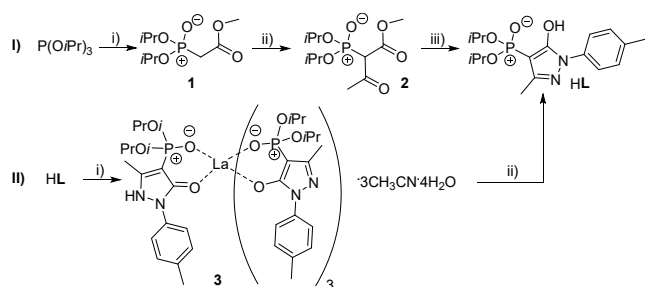
Scheme 1: **I:** Synthesis of the 4-phosphoryl pyrazolone H**L**; i) 1.05 eq. methyl bromoacetate, 120 °C, neat, 4 h, 98% with a purity of 92%; ii) 1.05 eq. MgCl$_2$, 3.5 eq. Et$_3$N, 1.95 eq. acetyl chloride, CH$_2$Cl$_2$, 20°C, 66%; iii) 1.1 eq. *p*-tolylhydrazine hydrochloride, 2.0 eq. K$_2$CO$_3$, H$_2$0, 2 h reflux, r.t. 12 h, 67% in a 91% purity; **II:** purification of H**L** *via* **3**·3CH$_3$CN·4H$_2$O and subsequent back extraction; i) LaCl$_3$·7H$_2$O, NaOH, CH$_3$CN/water, 96%; ii) CHCl$_3$/H$_2$O, HCl (0.05 M), 99%.

CHCl$_3$ solution of the complex **3**·3CH$_3$CN·4H$_2$O with 0.05 M HCl (pH = 1.3) enables the stripping of La(III) into the aqueous phase, releasing H**L** after removal of the solvent in high purity of > 99% (ESI†).

In complex **3**·3CH$_3$CN·4H$_2$O, the La(III) atom has a coordination number of eight arranged in a highly symmetric square antiprismatic coordination geometry. The La–O bond length involving the pyrazol-5-olate unit is slightly shorter (~ 0.05 Å) than that of the phosphoryl oxygen (La1–O1 2.4608(11) Å *vs.* La1–O2 2.5135(10) Å). The charge of the trivalent La is compensated by three deprotonated ligands and the square antiprismatic coordination polyhedron is completed by one neutral ligand. However, in the crystal structure of complex **3**·3CH$_3$CN·4H$_2$O all four ligands are essentially identical and the NH hydrogen atoms are seemingly disordered over all ligands with a site occupancy factor (SOF) of 0.25. Water is involved as a solvate and forms a hydrogen bond network with the nitrogen atoms of the pyrazolyl units. The donor···acceptor distances within N–H···O and O–H···O are 2.854(2) Å whereas the one in O–H···O is 2.829(4) Å. Fig. 1
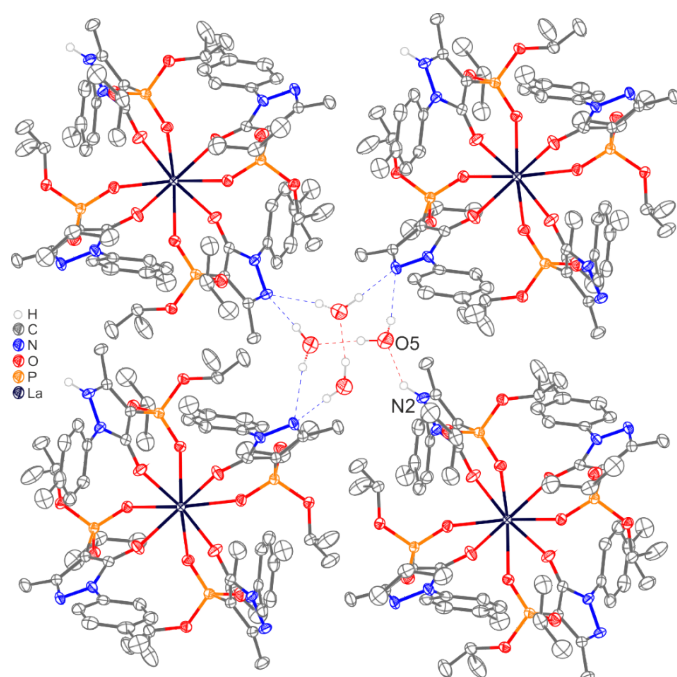

Fig. 1 Representation of hydrogen bonds between N2 and water molecules (O5) present in the crystal structure of [LaL$_3$HL]·3CH$_3$CN·4H$_2$O (**3**·3CH$_3$CN·4H$_2$O). All carbon hydrogen atoms and acetonitrile molecules are omitted for clarity; ellipsoids are drawn at 50% probability level.

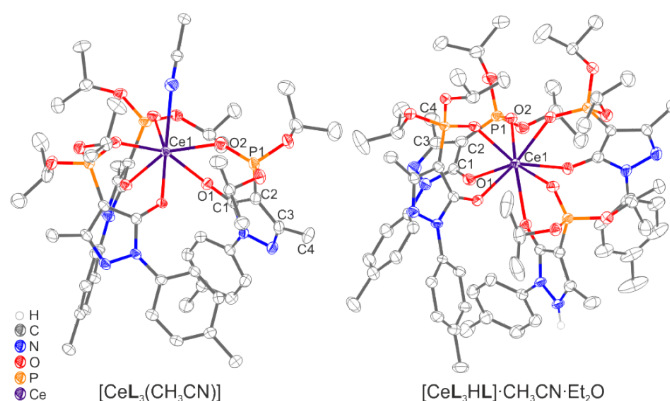**Fig. 2** Molecular structure of [Ce**L**$_3$(CH$_3$CN)] (CH$_3$CN⊂**4**) (left) and [Ce**L**$_3$H**L**]·CH$_3$CN·Et$_2$O (**5**·CH$_3$CN·Et$_2$O) (right). All carbon hydrogen atoms and solvates are omitted for clarity; ellipsoids are drawn at 50% probability level.

shows a section of the connectivity of the resulting network in the solid state.

In contrast, Ce(III) complexes can be synthesised in different metal to ligand ratios. The reaction of Ce$_2$(SO$_4$)$_3$ with three equivalents of H**L** in the presence of three equivalents of NaOH results in the formation of the Ce(III) complex [Ce**L**$_3$] (**4**) in moderate yield (ESI†). Suitable crystals for X-ray single crystal analysis of (CH$_3$CN⊂**4**) were obtained by slow evaporation of CH$_3$CN in the absence of oxygen and water (Fig. 2). Herein, the Ce(III) atom has a coordination number of seven formed by three six-membered chelate rings with the O$_2$ donor set of three deprotonated ligands and the coordination of one CH$_3$CN molecule. The Ce–O bond lengths involving the pyrazol-5-olate unit range from 2.3724(18) to 2.399(2) Å and are slightly shorter than those to the phosphoryl oxygen ranging from 2.416(2) to 2.427(2) Å. The Ce1–N7 bond length is 2.678(3) Å (Table S7, ESI†). The reaction of four equivalents of H**L** with one equivalent Ce(III) in the presence of NaOH results in the formation of the Ce(III) complex [Ce**L**$_3$H**L**] (**5**) in 85% yield. Recrystallization by slow diffusion of diethyl ether into a CH$_3$CN solution of the complex gives suitable crystals for X-ray structure analysis and yields the composition [Ce**L**$_3$H**L**]·CH$_3$CN·Et$_2$O (**5**·CH$_3$CN·Et$_2$O). The latter compound crystallised in the monoclinic space group *P*2$_1$ and the metal centre has a coordination number of eight which can be described as a distorted bicapped trigonal prismatic [MO$_8$] (M = metal) core. The increase in the coordination number results in an elongation of the Ce–O bond length. The Ce–O bonds involving the pyrazol-5-olate unit range from 2.395(3) Å to 2.500(3) Å whereas the Ce–O bond lengths of the phosphoryl oxygen are between 2.441(3) Å to 2.536(3) Å. The charge of the trivalent Ce atom is compensated by three deprotonated ligands. The fourth ligand has a NH hydrogen atom, which is involved in a N–H···N hydrogen bond with a N···N distance of 2.754(5) Å and links two molecules in a one-dimensional chain along the crystallographic *b*-axis. The co-crystallised solvent molecules CH$_3$CN and Et$_2$O are not involved in hydrogen bonds.

The syntheses of the *4f*- and *5f*-block metal(IV) complexes [M**L**$_4$] follows essentially the same procedure as for complex **3** and were performed in a variety of solvent systems with the corresponding *f*-block element salts (Ce(SO$_4$)$_2$·4H$_2$O, Th(NO$_3$)$_4$·5H$_2$O, UCl$_4$, NpCl$_4$) with moderate yields (ESI†). Suitable crystals for X-ray single crystal analysis of [Ce**L**$_4$]·2CH$_3$CN·4H$_2$O (**6**·2CH$_3$CN·4H$_2$O) were obtained by slow evaporation of aqueous CH$_3$CN after the addition of small amounts of ethanol. Suitable crystals for the diffraction experiments of [Th**L**$_4$]·3CH$_3$CN·4H$_2$O (**7**·3CH$_3$CN·4H$_2$O), [U**L**$_4$]·3CH$_3$CN·4H$_2$O

Journal Name

ARTICLE
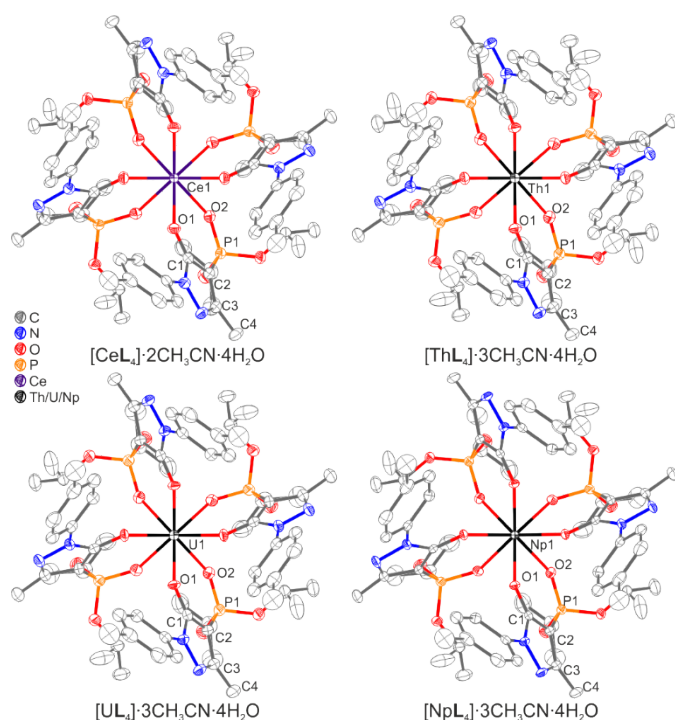
Fig. 3 Molecular structures of [CeL$_4$]·2CH$_3$CN·4H$_2$O (6·2CH$_3$CN·4H$_2$O), [ThL$_4$]·3CH$_3$CN·4H$_2$O (7·3CH$_3$CN·4H$_2$O), [UL$_4$]·3CH$_3$CN·4H$_2$O (8·3CH$_3$CN·4H$_2$O) and [NpL$_4$]·3CH$_3$CN·4H$_2$O (9·3CH$_3$CN·4H$_2$O). Hydrogen atoms and solvent molecules of crystallization are omitted for clarity; ellipsoids are drawn at 50% probability level.

(8·3CH$_3$CN·4H$_2$O) and [NpL$_4$]·3CH$_3$CN·4H$_2$O (9·3CH$_3$CN·4H$_2$O) were grown from the reaction mixture by slow evaporation. The obtained four complexes 6·2CH$_3$CN·4H$_2$O - 9·3CH$_3$CN·4H$_2$O are isostructural and crystallise in the tetragonal space group *P*4/*n* (Fig. 3). Similar to the La(III) complex 3·3CH$_3$CN·4H$_2$O and the Ce(III) complex 5·CH$_3$CN·Et$_2$O, the metal ions are octa-coordinated displaying four six-membered chelate rings between the O$_2$ donor set of four deprotonated ligands resulting in the same highly symmetric square antiprismatic [MO$_8$] core. In all complexes, the M(IV)–O bond length involving the pyrazol-5-olate unit is slightly shorter (~ 0.08 Å) than those to the phosphoryl oxygen (6·2CH$_3$CN·4H$_2$O: Ce1–O1 2.3356(14) Å *vs.* Ce1–O2 2.4173(14) Å; 7·3CH$_3$CN·4H$_2$O: Th1–O1 2.3571(15) Å *vs.* Th1–O2 2.4320(16) Å; 8·3CH$_3$CN·4H$_2$O: U1–O1 2.304(2) Å *vs.* U1–O2 2.388(2) Å; 9·3CH$_3$CN·4H$_2$O: Np1–O1 2.2990(12) Å and Np1–O2 2.3766(12) Å) but are in all cases in the typical range as evidenced by other complexes with related functional groups.[13,18,37,55] Interestingly, the bond lengths do not follow the anticipated trend of the ionic radii (CN = 8), but instead we find that the M^{IV}–O bonds both decrease in the order Th>Ce>U>Np.[56] Considering the change in the M–O bond lengths from 7·3CH$_3$CN·4H$_2$O to 8·3CH$_3$CN·4H$_2$O and 9·3CH$_3$CN·4H$_2$O an approximately equal decrease to the corresponding ionic radii (1.05 Å for Th(IV), 1.00 Å for U(IV) and 0.98 Å for Np(IV)) is observable, while the Ce–O bonds in 6·2CH$_3$CN·4H$_2$O seem to be the outliers of the series. Those are about 4 - 5 pm longer than expected and may be explained with the redox tendency of Ce(IV) (i.r. Ce(IV) = 0.97 Å *vs.* 1.14 Å for Ce(III)). However, the observed bond lengths in 5·CH$_3$CN·Et$_2$O are even longer (in 5·CH$_3$CN·Et$_2$O: Ce–O$_C$ 2.395(3) Å to 2.500(3) Å, Ce–O$_P$: 2.441(3) Å to 2.536(3) Å vs Ce–O$_C$ 2.3356(14) Å and Ce–O$_P$ 2.4173(14) Å in 6·2CH$_3$CN·4H$_2$O) indicating that no reduction to Ce^{III} occurred. The shorter M^{IV}–O bond lengths
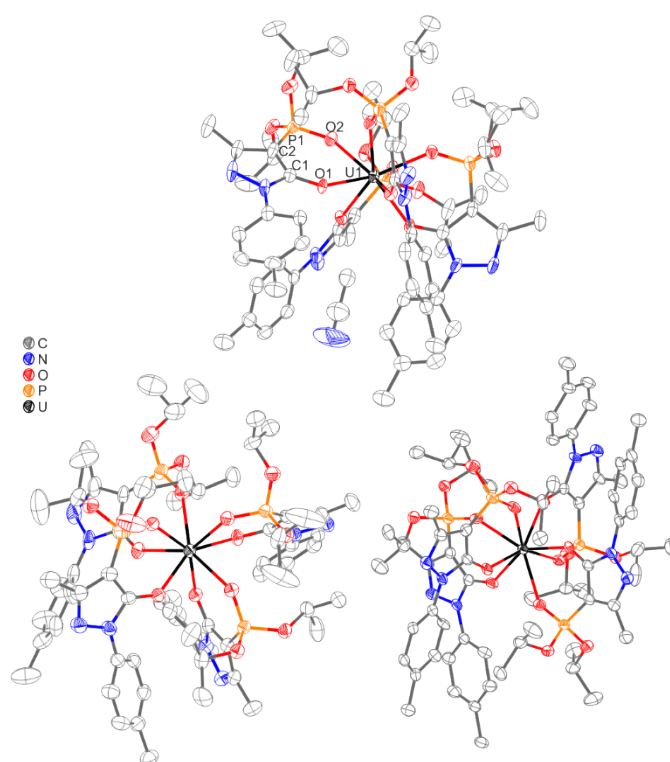
Fig. 4 Molecular structure of 8·3CH$_3$CN·4H$_2$O (top) with enclosed CH$_3$CN, 8·CH$_2$Cl$_2$ (bottom left) and of 8 (bottom right). Hydrogen atoms and remaining solvent molecules of crystallization are omitted for clarity; ellipsoids are drawn at 50% probability level.

in 7·3CH$_3$CN·4H$_2$O compared to 8·3CH$_3$CN·4H$_2$O and 9·3CH$_3$CN·4H$_2$O reflect the actinide contraction.[56] As expected, the O–M–O chelate angles were found to show an opposite order than the bond lengths (6·2CH$_3$CN·4H$_2$O: O–M–O 77.0° *vs.* 7·3CH$_3$CN·4H$_2$O: O–M–O 75.6° *vs.* 8·3CH$_3$CN·4H$_2$O: O–M–O 76.8°*vs.* 9·3CH$_3$CN·4H$_2$O: O–M–O 77.5°). Related bidentate 4-acyl pyrazol-5-olate ligands coordinate Th(IV) typically in a nine- or ten-coordinated fashion with sometimes significantly longer M(IV)–O bond lengths (2.38(3) Å to 2.49(6) Å) due to less space around the metal centre.[50,57] We note that the observed C–O bond lengths are approximately 1.28 Å (Table S8, ESI†), which indicates that the ligands are present in their enolate form, as C–O bonds in uncoordinated pyrazolones typically range around 1.30 Å.[58,59] A significant difference between our phosphoryl pyrazolone HL and classical acyl pyrazolone or conventional β-diketones, such as acetylacetone (Hacac) and 2-thenoyl-trifluoroacetone (HTTA), is the higher flexibility of the O···O distance between the two donating oxygen atoms (bite size) which affects the complexation and extraction behaviour. It is known that the selectivity of 4-acyl-5-pyrazolones in the extraction of lanthanides strongly depends on the O···O distance which is the most significant factor for the selectivity in the complexation process.[60] The smallest O···O distance with 2.916(3) Å is observed in 8·3CH$_3$CN·4H$_2$O *vs.* 2.9269(18) Å (O1···O2) in 9·3CH$_3$CN·4H$_2$O, 2.934(2) Å (O1···O2) in 7·3CH$_3$CN·4H$_2$O and 2.9589(19) Å (O1···O2) in 6·2CH$_3$CN·4H$_2$O, which is longer than O···O distances of Ce(IV) β-diketonate complexes (e.g. 2.810 Å, 2.764-2.814 Å).[25,61] In all four complexes the observed four six-membered chelate rings are almost perfectly planar. Furthermore, in all complexes one CH$_3$CN molecule is located in the cavity formed by the *p*-tolyl-substituents of the four ligands (Fig. 4, molecular structure of 8·3CH$_3$CN·4H$_2$O as example). However, weak interactions such as hydrogen bonds between the solvent and ligands are not observed.
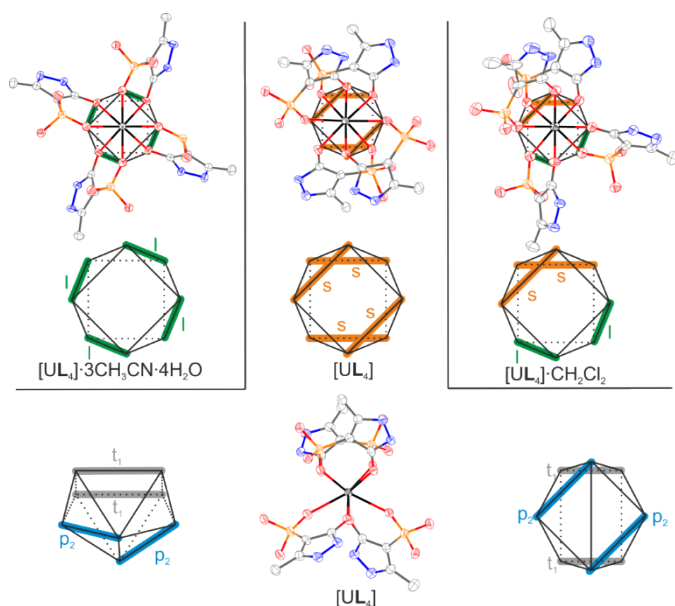
Fig. 5 View along the pseudo-tetragonal axis of the square antiprism in the structural fragment taken from XRD structure of $8 \cdot 3CH_3CN \cdot 4H_2O$ (left), 8 (middle) and $8 \cdot CH_2Cl_2$ (right) showing the coordination geometry of the $[UO_8]$ core. View on the trigonal planes of the bicapped trigonal prism in 8 (bottom). Ellipsoids are drawn at 50% probability level.

Attempts to crystallise the U(IV) complex in the absence of CH_3CN gave suitable crystals for X-ray structure analysis of $8 \cdot CH_2Cl_2$ if CH_2Cl_2 is used, and of 8 if toluene is used. For the latter, two $[UL_4]$ molecules are present in the asymmetric unit, whereas only one (A) is considered for the detailed analysis. In both, $8 \cdot CH_2Cl_2$ and 8, the coordination number remains eight formed by the coordination of four six-membered chelate rings between the O_2 donor set of four deprotonated ligands. Whereas $8 \cdot 3CH_3CN \cdot 4H_2O$ exhibits a strictly square-antiprismatic coordination environment due to the tetragonal space group $P4/n$, the structures $8 \cdot CH_2Cl_2$ and 8 are distorted towards a bicapped trigonal geometry (Fig. 5). The coordination polyhedron is best determined by measuring the angles δ and φ according to Porai-Koshits and Aslanov, (see ESI† for details) indicating a square-antiprismatic arrangement of the complex in $8 \cdot CH_2Cl_2$ but a bicapped trigonal geometry in 8.[62] Furthermore, a different arrangement of the ligands is observable for all three isomers. $8 \cdot 3CH_3CN \cdot 4H_2O$ adopts the *llll*-configuration with all ligands linking the two square faces of the polyhedron and thereby pointing all in the same direction. In contrast, the ligands in solvent-free 8 occupy two edges each of the quadrangle closest to square shape, which is described as *ssss*-configuration. In the bicapped trigonal geometry this configuration is described as $t_1t_1p_2p_2$. In the solvate $8 \cdot CH_2Cl_2$ the least symmetrical configuration *ssll* is found. It should be noted, that the asymmetric bidentate ligand L causes all three complexes to be chiral, but all structures crystallise as racemates. Isomerization between different configurations of eight-coordinate complexes has been described.[63] Potential pathways for interconversion between the three isomers are shown in Fig. S22 the ESI†.

In both molecular structures, $8 \cdot CH_2Cl_2$ and 8, the placement of the four ligands offers no solvent accessible voids within the complex core. The U(IV)–O bond lengths involving the pyrazol-5-olate unit in $8 \cdot CH_2Cl_2$ range from 2.289(2) to 2.312(2) Å and then to the
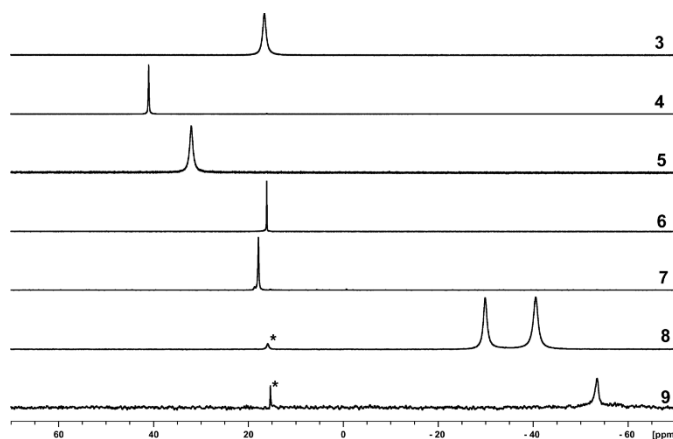

Fig. 6 ^{31}P NMR spectra of solutions of 3 (δ = 16.6 ppm), 4 (δ = 41.0 ppm), 5 (δ = 32.1 ppm), 6 (δ = 16.1 ppm), 7 (δ = 17.9 ppm), 8 (δ = -29,9 and -40.5 ppm) and 9 (δ = -53.4 ppm) at 300 K, *free ligand.

phosphoryl oxygen atom range from 2.387(2) to 2.423(3) Å (Table S9, ESI†). In 8, the U(IV)–O bond lengths show a somewhat expanded deviation and range between 2.278(4) Å and 2.357(4) Å for the pyrazol-5-olate unit and between 2.385(4) Å and 2.443(4) Å for the phosphoryl oxygen (Table S10, ESI†). The deviation to the U–O bond length of $8 \cdot 3CH_3CN \cdot 4H_2O$ (U1–O_C 2.304(2) Å; U1–O_P 2.388(2) Å) for $8 \cdot CH_2Cl_2$ is 0.035 Å and for 8 0.055 Å. In contrast, the O···O distance between the two donor atoms of the four deprotonated ligands are shorter in 8: O1A···O2A: 2.784(6) Å, O5A···O6A: 2.786(6) Å, O9A···O10A: 2.739(7) Å and O13A···O14A: 2.827(7) Å) compared to $8 \cdot CH_2Cl_2$: O1···O2: 2.811(4) Å, O5···O6: 2.803(4) Å, O9···O10: 2.876(4) Å and O13···O14: 2.863(4) Å, and $8 \cdot 3CH_3CN \cdot 4H_2O$: O1···O2: 2.916(3) Å. The six shortest distances are found where the respective ligands occupy an *s*-edge of the square antiprism, whereas all longer ones are found on *l*-edges. A study of the relationship between bite angle and preferred geomery indicates a preference for the *llll*-configuration for ligands with larger and *ssss* with smaller bite angles.[64] The flexibility of the phosphoryl pyrazoloate allows for different coordination geometries to be adopted. Further, in both structures only one of the four six-membered chelate rings is almost perfectly planar to the metal centre with a dihedral angel of 2.2° in $8 \cdot CH_2Cl_2$ and 2.3° in 8, respectively. The remaining dihedral angles between the planes are 11.8°, 12.5° and 15.4° in $8 \cdot CH_2Cl_2$ (Table S9, ESI†) and 9.2°, 6.5° and 12.2° in 8 (Table S10, ESI†).

The crystal structures cannot provide any information about the structures of the complexes in solution. NMR experiments were therefore carried out on solutions of the complexes. A single resonance is observed in the ^{31}P NMR spectra at δ = 16.6 ppm, 41.0 ppm, 32.1 ppm, and 16.1 ppm for the La(III) complex 3, the Ce(III) complexes 4 and 5, and the Ce(IV) complex 6, respectively (Fig. 6). This shows the presence of a single complex species in solution, most likely in a coordination geometry comparable to those observed in the crystal structures. In addition, ^{31}P NMR spectroscopy can be used to determine the coordination number and oxidation state of the metal centre. For the Ce(III) complexes, the resonance at δ = 41.0 ppm is attributed to the $[CeL_3]$ complex 4, whereas the resonance at δ = 32.1 ppm is observed for 5 ($[CeL_3HL]$). A control experiment reacting 4 with one equivalent of HL gives a ^{31}P NMR spectrum with a single resonance at 32.1 ppm, matching exactly the obtained resonance of 5 (Fig. 7). In addition, the resonance at
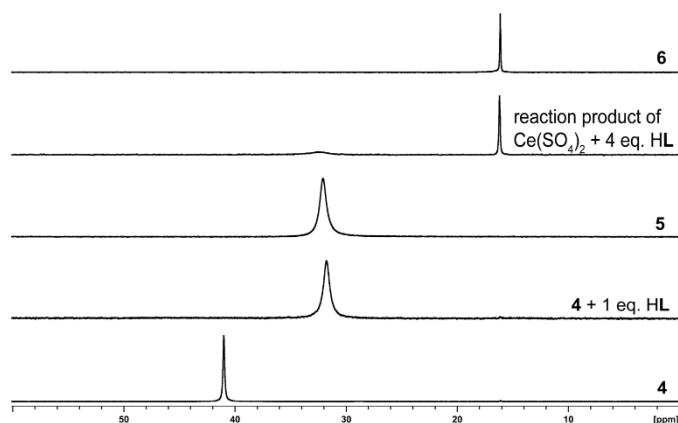
Fig. 7 ^{31}P NMR spectra of the Ce(III) complex **4** (δ = 41.0 ppm), the reaction product of **4** with 1 eq. H**L** (δ = 32.1 ppm), **5** (δ = 32.1 ppm), the Ce(IV) complex **6** (δ = 16.1 ppm), and the reaction product of Ce(SO$_4$)$_2$ with 4 eq. H**L** (δ = 16.1 and 32.3 ppm) at 300 K in CD$_2$Cl$_2$.

Fig 8 ^{31}P-^{31}P- EXSY NMR spectrum of a solution of [U**L**$_4$] complex **8** at 300 K in CD$_2$Cl$_2$ with a mixing time of 0.025 seconds.

Fig. 9 ^{31}P NMR spectra of a solution of [U**L**$_4$] complex **8** at 300 K in CD$_2$Cl$_2$ (bottom) and in CD$_2$Cl$_2$/CH$_3$CN (top).

32.1 ppm was also obtained in the crude reaction product of H**L** and Ce(SO$_4$)$_2$·4H$_2$O. After washing the reaction solution with the oxidant KMnO$_4$ (5 mM aqueous solution) this resonance vanished and only the resonance of the Ce(IV) complex **6** at δ = 16.1 ppm remained, showing that the change in the oxidation state of the centre results in a shift of 16 ppm towards lower field (Fig. 7).

For the Th(IV) complex **7** and the Np(IV) complex **9** a single resonance at δ = 17.9 ppm and a broad resonance at δ = −53.4 ppm are observed (Fig. 6), indicating the presence of a respective single complex species which may have a comparable coordination of the metal atom in solution. In contrast, two resonances at δ = −29.9 ppm and −40.5 ppm are obtained for the U(IV) complex **8** in CD$_2$Cl$_2$, pointing at the presence of more than one species in solution. Presumably, the two different coordination polyhedra observed for the U(IV) complex in the crystal structures of **8**·3CH$_3$CN·4H$_2$O, of **8**·CH$_2$Cl$_2$ (square antiprismatic), and **8** (bi-capped trigonal prismatic), respectively (Fig. 5), are also present in solution. Extended ^{31}P NMR studies involving a ^{31}P-^{31}P exchange spectroscopy (EXSY) experiment at room temperature (Fig. 8) and at 190 K (Fig. S24, ESI†) reveal an exchange between the two respective species. As no exchange peaks are observed for the remaining free ligand (δ = 15.3 ppm) the exchange may occur between the present species of the [U**L**$_4$] complex only. Furthermore, a solvent influence is noticeable. In CD$_2$Cl$_2$ the two resonances integrate approximately equal (integration ratio normalized to an overall integral of 1.0: 0.45 to 0.55 for δ at −29.9 and −40.5 ppm), pointing at the presence of both species in comparable concentration. Upon the addition of CH$_3$CN this ratio changes to 0.25 to 0.75 (Fig. 9). Such a solvent influence is also observed in toluene-d_8 and hexafluorobenzene upon the addition of CH$_3$CN (Fig. S28 and Fig. S29, ESI†). Thus, increasing the concentration of CH$_3$CN shifts the equilibrium between the two coordination polyhedra, presumably towards the structure observed in the presence of CH$_3$CN in which the U(IV) metal centre has the highly symmetric square antiprismatic coordination sphere. The latter is obtained as the only coordination geometry for the other studied M(IV) f-block metals and may be the preferred arrangement with H**L** under the chosen experimental conditions.

In order to get further information about the complex structure in solution extended X-ray absorption fine structure (EXAFS)
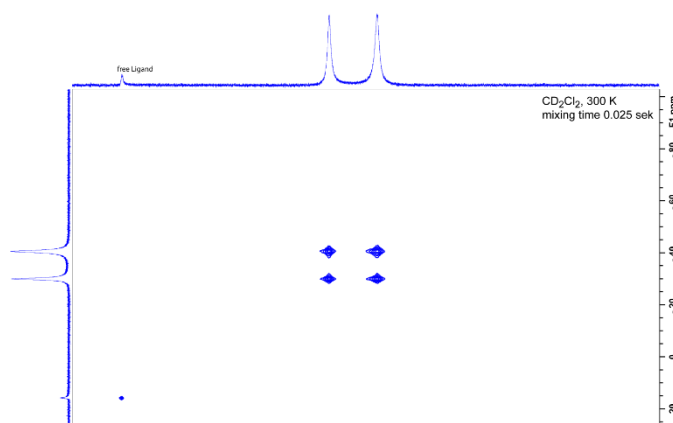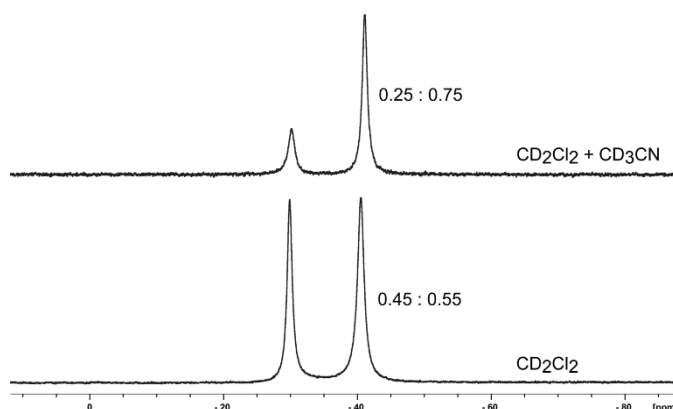
spectroscopy has been applied to elucidate the coordination environment of the U(IV) and Np(IV) complexes. The experiments will give the type, number and distance of neighbouring atoms to the central atom, which can be correlated to a structural model based on the structural information obtained from the X-ray single crystal analysis. For the Np(IV) complex the structural data of **9**·3CH$_3$CN·4H$_2$O were used. In the case of U(IV) we assumed according to the NMR experiments a mixture of complexes in approximately equal concentration in toluene solution with **8**·3CH$_3$CN·4H$_2$O, **8**·CH$_2$Cl$_2$, and **8** as representative structures for the different coordination polyhedra of the U(IV) metal centre. The EXAFS investigations were carried out at the Rossendorf Beamline (ROBL) of the ESRF in Grenoble.[65] Details on the theoretical background as well as the fitting procedures are given in the supporting information (ESI†). In order to obtain a reliable evaluation on the EXAFS spectra, three methods were applied comparatively, including shell fit, Monte-Carlo (MC) Simulation, and a Fourier filtering algorithm (FFA) which was used for the first time by Taube et al..[66]

Upon shell fit, the radial distances (r), agreeing within 0.02 Å with the structural data from the XRD, could be obtained for both complexes (Table 1). The larger deviations of 0.035 Å - 0.031 Å observed for the U/Np–P interaction exceeds slightly the common uncertainty in determination of r (0.02 Å) by EXAFS[67] and may indicate small structural deviations between the solid-state structures of the complexes and their solutions. Although small deviations can be already a hint to an intrinsic problem of the fit, however, the good description of the strong structural features in the
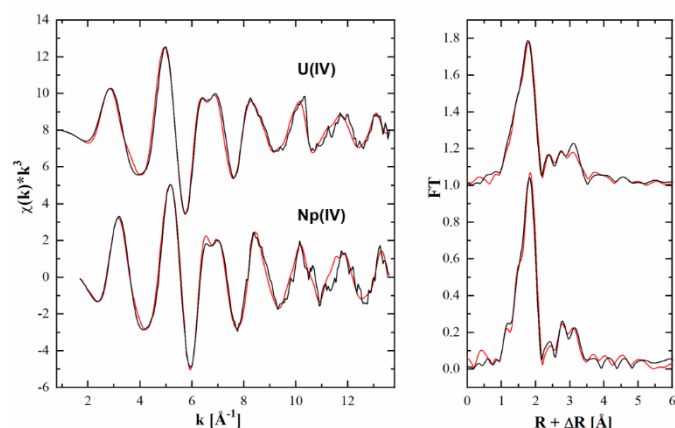
ARTICLE

Fig. 10 Experimental (black) k^3-weighted EXAFS spectra of the U(IV) complexes and the Np(IV) complex acquired as toluene solution and the modified theoretical spectra (red (left)). Corresponding Fourier transform (right).

spectra of both systems (Fig. 10) support the reliability of the fit. The MC simulation of the mixed U(IV) complexes and of the Np(IV) complex in solution was performed by constructing models from the XRD structural data. This resulted in a 3D particle distribution and a fit of the EXAFS spectra, which outperforms the quality of the shell fit (see ESI†). Up to 6 Å the structures of the U(IV) complexes and the structure of the Np(IV) complex, equals the corresponding solid-state structure/s, obtained by single crystal X-ray analysis. The result is illustrated in Fig. 11, which shows the good agreement between the MC simulated structures of the U(IV) complex in solution (yellow) with the crystal structures of **8**·3CH₃CN·4H₂O, **8**·CH₂Cl₂, and **8**. As

Table 1 EXAFS shell fit parameter of the U(IV) and Np(IV) complexes in toluene solution.

Path/sample	n	r/Å	Δr/Å	σ²/Å²	ΔE₀/Ev
8·3CH₃CN·4H₂O, 8·CH₂Cl₂, 8					
U–O1	4	2.30(1)	0.00ᵃ	0.0059(9)	1.9(3)
U–O2	4	2.39(1)	0.00ᵃ	0.008(2)	1.9/
U–C1	4	3.361(8)	0.022ᵃ	0.0034(5)	1.9/
U–O1–C1	8	3.480/		0.0034/	1.9/
U–O1–C1–O1	4	3.598/		0.0034/	1.9/
U–P	4	3.647(5)	0.035ᵃ	0.0064(8)	1.9/
U–O2–P	8	3.72(1)		0.0064/	1.9/
U–O2–P–O2	4	3.83/		0.0064/	1.9/
U–C2	4	3.97(1)	0.00ᵃ	0.005	1.9/
9·3CH₃CN·4H₂O					
Np–O1	4	2.278(7)	0.020	0.0052(9)	9.87(4)
Np–O2	4	2.369(9)	0.008	0.006(1)	9.87/
Np–C1	4	3.337(5)	0.007	0.0017(4)	9.87/
Np–O1–C1	8	3.455/		0.0017/	9.87/
Np–O1–C1–O1	4	3.572/		0.0017/	9.87/
Np–P	4	3.605(6)	0.031	0.0060(9)	9.87/
Np–O2–P	8	3.69(2)		0.0060/	9.87/
Np–O2–P–O2	4	3.809/		0.0060/	9.87/
Np–C2	4	3.94(1)	-0.03	0.005	9.87/

/-linked parameter. n – coordination number, r – radial distance, σ² – Debye-Waller factor, ΔE₀ - shift in energy threshold, Δr - difference between distances supplied by the XRD structure and corresponding shell fit distances. ᵃ – calculated with average distances taken from XRD structural data of **8**·3CH₃CN·4H₂O, **8**·CH₂Cl₂, and **8**, respectively. Estimated standard deviations of the variable parameter as given from EXAFSPAK in parenthesis.
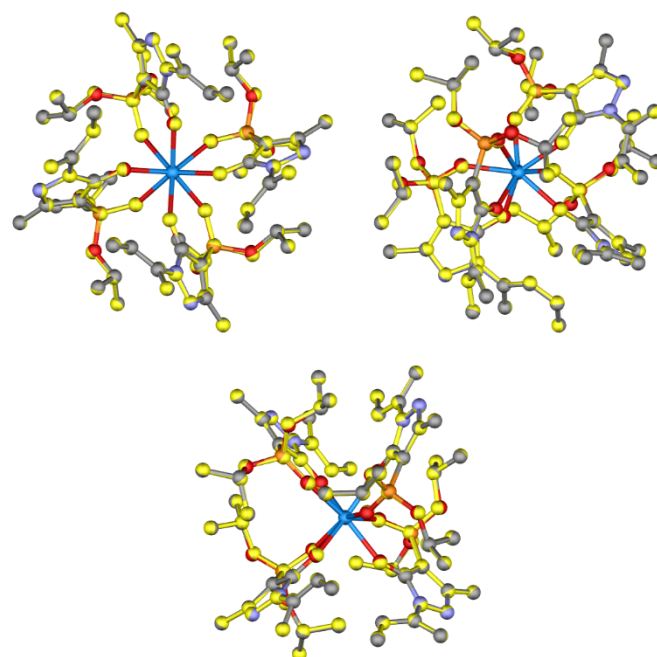

Fig. 11 Structure of **8**·3CH₃CN·4H₂O (upper left), **8**·CH₂Cl₂ (upper right), and **8** (lower middle) provided by XRD structural data (coloured) and the determined average atomic positions by using MC simulation (yellow). CH₃CN entity in **8**·3CH₃CN·4H₂O omitted for better visualization.

third evaluation of the obtained EXAFS spectra the FFA was conducted, which comprises the calculation of a theoretical EXAFS spectrum based on the crystal structures. It has to be stated that usually, a correlation of solid state and liquid phase structure can be obtained by a plain comparison of the solid-state and the solution EXAFS. Since herein only the experimental EXAFS data for the complexes in solution were available, the task was to compare the crystal structures with EXAFS without knowing the experimental amplitude functions like Debye-Waller damping terms (σ²). By implementation of a constant ΔE₀, which was provided by the shell fit of the EXAFS spectra in solution (Table 1), the theoretical phase and amplitude functions could be adjusted to a certain Fermi level (for details see ESI†). As a result, a direct comparison of the theoretical EXAFS spectra, based on the solid state molecular structures and the experimental EXAFS spectra of the solution samples, was possible. It could be confirmed that the theoretical EXAFS spectra, based on the structures of **8**·3CH₃CN·4H₂O, **8**·CH₂Cl₂, **8**, and **9**·3CH₃CN·4H₂O compares well to the experimental EXAFS spectra of the U(IV) and Np(IV) complexes in toluene solution (Fig. 10).

Conclusions

Despite the wealth of previous reports on structural analyses of actinide(IV) complexes there are few studies focusing on the structural features of their coordination in solution. This study has demonstrated that the 4-phosphoryl pyrazolone H**L** is suitable to coordinate such metal ions in solid state and in solution. Single crystal X-ray analyses show isostructural complexes for the *f*-elements Ce(IV), Th(IV), and Np(IV) with a coordination number of eight provided by the two O-donor atoms of four deprotonated ligands. Detailed analysis of EXAFS studies of the U(IV) and Np(IV) complexes in solution point at the same structural features. Thus, the coordination of the metal ions by the deprotonated 4-phosphoryl pyrazol-5-olate ligand H**L** are essentially the same in toluene solution

and in the solid state indicating that intermolecular interactions do not play a significant role for the compounds' crystallization. These results provide insight into the bonding and coordination of the *f*-elements in solution.
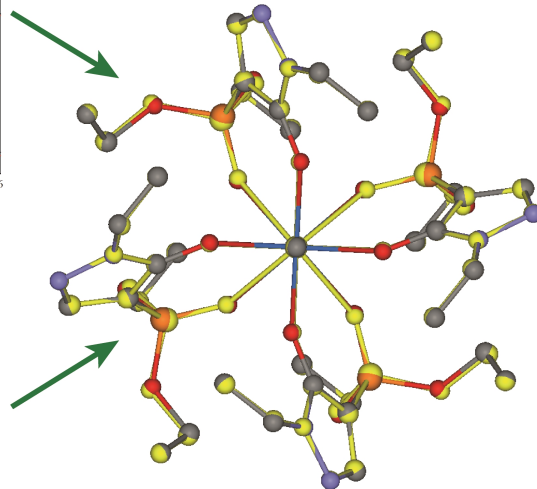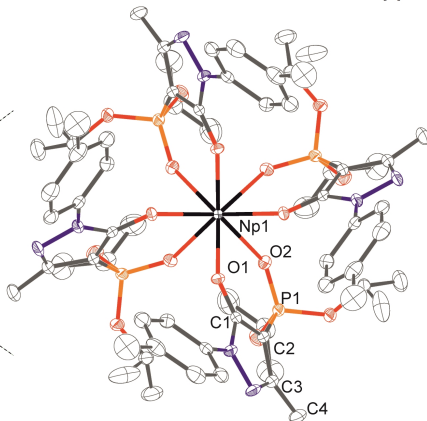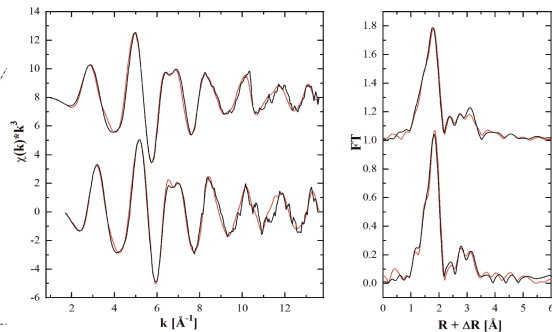
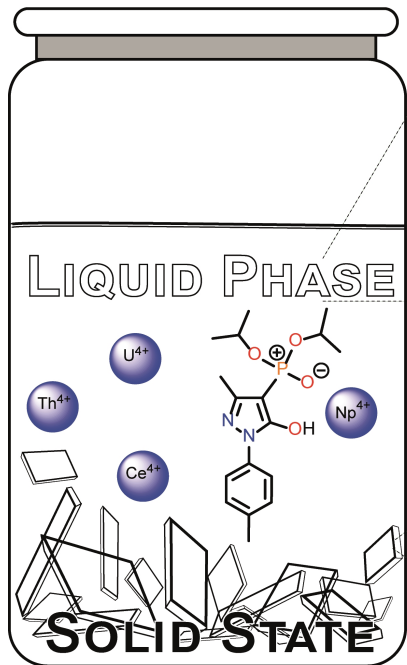## Conflicts of interest

There are no conflicts to declare.

Notes and references

1. J. Veliscek-Carolan, *J. Hazard. Mater.*, 2016, **318**, 266-281.
2. J. I. Kim, *Nucl. Eng. Technol.*, 2006, **38**, 459-482.
3. M. B. Jones and A. J. Gaunt, *Chem. Rev.*, 2013, **113**, 1137-1198.
4. P. J. Panak and A. Geist, *Chem. Rev.*, 2013, **113**, 1199-1236.
5. G. T. Kent, G. Wu and T. W. Hayton, *Inorg. Chem.*, 2019, **58**, 8253-8256.
6. N. P. Martin, J. März, C. Volkringer, N. Henry, C. Hennig, A. Ikeda-Ohno and T. Loiseau, *Inorg. Chem.*, 2017, **56**, 2902-2913.
7. B. E. Klamm, C. J. Windorff, M. L. Marsh, D. S. Meeker and T. E. Albrecht-Schmitt, *Chem. Commun.*, 2018, **54**, 8634-8636.
8. Z. Zhang, B. F. Parker, T. D. Lohrey, S. J. Teat, J. Arnold and L. Rao, *Dalton Trans.*, 2018, **47**, 8134-8141.
9. N. S. Settineri and J. Arnold, *Chem. Sci.*, 2018, **9**, 2831-2841.
10. A. McSkimming, J. Su, T. Cheisson, M. R. Gau, P. J. Carroll, E. R. Batista, P. Yang and E. J. Schelter, *Inorg. Chem.*, 2018, **57**, 4387-4394.
11. B. E. Klamm, C. J. Windorff, C. Celis-Barros, M. L. Marsh, D. S. Meeker and T. E. Albrecht-Schmitt, *Inorg. Chem.*, 2018, **57**, 15389-15398.
12. C. A. P. Goodwin, F. Tuna, E. J. L. McInnes and D. P. Mills, *Eur. J. Inorg. Chem.*, 2018, **2018**, 2356-2362.
13. A. C. Behrle, A. J. Myers, A. Kerridge and J. R. Walensky, *Inorg. Chem.*, 2018, **57**, 10518-10524.
14. S. P. Kelley, V. Smetana, S. D. Emerson, A.-V. Mudring and R. D. Rogers, *Chem. Commun.*, 2020, **56**, 4232-4235.
15. G. Feng, K. N. McCabe, S. Wang, L. Maron and C. Zhu, *Chem. Sci.*, 2020, **11**, 7585-7592.
16. N. Jori, M. Falcone, R. Scopelliti and M. Mazzanti, *Organometallics*, 2020, **39**, 1590-1601.
17. W. Zhou, D. McKearney and D. B. Leznoff, *Chem. Eur. J.*, 2020, **26**, 1027-1031.
18. C. J. Tatebe, E. M. Matson, C. L. Clark, J. J. Kiernicki, P. E. Fanwick, M. Zeller and S. C. Bart, *Organometallics*, 2020, **39**, 353-360.
19. J. T. Boronski, L. R. Doyle, J. A. Seed, A. J. Wooles and S. T. Liddle, *Angew. Chem. Int. Ed.*, 2020, **59**, 295-299.
20. Y. Zhang, K. Lu, M. Liu, I. Karatchevtseva, Z. Tao and G. Wei, *Dalton Trans.*, 2020, **49**, 404-410.
21. J. T. Brewster, D. N. Mangel, A. J. Gaunt, D. P. Saunders, H. Zafar, V. M. Lynch, M. A. Boreen, M. E. Garner, C. A. P. Goodwin, N. S. Settineri, J. Arnold and J. L. Sessler, *J. Am. Chem. Soc.*, 2019, **141**, 17867-17874.
22. K. S. Pedersen, K. R. Meihaus, A. Rogalev, F. Wilhelm, D. Aravena, M. Amoza, E. Ruiz, J. R. Long, J. Bendix and R. Clérac, *Angew. Chem. Int. Ed.*, 2019, **58**, 15650-15654.
23. J. N. Wacker, S. Y. Han, A. V. Murray, N. A. Vanagas, J. A. Bertke, J. M. Sperling, R. G. Surbella and K. E. Knope, *Inorg. Chem.*, 2019, **58**, 10578-10591.
24. K. Takao, J. März, M. Matsuoka, T. Mashita, H. Kazama and S. Tsushima, *RSC Advances*, 2020, **10**, 6082-6087.
25. S. K. Cary, M. Livshits, J. N. Cross, M. G. Ferrier, V. Mocko, B. W. Stein, S. A. Kozimor, B. L. Scott and J. J. Rack, *Inorg. Chem.*, 2018, **57**, 3782-3797.
26. L. Götzke, G. Schaper, J. März, P. Kaden, N. Huittinen, T. Stumpf, K. K. K. Kammerlander, E. Brunner, P. Hahn, A. Mehnert, B. Kersting, T. Henle, L. F. Lindoy, G. Zanoni and J. J. Weigand, *Coord. Chem. Rev.*, 2019, **386**, 267-309.
27. A. E. V. Gorden, M. A. DeVore and B. A. Maynard, *Inorg. Chem.*, 2013, **52**, 3445-3458.
28. A. Leoncini, J. Huskens and W. Verboom, *Chem. Soc. Rev.*, 2017, **46**, 7229-7273.
29. D. Das, G. Gopakumar, C. V. S. Brahmmananda Rao, N. Sivaraman, A. Sivaramakrishna and K. Vijayakrishna, *J. Coord. Chem.*, 2017, **70**, 3338-3352.
30. D. Das, C. V. S. Brahmmananda Rao, N. Sivaraman, A. Sivaramakrishna and K. Vijayakrishna, *Inorg. Chim. Acta*, 2018, **482**, 597-604.
31. A. N. Turanov, V. K. Karandashev, O. I. Artyushin and V. K. Brel, *Solvent Extr. Ion Exch.*, 2020, **38**, 166-179.
32. S. T. Disale, C. V. S. Brahmmananda Rao, G. Gopakumar and R. V. Jayaram, *J. Coord. Chem.*, 2019, **72**, 1480-1496.
33. M. Huang, Y. Fu, Y. Lu, W. Liao and Z. Li, *J. Rare Earths*, 2019.
34. D. Das, A. Sivaramakrishna, G. Gopakumar, C. V. S. Brahmmananda Rao, N. Sivaraman and K. Vijayakrishna, *Polyhedron*, 2018, **141**, 215-222.
35. G. Jegan, A. Suresh, C. V. S. Brahmmananda Rao, B. Sreenivasulu and N. Sivaraman, *Inorg. Chim. Acta*, 2019, **495**, 118935.
36. C. Huang, H. Lv, C. Zuo, Z. Yuan, W. Zheng and T. Yan, *J. Radioanal. Nucl. Chem.*, 2018, **317**, 103-110.
37. M. Alyapyshev, V. Babain, L. Tkachenko, E. Kenf, I. Voronaev, D. Dar'in, P. Matveev, V. Petrov, S. Kalmykov and Y. Ustynyuk, *J. Radioanal. Nucl. Chem.*, 2018, **316**, 419-428.
38. M. Bholanath, S. K. Avinash, A. A. Seraj, B. Arunasis and K. M. Prasanta, *Radiochim. Acta*, 2019, **107**, 369-376.
39. B. Mahanty, A. Bhattacharyya, A. S. Kanekar and P. K. Mohapatra, *Solvent Extr. Ion Exch.*, 2020, **38**, 290-303.
40. D. Whittaker, A. Geist, G. Modolo, R. Taylor, M. Sarsfield and A. Wilden, *Solvent Extr. Ion Exch.*, 2018, **36**, 223-256.
41. S. A. Ansari, A. Bhattacharyya, P. K. Mohapatra, R. J. M. Egberink, J. Huskens and W. Verboom, *RSC Advances*, 2019, **9**, 31928-31935.
42. A. Sengupta, P. K. Mohapatra, P. Pathak, T. K. Ghanty and W. Verboom, *New J. Chem.*, 2017, **41**, 836-844.

43. M. F. Cheira, A. S. Orabi, B. M. Atia and S. M. Hassan, *J. Solution Chem.*, 2018, **47**, 611-633.

44. Y. Wei-fan, Y. Shuanggui, X. Yanbing, X. Yonghou, F. Ke-ming and X. Bing, *J. Radioanal. Nucl. Chem.*, 2003, **256**, 149-152.

45. R. Meera, R. Luxmi Varma and M. L. P. Reddy, *Radiochim. Acta*, 2004, **92**, 17-23.

46. Z. W. Pan, J. H. Lin, W. J. Li, T. C. Wu and J. D. Pan, *Adv. Mat. Res.*, 2013, **602-604**, 887-891.

47. A. M. Wilson, P. J. Bailey, P. A. Tasker, J. R. Turkington, R. A. Grant and J. B. Love, *Chem. Soc. Rev.*, 2014, **43**, 123-134.

48. F. Marchetti, C. Pettinari and R. Pettinari, *Coord. Chem. Rev.*, 2005, **249**, 2909-2945.

49. F. Marchetti, R. Pettinari and C. Pettinari, *Coord. Chem. Rev.*, 2015, **303**, 1-31.

50. G. D. Jarvinen, A. J. Zozulin, E. M. Larson and R. R. Ryan, *Acta Crystallogr., Sect. C: Cryst. Struct. Commun.*, 1991, **47**, 262-264.

51. D. Matt, D. Lakkis, D. Grandjean, F. Balegroune and A. Laidoudi, *Acta Crystallogr., Sect. C: Cryst. Struct. Commun.*, 1992, **48**, 1408-1411.

52. R. D. Hubbard and B. L. Miller, *J. Org. Chem.*, 1998, **63**, 4143-4146.

53. B. Corbel, I. LHostisKervella and J. P. Haelters, *Synth. Commun.*, 1996, **26**, 2561-2568.

54. J. Modranka, R. Jakubowski, M. Różalski, U. Krajewska, A. Janecka, K. Gach, D. Pomorska and T. Janecki, *Eur. J. Med. Chem.*, 2015, **92**, 565-574.

55. S. M. Bowen, E. N. Duesler and R. T. Paine, *Inorg. Chem.*, 1982, **21**, 261-265.

56. R. Shannon, *Acta Crystallographica Section A*, 1976, **32**, 751-767.

57. J. Xu and K. N. Raymond, *Angew. Chem. Int. Ed.*, 2006, **45**, 6480-6485.

58. T. U. Sheikh, M. A. Khan, M. N. Arshad, I. U. Khan and H. Stoeckli-Evans, *Acta Crystallogr., Sect. E: Struct. Rep. Online*, 2009, **65**, o330.

59. A. Cingolani, Effendy, F. Marchetti, C. Pettinari, R. Pettinari, B. W. Skelton and A. H. White, *Inorg. Chem.*, 2002, **41**, 1151-1161.

60. S. Umetani, Y. Kawase, Q. T. H. Le and M. Matsui, *J. Chem. Soc., Dalton Trans.*, 2000, 2787-2791.

61. E. C. Lingafelter and R. L. Braun, *J. Am. Chem. Soc.*, 1966, **88**, 2951-2956.

62. M. A. Porai-Koshits and L. A. Aslanov, *J. Struct. Chem.*, 1972, **13**, 244-253.

63. R. C. Fay, *Coord. Chem. Rev.*, 1996, **154**, 99-124.

64. D. G. Blight and D. L. Kepert, *Inorg. Chem.*, 1972, **11**, 1556-1561.

65. A. C. Scheinost, J. Claussner, J. Exner, M. Feig, S. Findeisen, C. Hennig, K. O. Kvashnina, D. Naudet, D. Prieur, A. Rossberg, M. Schmidt, C. Qiu, P. Colomp, C. Cohen, E. Dettona, V. Dyadkin and T. Stumpf, *J. Synchrotron Radiat.*, 2021, **28**, in press.

66. F. Taube, B. Drobot, A. Rossberg, H. Foerstendorf, M. Acker, M. Patzschke, M. Trumm, S. Taut and T. Stumpf, *Inorg. Chem.*, 2019, **58**, 368-381.

67. G. G. Li, F. Bridges and C. H. Booth, *Physical Review B*, 1995, **52**, 6332-6348.

Same local structure

Fig1.png

$[CeL_3(CH_3CN)]$

Fig2.png

$[CeL_3HL]·CH_3CN·Et_2O$

$[CeL_4]\cdot 2CH_3CN\cdot 4H_2O$

$[ThL_4]\cdot 3CH_3CN\cdot 4H_2O$

$[UL_4]\cdot 3CH_3CN\cdot 4H_2O$

$[NpL_4]\cdot 3CH_3CN\cdot 4H_2O$

Fig3.png

Fig4.png

[U**L**$_4$]·3CH$_3$CN·4H$_2$O

[U**L**$_4$]

[U**L**$_4$]·CH$_2$Cl$_2$

Figure 1 [U**L**$_4$]

free Ligand

CD$_2$Cl$_2$, 300 K
mixing time 0.025 sek

F1 ppm

F2 ppm

Chemical Science
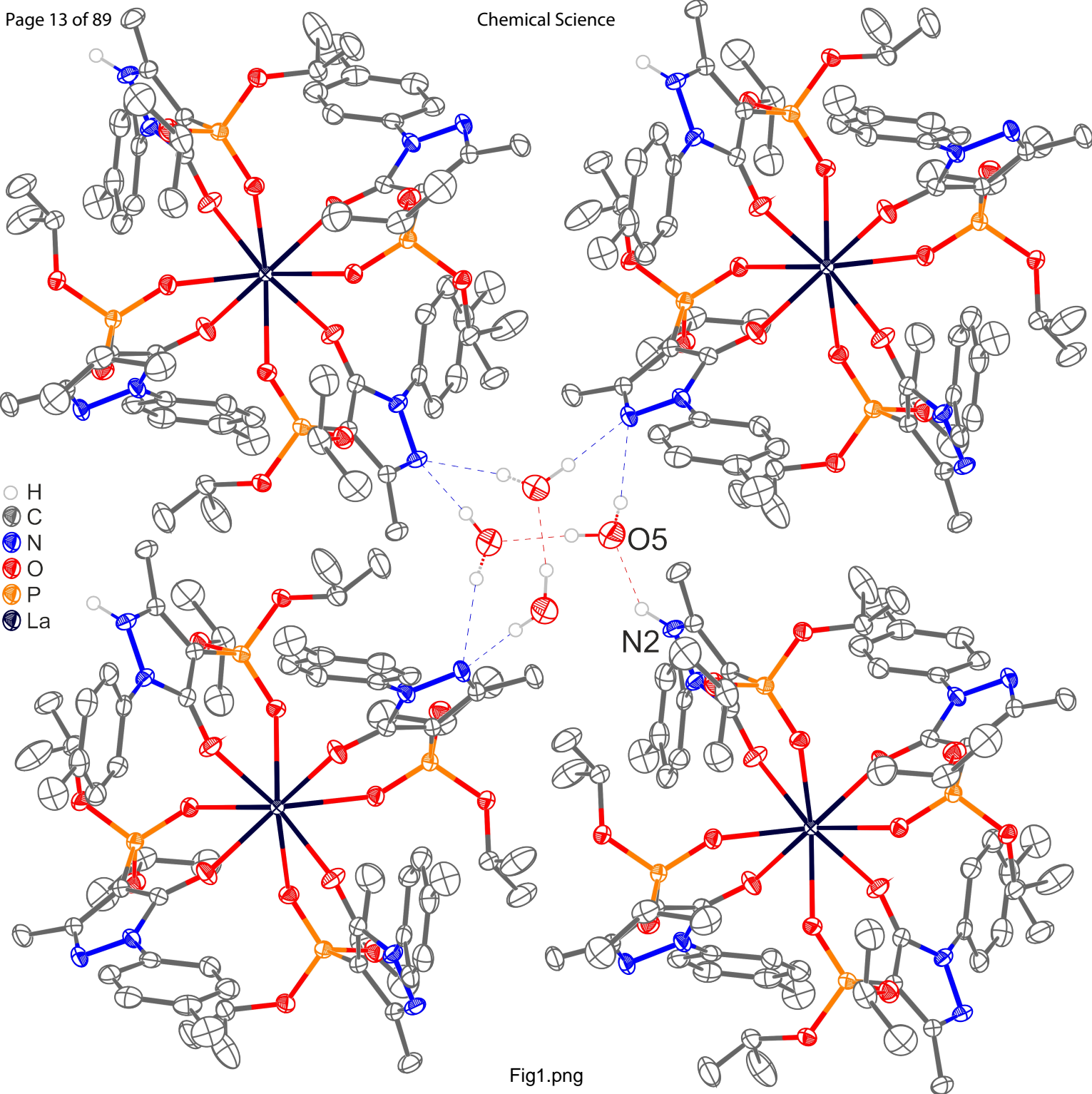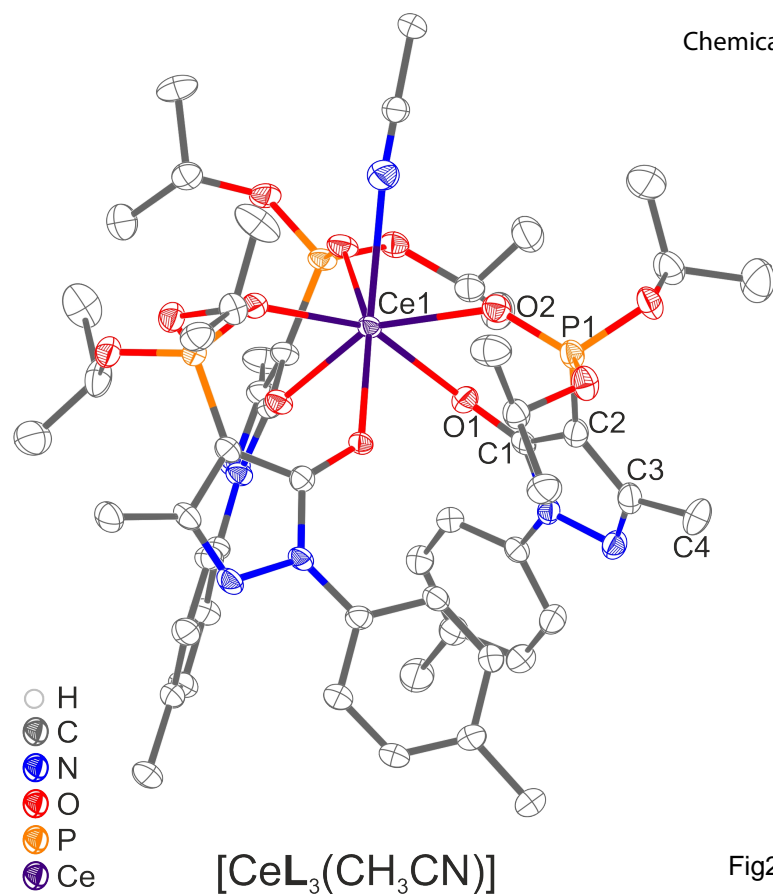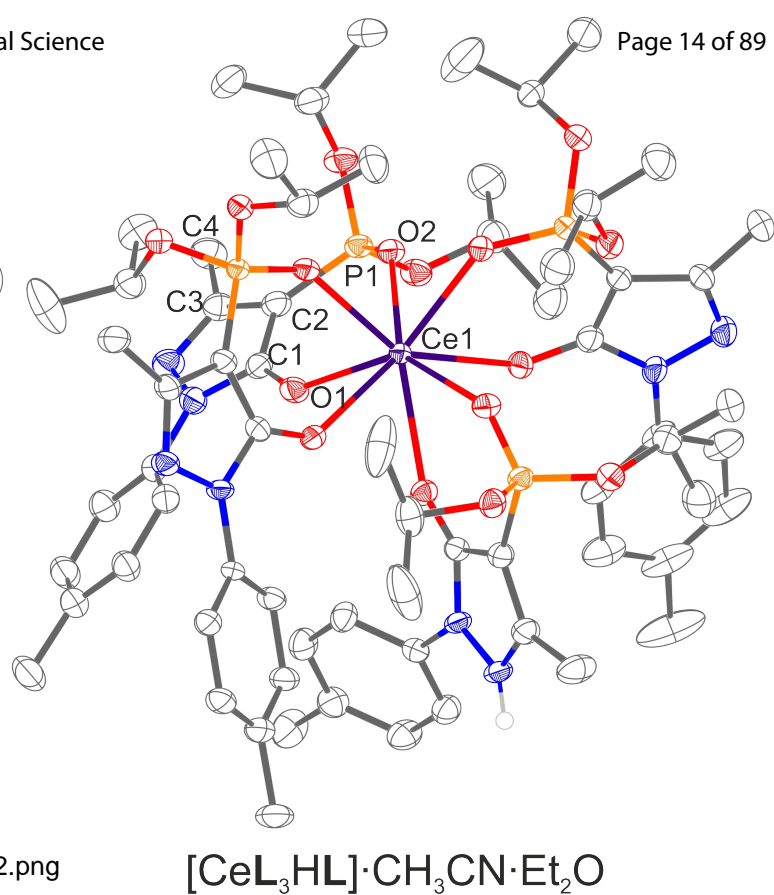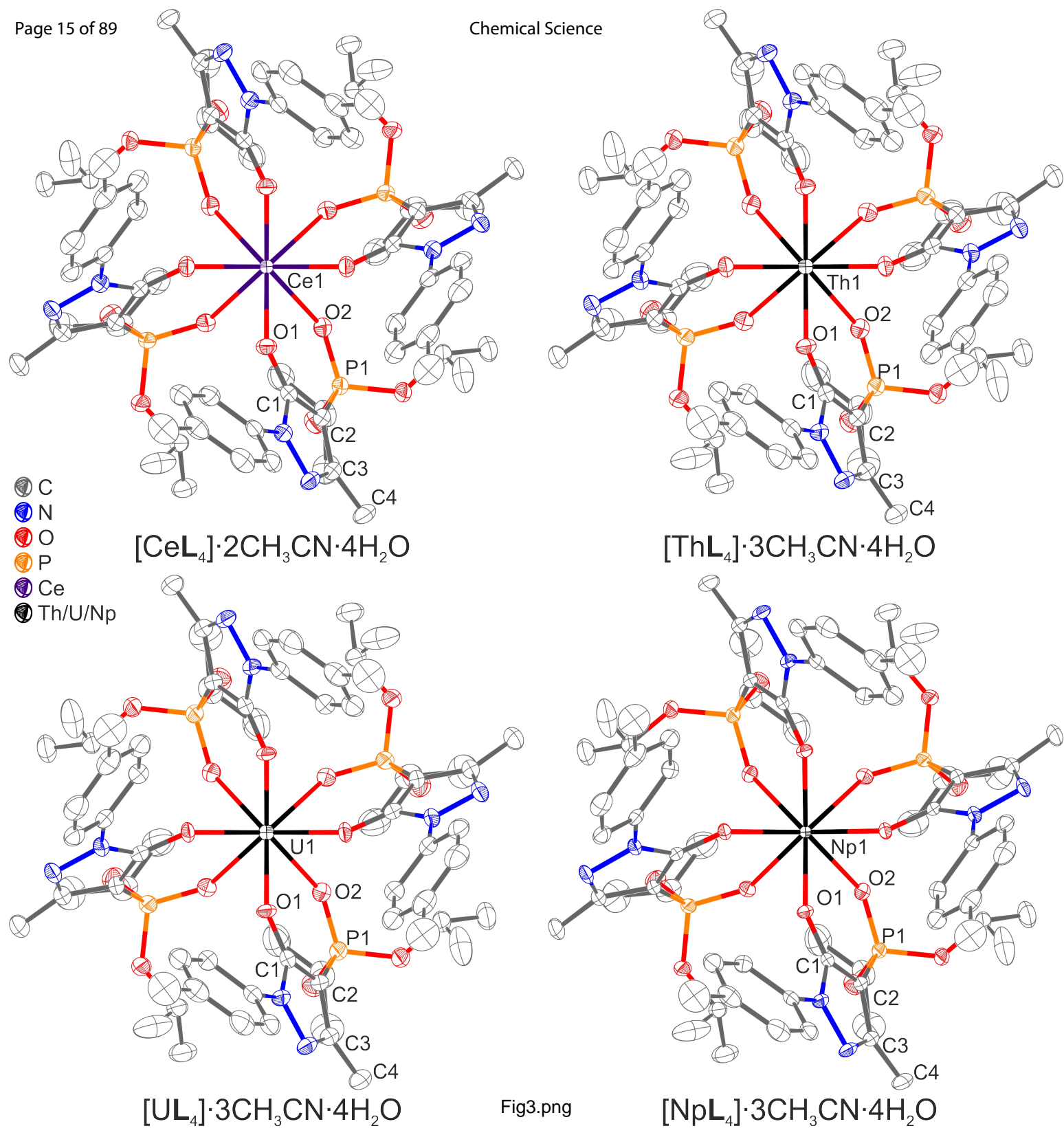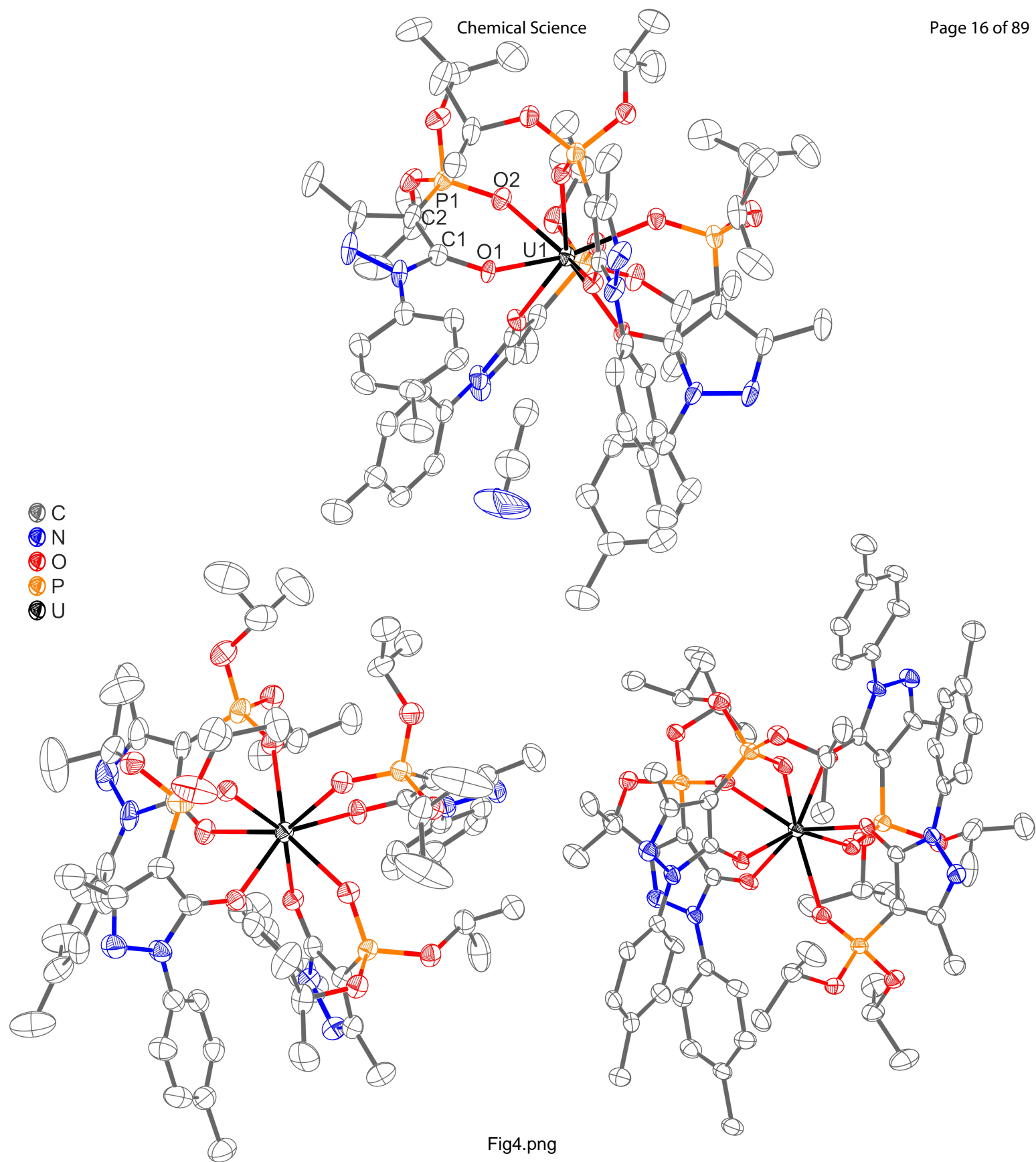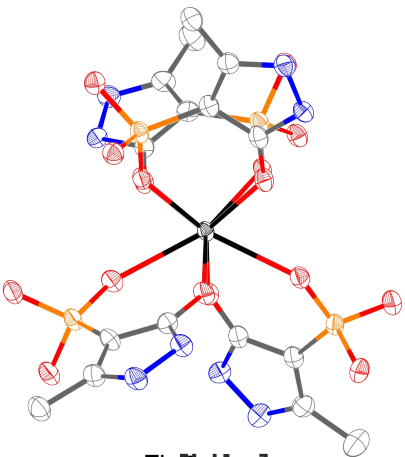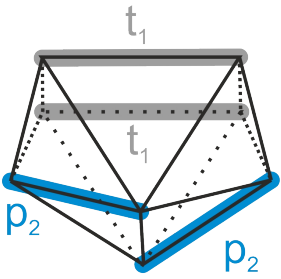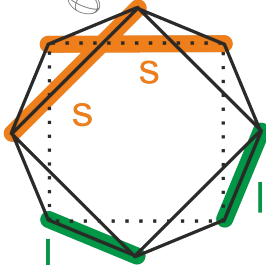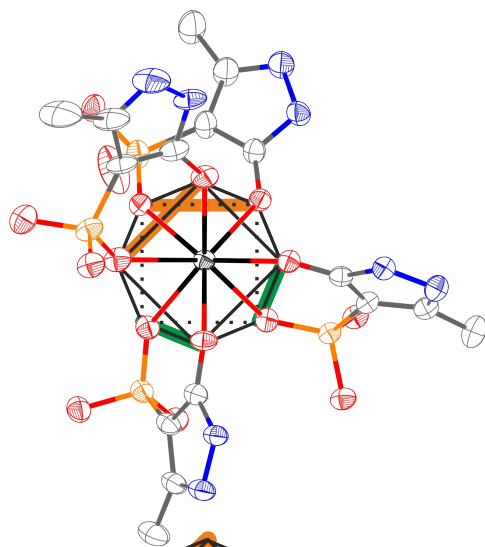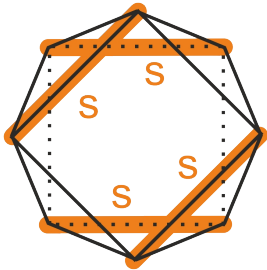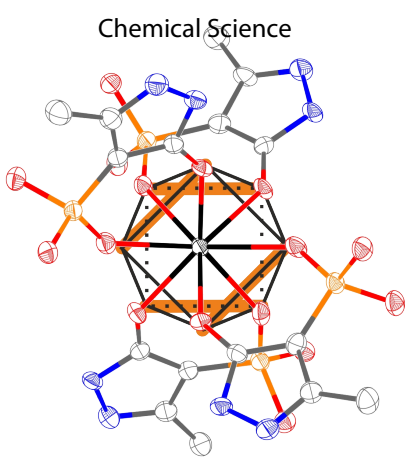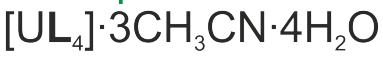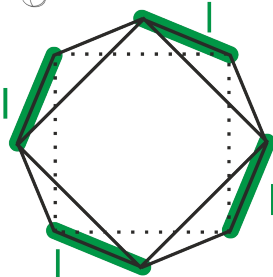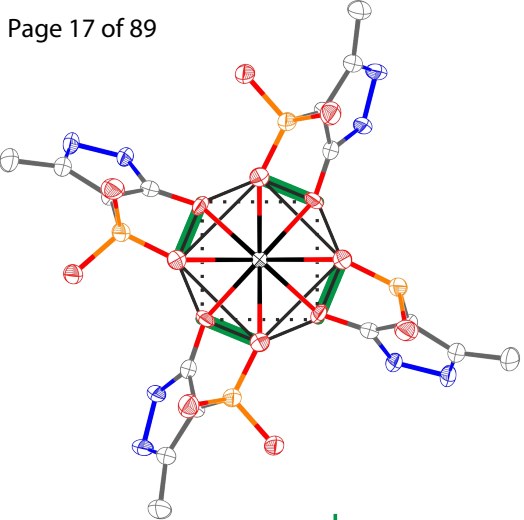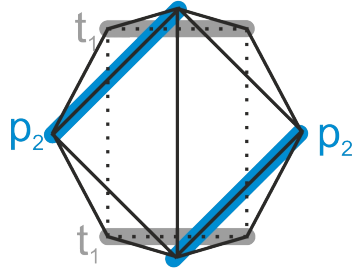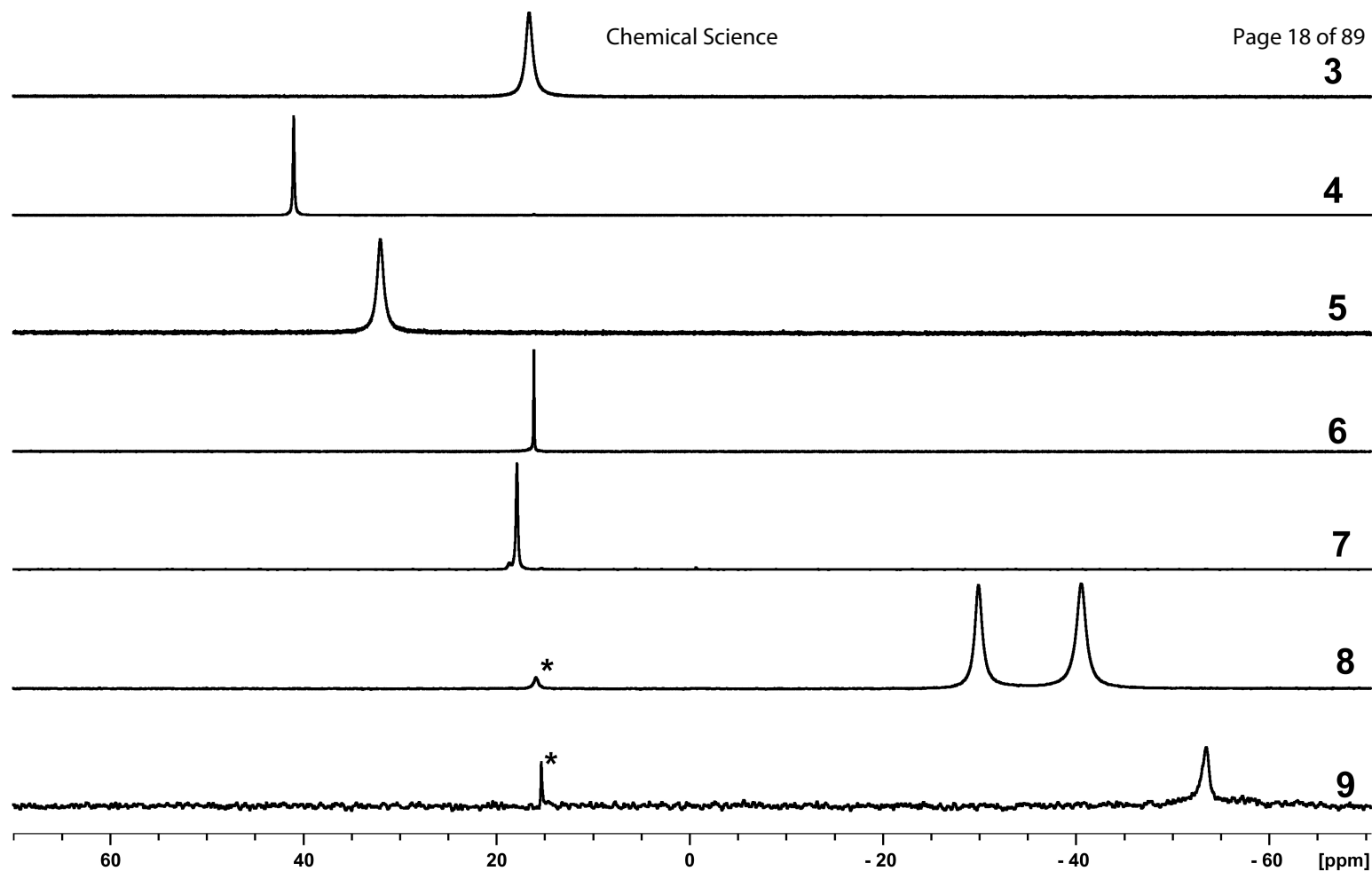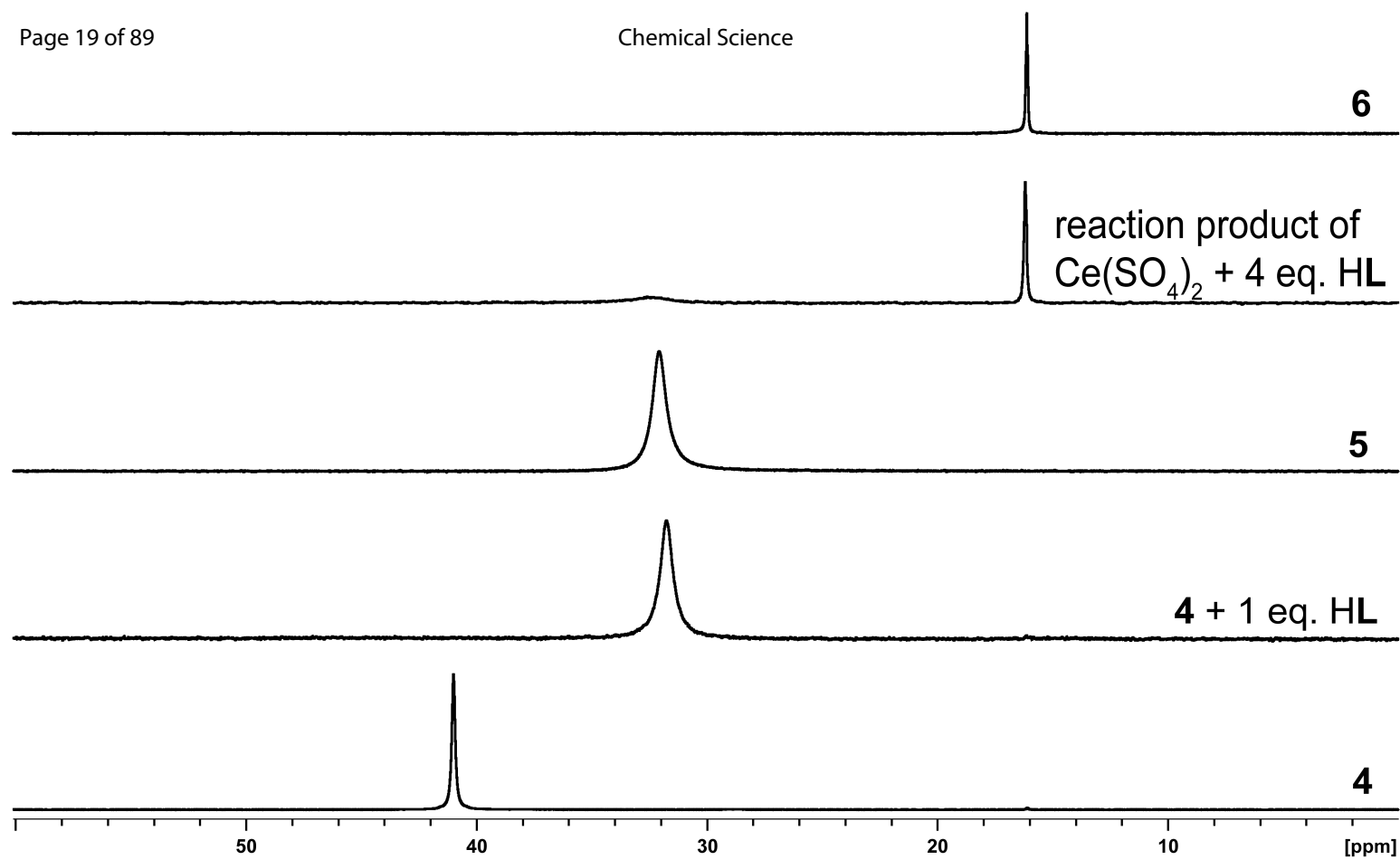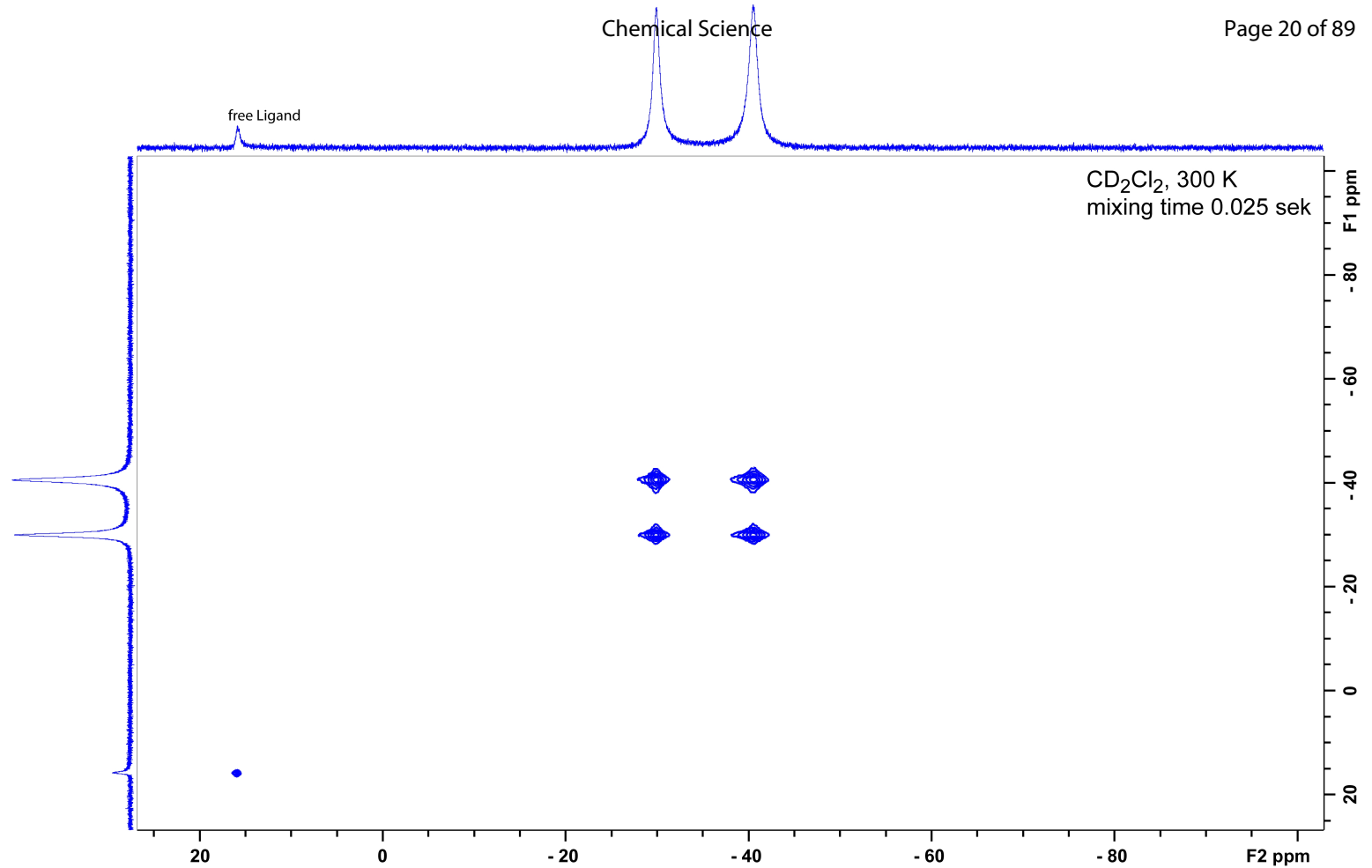
0.25 : 0.75

CD$_2$Cl$_2$ + CD$_3$CN

0.45 : 0.55

CD$_2$Cl$_2$

Same local structure

199x104mm (300 x 300 DPI)

H
C
N
O
P
Ce

[CeL₃(CH₃CN)]   [CeL₃HL]·CH₃CN·Et₂O

C
N
O
P
Ce
Th/U/Np

[CeL$_4$]·2CH$_3$CN·4H$_2$O

[ThL$_4$]·3CH$_3$CN·4H$_2$O

[UL$_4$]·3CH$_3$CN·4H$_2$O

[NpL$_4$]·3CH$_3$CN·4H$_2$O

[UL$_4$]·3CH$_3$CN·4H$_2$O

[UL$_4$]

[UL$_4$]·CH$_2$Cl$_2$

[UL$_4$]
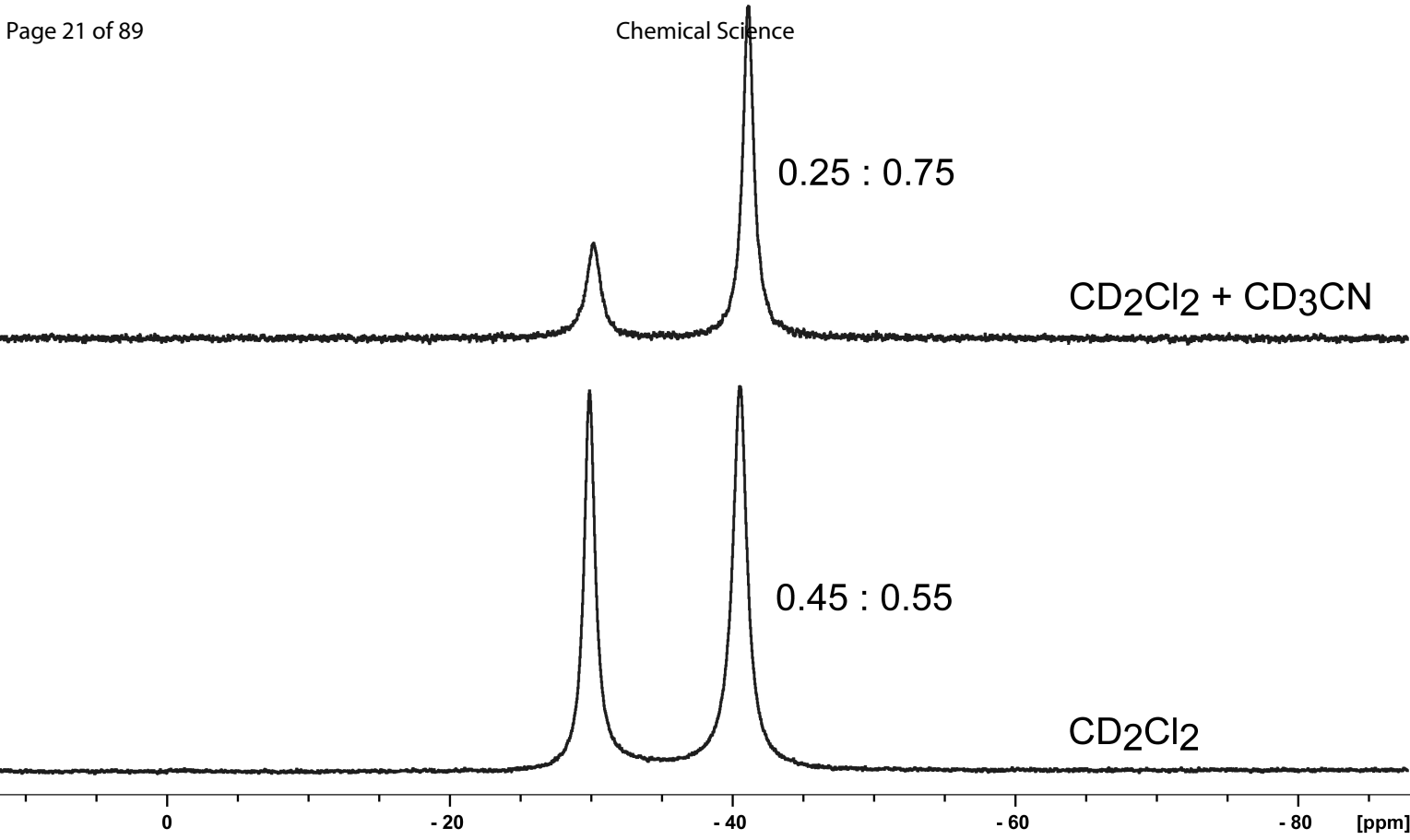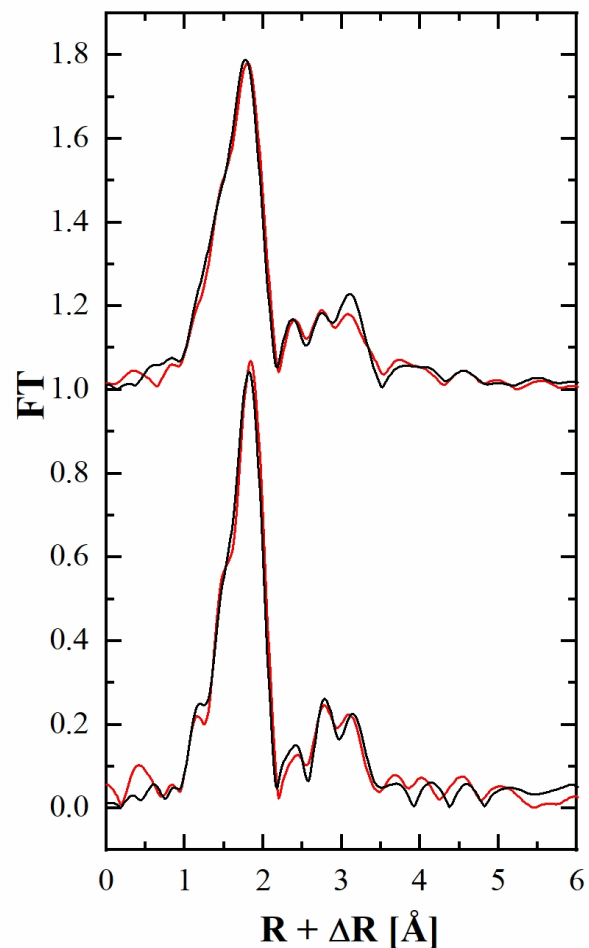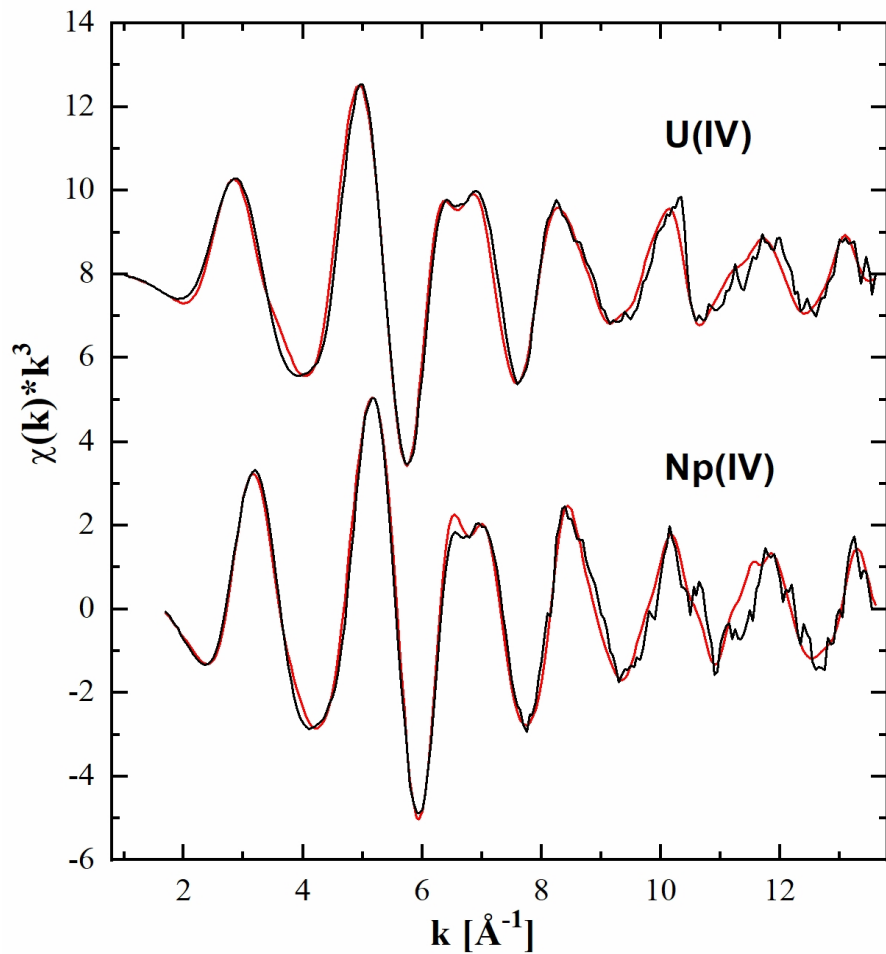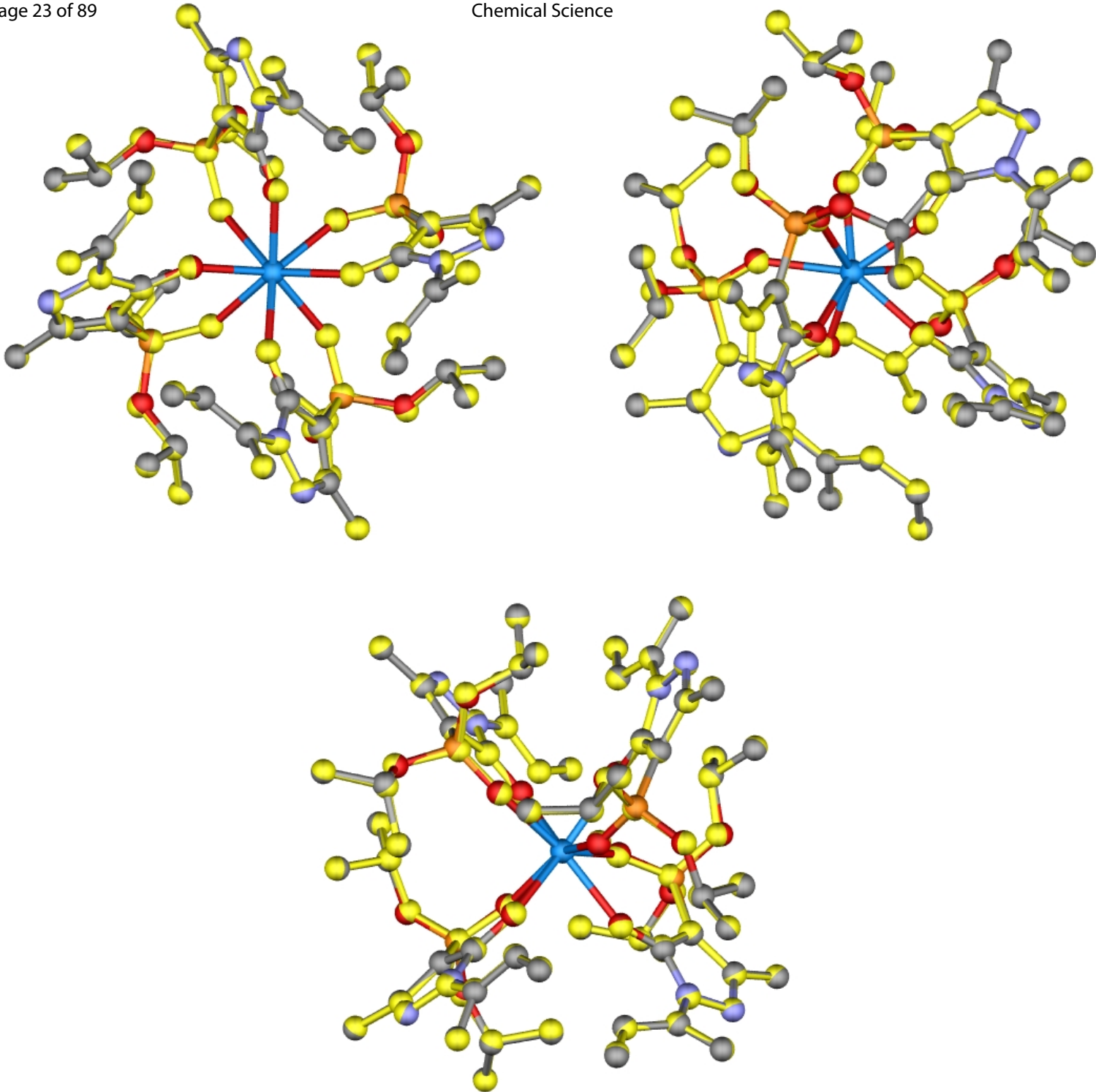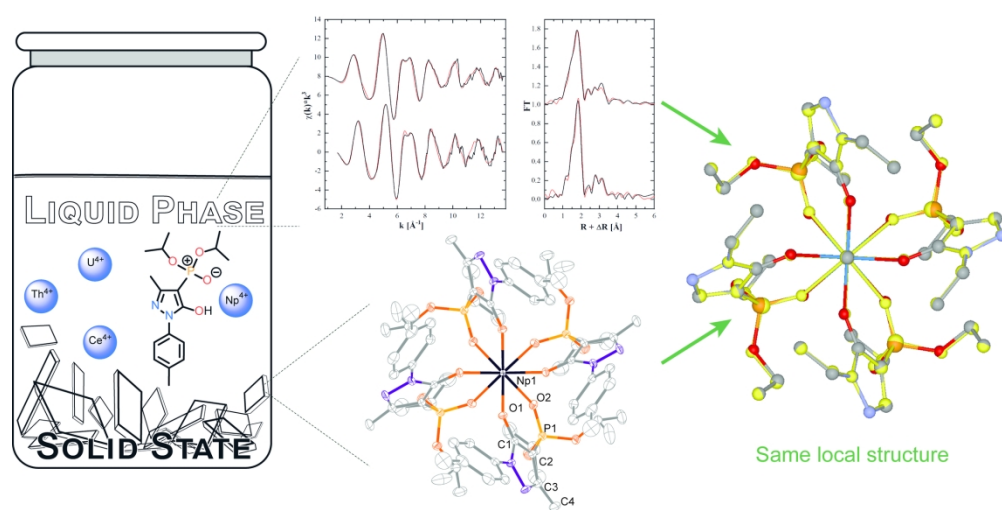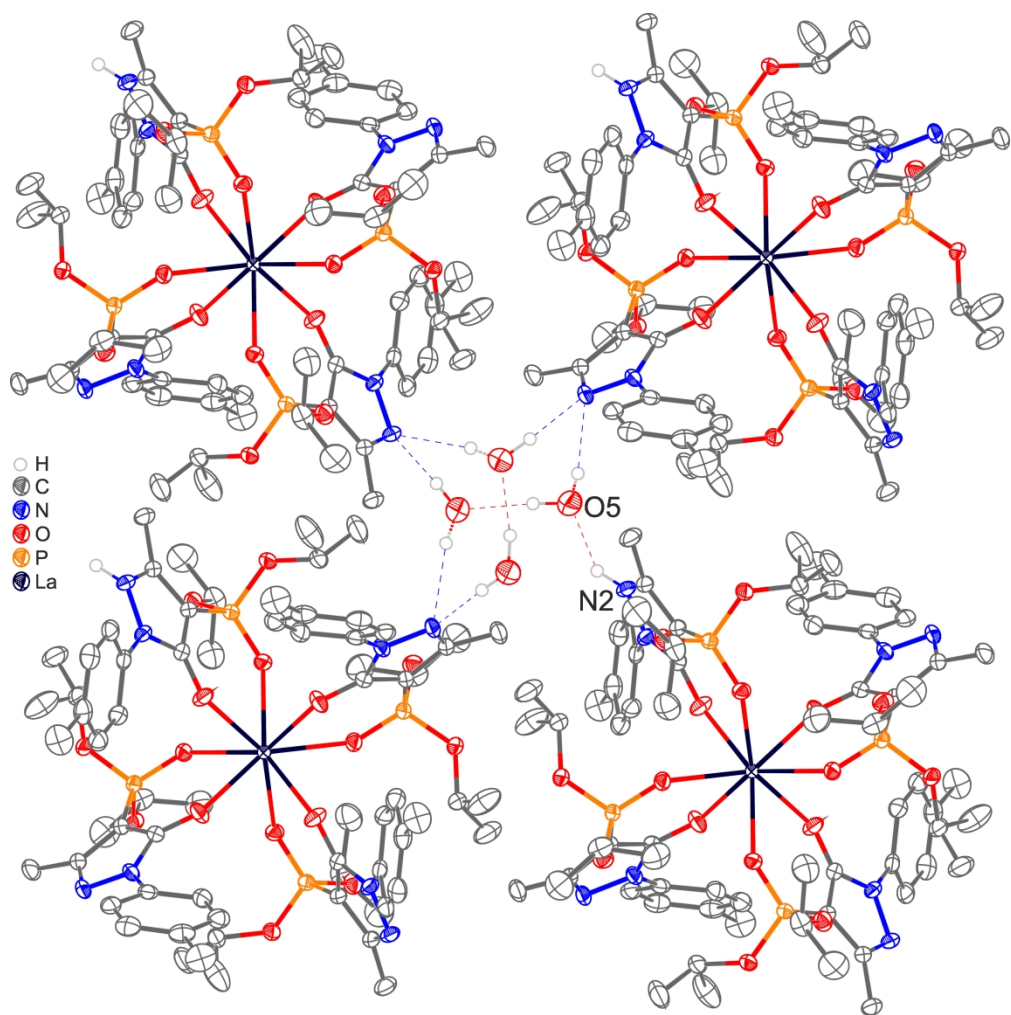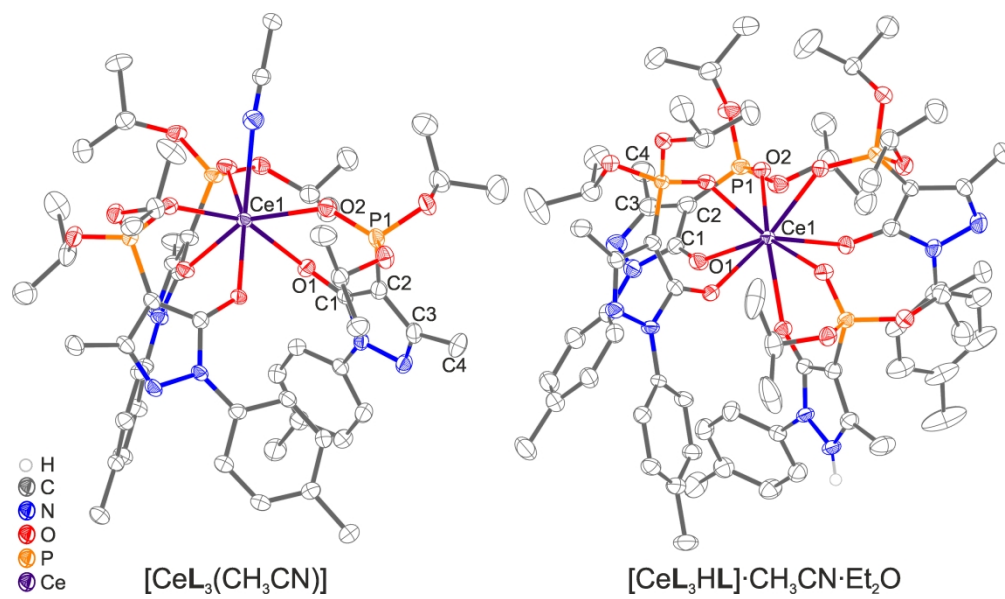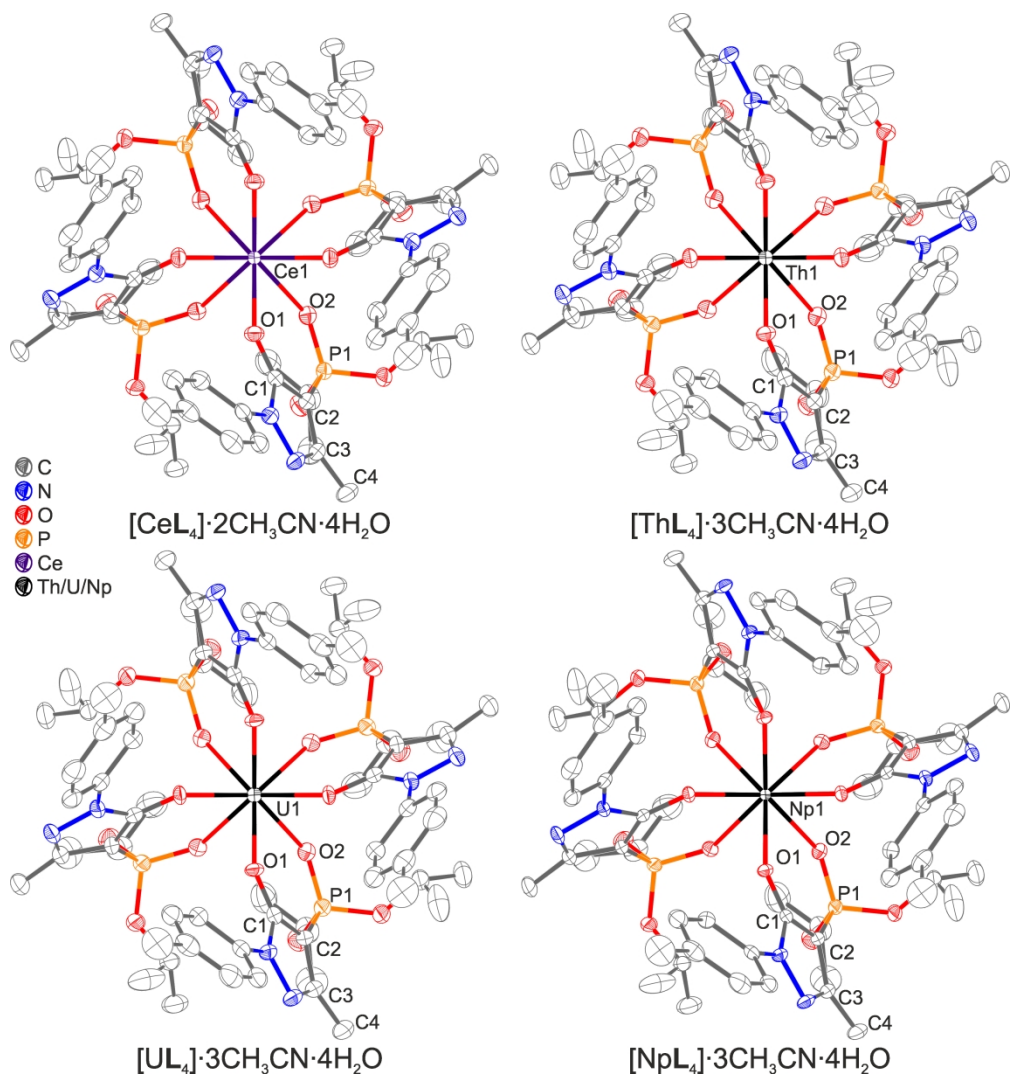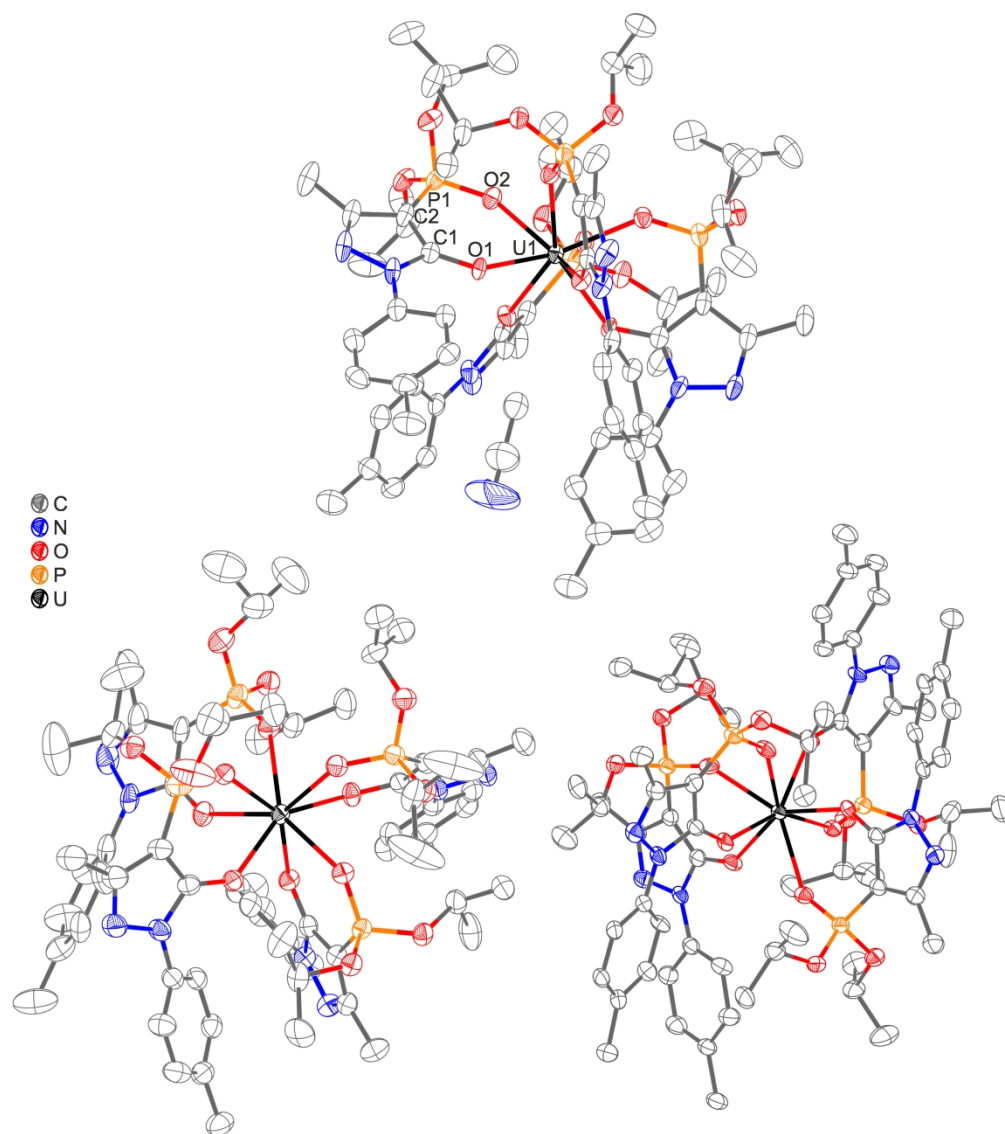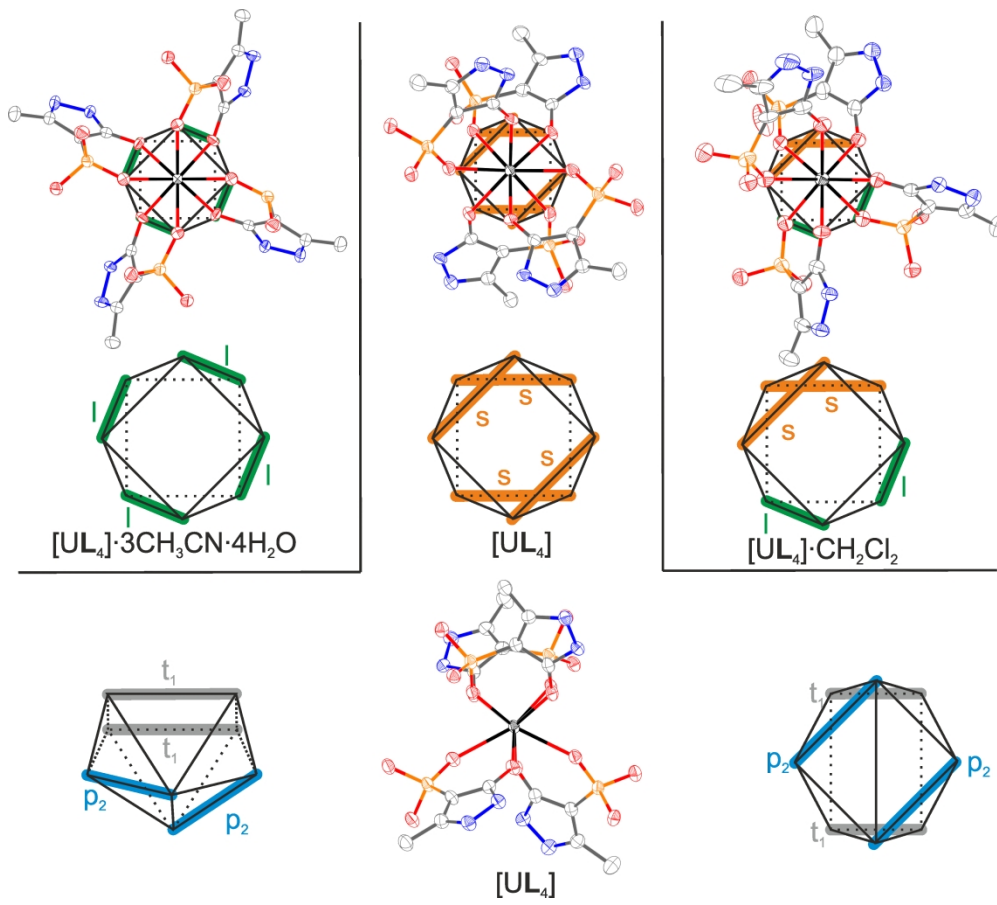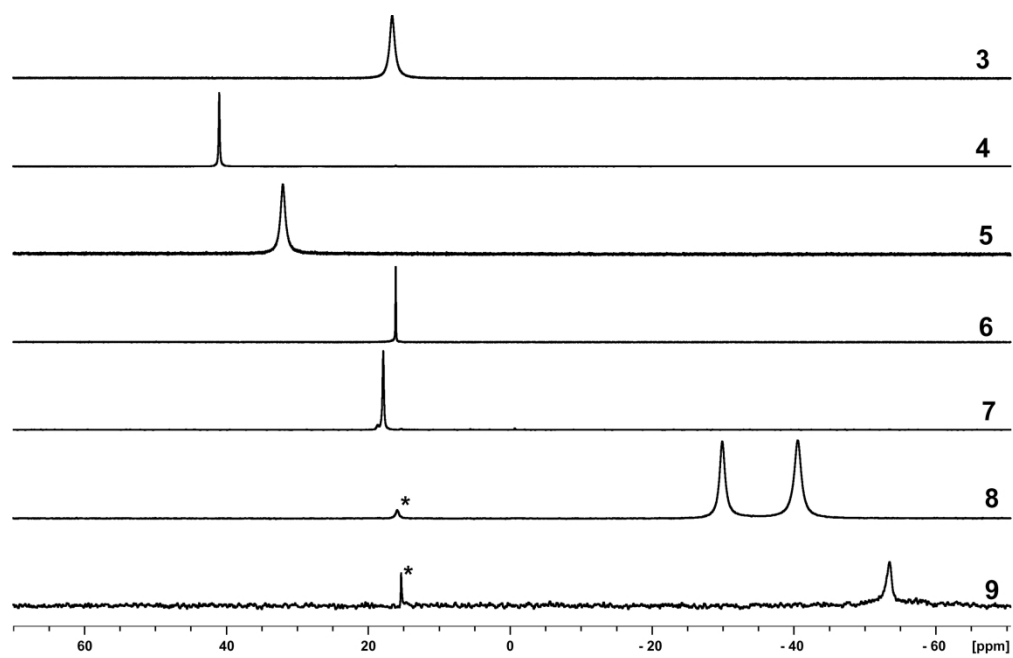
239x152mm (300 x 300 DPI)

239x147mm (300 x 300 DPI)

free Ligand

CD$_2$Cl$_2$, 300 K
mixing time 0.025 sek
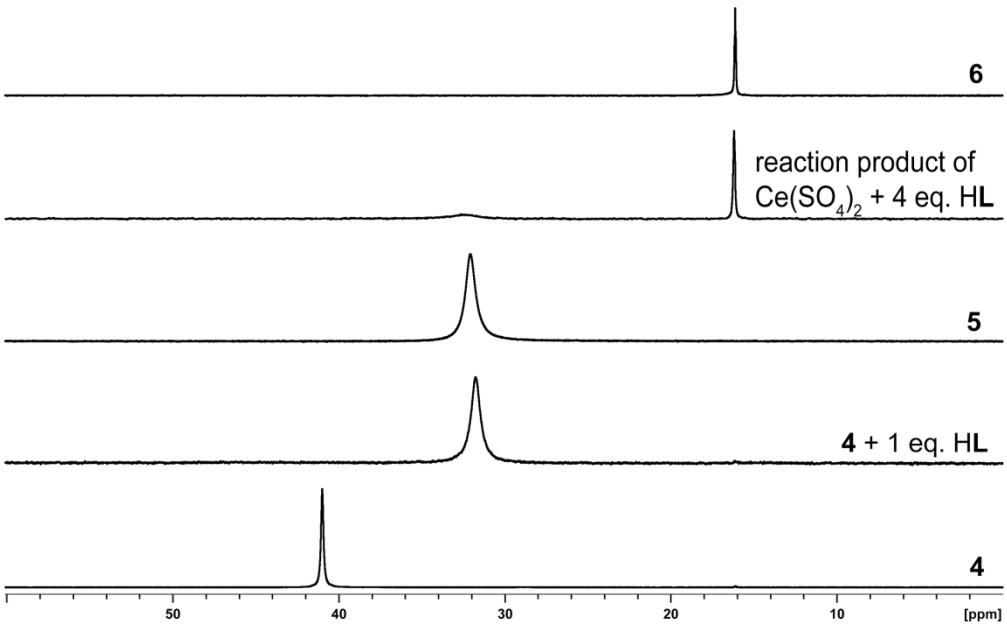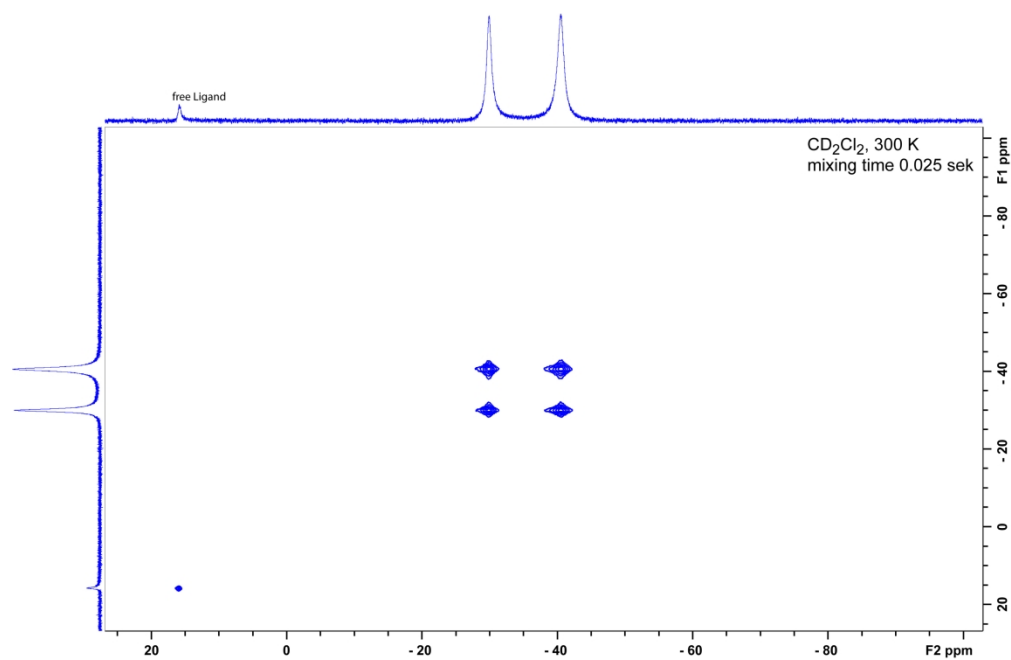
246x159mm (300 x 300 DPI)
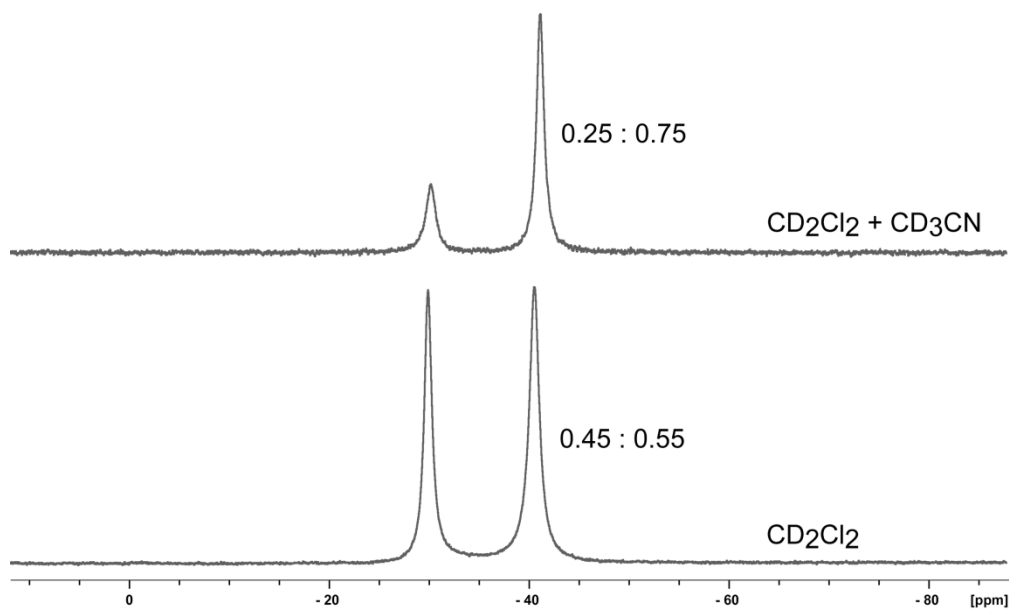
238x142mm (300 x 300 DPI)
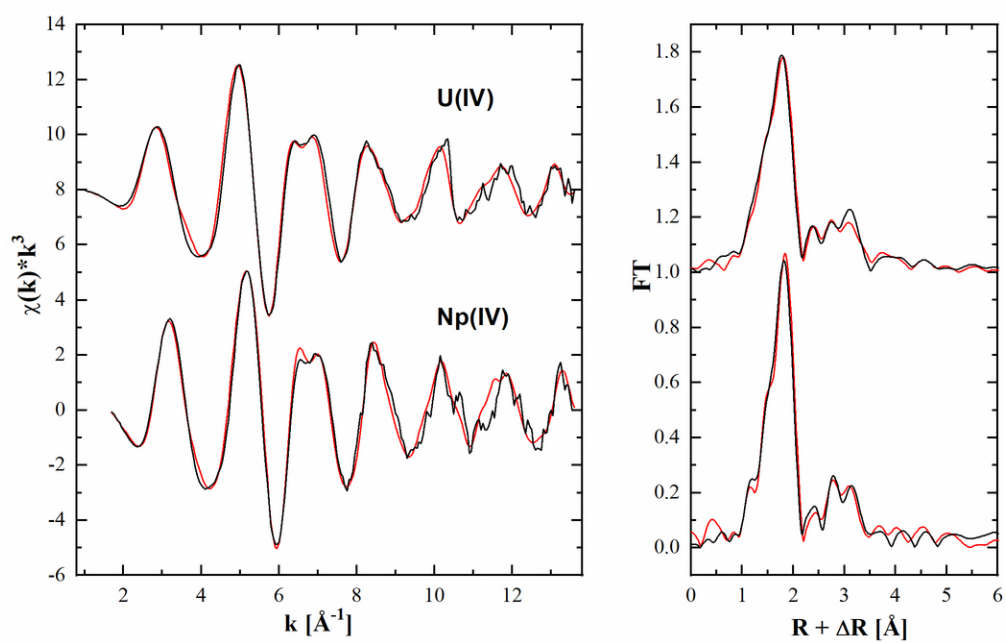
88x60mm (300 x 300 DPI)
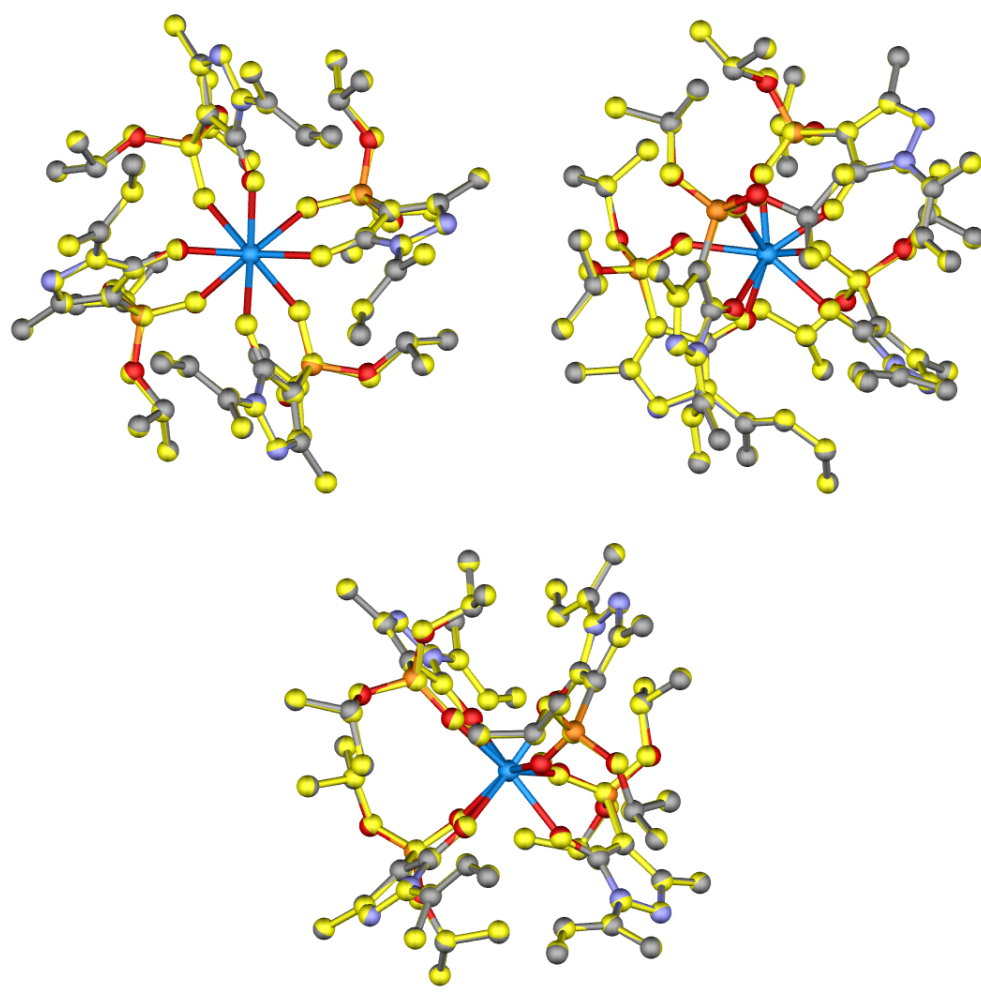
Coordination of Trivalent Lanthanum and Cerium, and Tetravalent Cerium and Actinides (An = Th(IV), U(IV), Np(IV)) by a 4-Phosphoryl 1H-Pyrazol-5-olate Ligand in Solution and the Solid State

Jianfeng Zhang,[a] Marco Wenzel,[a] Kathleen Schnaars,[a] Felix Hennersdorf,[a] Kai Schwedtmann,[a] Juliane März,[b] André Rossberg,[b] Peter Kaden,[b] Florian Kraus,[c] Thorsten Stumpf[b] and Jan J. Weigand*[a]

a.   Faculty of Chemistry and Food Chemistry, Technische Universität Dresden, 01062 Dresden, Germany.
b.   Institute of Resource Ecology, Helmholtz-Zentrum Dresden-Rossendorf (HZDR), Bautzner Landstraße 400, 01328 Dresden, Germany.
c.   Department of Chemistry, Philipps-Universität Marburg, 35032 Marburg, Germany.

[*] E-mail: jan.weigand@tu-dresden.de

Table of content

Experimental details

General Considerations: If not stated differently, all manipulations were performed with HPLC grade, analytical grade or technical grade reagents and solvents, which were used without further purification. The used starting materials were purchased from SIGMA-ALDRICH, FLUKA, MERCK, VWR, TCI, ABCR CHEMICALS, ACROS, CARL ROTH or WAKO.

Manipulations under dry, oxygen-free conditions were performed in a Glovebox MB Unilab or using *Schlenk* technique under an atmosphere of purified nitrogen. All glassware was oven-dried at 160°C prior to use. Dry, oxygen-free solvents (CH_2Cl_2, CH_3CN, C_6F_6 (distilled from CaH_2), toluene, Et_2O (distilled from potassium)) were employed. Anhydrous deuterated acetonitrile (CD_3CN), dichloromethane (CD_2Cl_2), chloroform ($CDCl_3$) and methanol (CD_3OD) were purchased from Sigma-Aldrich or Deutero. All distilled and deuterated solvents were stored over molecular sieves (4 Å: CH_2Cl_2, CD_2Cl_2, $CDCl_3$, CD_3OD, toluene, Et_2O, C_6F_6; 3 Å: CH_3CN, CD_3CN)). Dry, oxygen-free CH_2Cl_2 was obtained by distillation from CaH_2. The obtained anhydrous solvents were stored over 4 Å molecular sieves.

NMR spectra were measured on a Bruker AVANCE III HD Nanobay, 400 MHz UltraSield (^{1}H (400.13 MHz), ^{13}C (100.61 MHz), ^{31}P (161.98 MHz)) or on a Bruker AVANCE III HDX, 500 MHz Ascend (^{1}H (500.13 MHz), ^{13}C (125.75 MHz), ^{31}P (202.45 MHz)), or on a Varian Inova 400, 400 MHz Oxford magnet (^{1}H (399,89 MHz), ^{13}C (100.56 MHz), ^{31}P (161.87 MHz)) installed in a radioactive controlled laboratory. All ^{13}C NMR spectra were exclusively recorded with composite pulse decoupling. Reported numbers assigning atoms in the ^{13}C spectra were indirectly deduced from the cross-peaks in 2D correlation experiments (HMBC, HSQC). Chemical shifts were referenced the respective solvent to δ = 7.26 ppm (^{1}H), 77.16 ppm (^{13}C) for $CDCl_3$, δ = 5.32 ppm (^{1}H), 53.84 ppm (^{13}C) for CD_2Cl_2, δ = 3.31 ppm (^{1}H), 49.00 ppm (^{13}C) for CD_3OD)[1] and $\delta_{H3PO4(85\%)}$ = 0.00 ppm (^{31}P, externally). Chemical shifts (δ) are reported in ppm. Coupling constants (J) are reported in Hz. Infrared (IR) and Raman spectra were recorded at ambient temperature using a Bruker Vertex 70 instrument equipped with a RAM II module (Nd-YAG laser, 1064 nm). The Raman intensities are reported in percent relative to the most intense peak and are given in parenthesis. An ATR unit (diamond) was used for recording IR spectra. The intensities are reported relative to the most intense peak and are given in parenthesis using the following abbreviations: vw = very weak, w = weak, m = medium, s = strong, vs = very strong. Elemental analyses were performed on a Vario MICRO cube Elemental Analyzer by Elementar Analysatorsysteme GmbH in CHNS modus. For the mass spectrometry experiments a waters ACQUITY UPLC H-Class system in combination with an ACQUITY TQ Detector V4.1 SCN849 SCN896 was used. MassLynx V4.1 SCN849 SCN896 served as evaluation software. The required ionization was provided by the electrospray method (ESI). As diluent for the samples served an acetonitrile water mixture containing both solvents in a 70:30 (acetonitrile: water) ratio and additionally 0.1% of formic acid.

Synthesis of Diisopropyl (5-hydroxy-3-methyl-1-(p-tolyl)-1H-pyrazol-4-yl)phosphonate (HL)

The 4-phosphoryl pyrazolone ligand **HL** has been synthesised in 3 steps by adoption of procedure reported in the literature (Scheme S1).[2-4]
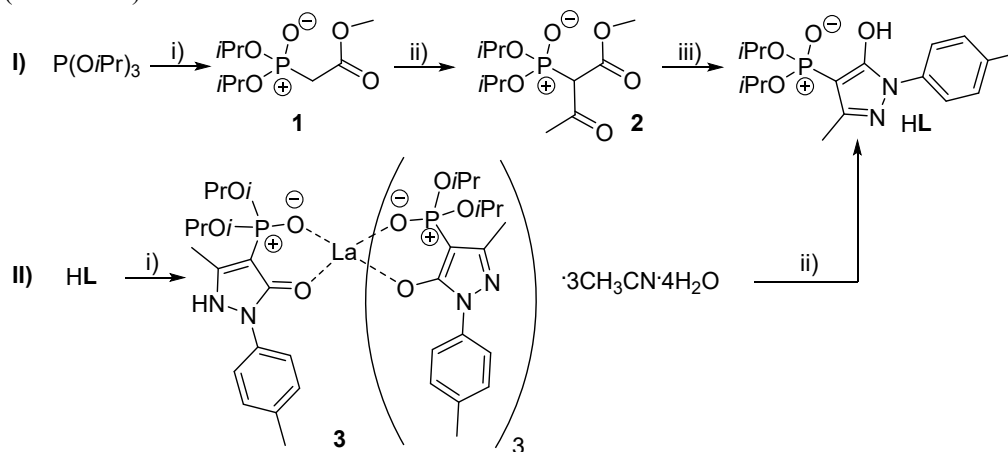
Scheme S1: Synthesis of the 4-phosphoryl pyrazolone **HL**; i) 1.05 eq methyl bromoacetate, 120 °C, neat, 4 h 98% with a purity of 92%; ii) 1.05 eq. $MgCl_2$, 3.5 eq. Et_3N, 1.95 eq. acetyl chloride, CH_2Cl_2, 20°C, 66%; iii) 1.1 eq. *p*-tolylhydrazine hydrochloride, 2.0 eq. K_2CO_3, H_2O, 2 h reflux, r.t. 12 h, 67% in a 91% purity; **II:** purification of

H**L** *via* **3** and subsequent back extraction; i) LaCl$_3$·7H$_2$O, NaOH, CH$_3$CN/water, 96%; ii) CHCl$_3$/H$_2$O, HCl (0.05 M), 99%.

Diisopropyl (5-hydroxy-3-methyl-1-(p-tolyl)-1H-pyrazol-4-yl)phosphonate (HL):
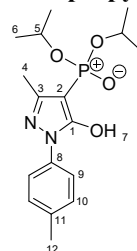
The ligand was synthesized according to a procedure reported by Modranka and coworkers.[2] To a suspension of 2.76 g, 8.25 mmol of methyl 2-(diisopropoxyphosphoryl)-3-oxobutanoate (**2**) in water (15 mL), 1.1 eq (1.47 g; 9.08 mmol in 18 mL H$_2$O) of *p*-tolylhydrazine hydrochloride (98%) were added. The suspension was heated up to 100-110 °C and refluxed for 2 h to yield a brown oil in a yellowish solution. After cooling down to r.t. 2.28 g (16.51 mmol, 2 eq) of potassium carbonate were slowly added. The resulting suspension was heated again to reflux for another 2 h. After cooling down the reaction mixture was stirred at r.t. overnight. The resulting mixture was transferred into a separation funnel and washed with Et$_2$O (3 x 20 ml). The combined aqueous phase were collected and acidified with a 0.5 M HCl to pH = 2, affording a pale yellow oily suspension, which was extracted with EtOAc (3 x 20 ml). The combined organic layers were washed with brine, dried over Na$_2$SO$_4$ and the solvent was evaporated under reduced pressure to yield the product as a brown oil in 91% purity and a yield of 2.14 g, 67%. All classical methods to purify this ligand, including chromatography and recrystallization, failed. However, H**L** readily forms the stable La(III) complex [La**L**$_3$H**L**]·3CH$_3$CH·4H$_2$O (**3**·3CH$_3$CH·4H$_2$O) upon reaction with LaCl$_3$·7H$_2$O at 80°C in an aqueous CH$_3$CN solution in the presence of NaOH (Scheme S1). Therefore, the reaction mixture stirred for 1 h at 80 °C, cooled down to r.t. and put in the fridge for another 2 h. The light yellow powder was collected by filtration giving **3**·3CH$_3$CH·4H$_2$O in 96 % yield. The extraction of a CHCl$_3$ solution of the complex **3**·3CH$_3$CH·4H$_2$O with 0.05 M HCl (pH = 1.3) enables the stripping of La(III) into the aqueous phase, releasing H**L** after removing the solvent in high purity > 99%.

Raman (255 mW, in cm^{-1}): v = 3083 (27), 2983 (51), 2923 (100), 2871 (47), 2734 (31), 1616 (78), 1579 (22), 1570 (22), 1531 (28), 1516 (29), 1452 (35), 1427 (20), 1402 (25), 1384 (22), 1369 (29), 1346 (28), 1315 (22), 1292 (20), 1215 (18), 1184 (17), 1055 (24), 842 (24), 785 (13), 684 (16), 77 (49); **IR (ATR, in cm^{-1})**: v = 2980 (w), 2928 (vw), 1614 (vw), 1531 (m), 1514 (m), 1483 (vw), 1466 (w), 1450 (w), 1416 (w), 1387 (w), 1375 (w), 1348 (vw), 1273 (vw), 1180 (m), 1155 (m), 1103 (w), 1055 (vw), 978 (vs), 939 (w), 887 (m), 841 (vw), 818 (m), 775 (m), 750 (m), 714 (w), 683 (m), 648 (w), 636 (w), 611 (w), 577 (s), 565 (s), 548 (w), 528 (w), 507 (m), 494 (w), 442 (w), 422 (w); **^{1}H NMR (CDCl$_3$, in ppm)**: δ = 1.25 (6H, d, $^3J_{HH}$ = 6.3 Hz, H6a), 1.37 (6H, d, $^3J_{HH}$ = 6.2 Hz, H6b), 2.25 (3H, d, $^4J_{HP}$ = 0.7 Hz, H4), 2.34 (3H, s, H12), 4.59 (2H, d sept, $^3J_{HP}$ = 8.2 Hz, $^3J_{HH}$ = 6.2 Hz, H5), 7.20 (2H, d, $^3J_{HH}$ = 8.3 Hz, H10), 7.61-7.64 (2H, m, H9); **^{13}C{^{1}H} NMR (CDCl$_3$, in ppm)**: δ = 13.9 (1C, s, C4), 21.0 (1C, s, C12), 23.8 (2C, d, $^3J_{CP}$ = 5.2 Hz, C6a), 24.1 (2C, d, $^3J_{CP}$ = 3.9 Hz, C6b), 71.4 (2C, d, $^2J_{CP}$ = 4.9 Hz, C5), 85.0 (1C, d, $^1J_{CP}$ = 218.3 Hz, C2), 121.4 (2C, s, C9), 129.7 (2C, s, C10), 135.4 (1C, s, C8), 136.3 (1C, s, C11), 149.2 (1C, d, $^2J_{CP}$ = 10.1 Hz, C3), 158.9 (1C, d, $^2J_{CP}$ = 23.2 Hz, C1); **^{31}P{^{1}H} NMR (CDCl$_3$, in ppm)**: δ = 15.3 (s); **^{31}P{} NMR (CDCl$_3$, in ppm)**: δ = 15.3 (t, $^3J_{PH}$ = 8.3 Hz); **elemental analysis (in %)**: calculated for C$_{17}$H$_{25}$N$_2$O$_4$P: C: 57.95, H: 7.15 N: 7.95, found: C: 58.09, H: 6.96, N: 8.14.

Methyl 2-(diisopropoxyphosphoryl)acetate (1):
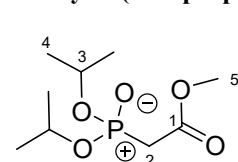
The synthesis of **1** was performed according to the procedure reported by Hubbard and Miller[3] in dried N$_2$ atmosphere. Trisisopropyl phosphite (86.5 ml, 0.35 mol) was heated to 120 °C and 35.5 ml (0.36 mol, 1.05 eq) methyl bromoacetate were slowly added over a period of 2 h while keeping the temperature at 120 °C. Simultaneously, the generated 2-bromopropane was distilled from the reaction mixture at about 35 - 50 °C inner temperature in the distillation apparatus. After the addition of methyl bromoacetate was completed the amount of evolving 2-bromopropan decreased and the reaction mixture was kept at a temperature of 120 - 130 °C for additional 2 h. After cooling down residual volatiles were removed under reduced pressure to yield in 87.82 g (98% yield) of a colourless oil containing the crude produce **1** in 92 % purity. The product was used without further purification.

Raman (255 mW, in cm^{-1}): v = 3047 (20), 3029 (21), 3022 (23), 2985 (62), 2943 (100), 2929 (89), 2885 (35),

2877 (36); **IR (ATR, in cm^{-1})**: v = 2982 (vw), 2955 (vw), 2937 (vw), 1740 (m), 1468 (vw), 1454 (vw), 1437 (vw), 1387 (w), 1375 (w), 1254 (s), 1213 (w), 1178 (w), 1142 (w), 1119 (w), 1103 (m), 976 (vs), 905 (w), 889 (m), 820 (w), 764 (w), 716 (vw), 617 (w), 501 (m), 419 (w); **^{1}H NMR (CDCl$_3$, in ppm):** δ = 1.27 (12H, d, $^3J_{HH}$ = 6.2 Hz, H4), 2.86 (2H, d, $^2J_{HP}$ = 21.8 Hz, H2), 3.66 (3H, s, H5), 4.68 (2H, d sept, $^3J_{HP}$ = 7.6 Hz, $^3J_{HH}$ = 6.2 Hz, H3); **^{13}C{^{1}H} NMR (CDCl$_3$, in ppm):** δ = 23.8 (2C, d, $^3J_{CP}$ = 4.9 Hz, C4a), 24.0 (2C, d, $^3J_{CP}$ = 4.2 Hz, C4b), 35.3 (1C, d, $^1J_{CP}$ = 135.3 Hz, C2), 52.3 (1C, s, C5), 71.5 (2C, d, $^2J_{CP}$ = 6.5 Hz, C3), 166.4 (1C, d, $^2J_{CP}$ = 6.3 Hz, C1); **^{31}P{^{1}H} NMR (CDCl$_3$, in ppm)**: δ = 17.3 (s); **^{31}P{} NMR (CDCl$_3$, in ppm)**: δ = 17.3 (tt, $^2J_{PH}$ = 21.5 Hz, $^3J_{PH}$ = 12.1 Hz).

Methyl 2-(diisopropoxyphosphoryl)-3-oxobutanoate (2):
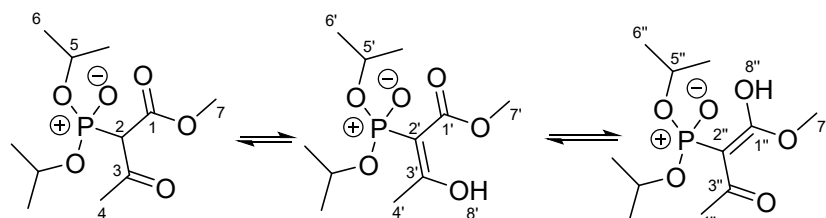
The synthesis of the precursor **2** was performed on the basis of a procedure reported by *Corbel* and coworkers[4] under an atmosphere of dried N$_2$ in dry solvents. To a 25 mL CH$_2$Cl$_2$ suspension of MgCl$_2$ (98%, 6.1176 g, 62.97 mmol) a solution (20 mL CH$_2$Cl$_2$) of 15.003 g (57.88 mmol) methyl 2-(diisopropoxyphosphoryl)acetate (**1**) (92% purity) was added, followed by the addition of 2 eq. Et$_3$N (99.5%, 17.6 mL, 125.92 mmol). The reaction mixture was stirred for 30 min at room temperature. Subsequent the temperature of the reaction mixture was reduce to 20 °C using an external water cooling and 1.1 eq acetyl chloride (4.94 mL, 69.25 mmol) were added slowly. The colour of the reaction mixture turned yellow. After 15 min of stirring a part of the solution was taken, acidified with 1 M HCl and the organic phase was separated, dried over Na$_2$SO$_4$ and monitored by ^{31}P{}-NMR spectroscopy. The reaction was brought to completeness by sequential addition of an excess of 1 eq. (8.81 mL, 62.97 mmol) and then 0.5 eq. (4.41 mL, 31.48 mmol) of Et$_3$N and 0.55 eq. (2.47 mL, 34.63 mmol) and 0.275 .eq (1.24 mL, 17.31 mmol) of the acetyl chloride at intervals of 15 min. The resulting red orange suspension was quenched by 1 M HCl (2 eq.) and extracted 3 times with CH$_2$Cl$_2$. The combined organic phases were dried over Na$_2$SO$_4$, filtered and the solvent was evaporated under reduced pressure. The crude product was purified by column chromatography (EtOAc: *n*-hexane, 4:1) to yield a yellow oil containing a mixture of the different keto-enol-tautomer's of the target molecules. The product degrades slowly if not stored dry and in an inert atmosphere.

Yield: 10.6633 g, 66% **Raman (255 mW, in cm^{-1})**: v = 2983 (49), 2939 (100), 2927 (100), 2875 (31), 2738 (9), 1712 (10), 1587 (6), 1454 (16), 1355 (7), 887 (7), 734 (7), 129 (6), 69 (25); **IR (ATR, in cm^{-1})**: v = 2982 (vw), 2937 (vw), 1744 (vw), 1709 (m), 1591 (w), 1466 (vw), 1437 (w), 1412 (w), 1385 (w), 1375 (m), 1329 (w), 1242 (s), 1180 (w), 1144 (w), 1103 (m), 1080 (m), 982 (vs), 899 (w), 887 (w), 851 (vw), 812 (vw), 781 (w), 771 (w), 737 (vw), 625 (w), 598 (w), 534 (m), 449 (w), 422 (w), 413 (w); **^{1}H NMR (CDCl$_3$, in ppm):** δ = 1.22-1.26 (6H, m, $^3J_{HH}$ = 6.2 Hz, H6a/H6′a/H6′′a), 1.31-1.34 (6H, m, $^3J_{HH}$ = 6.2 Hz, H6b/H6′b/H6′′b), 2.39 (3H, s, H4), 2.43 (3H, d, $^4J_{HP}$ = 0.7 Hz, H4′), 2.51 (3H, d, $^4J_{HP}$ = 0.8 Hz, H4′′), 3.69 (3H, s, H7′), 3.76 (3H, s, H7), 3.79 (3H, s, H7′′), 4.18 (1H, d, $^2J_{HP}$ = 23.8 Hz, H2), 4.57 (2H, d sept, $^3J_{HP}$ = 8.4 Hz, $^3J_{HH}$ = 6.2 Hz, H5′), 4.60 (2H, m, H5′′), 4.80 (2H, m, H5), 13.81 (1H, s, H8′), 14.55 (1H, s, H8′′); **^{13}C{^{1}H} NMR (CDCl$_3$, in ppm):** δ = 22.6 (1C, s, C4′′), 23.0 (1C, s, C4′a), 23.1 (1C, s, C4′b), 23.6-24.2 (4C, m, C6/C6′/C6′′), 30.0 (1C, s, C4), 51.1 (1C, s, C7′), 52.1 (1C, s, C7′′), 52.9 (1C, s, C7), 62.7 (1C, d, $^1J_{CP}$ = 126.2 Hz, C2), 70.4 (2C, d, $^2J_{CP}$ = 5.4 Hz, C5′′), 71.9 (2C, d, $^2J_{CP}$ = 5.2 Hz, C5′), 72.8 (1C, d, $^2J_{CP}$ = 6.9 Hz, C5a), 72.9 (1C, d, $^2J_{CP}$ = 6.8 Hz, C5b), 89.5 (1C, d, $^1J_{CP}$ = 178.7 Hz, C2′), 92.0 (1C, d, $^1J_{CP}$ = 206.0 Hz, C2′′), 164.9 (1C, d, $^2J_{CP}$ = 5.5 Hz, C1), 166.8 (1C, d, $^2J_{CP}$ = 9.2 Hz, C1′), 173.8 (1C, d, $^2J_{CP}$ = 9.2 Hz, C1′′), 187.9 (1C, d, $^2J_{CP}$ = 6.0 Hz, C3′), 189.6 (1C, d, $^2J_{CP}$ = 21.7 Hz, C3′′), 196.6 (1C, d, $^2J_{CP}$ = 5.0 Hz, C3); **^{31}P{^{1}H}NMR (CDCl$_3$, in ppm):** δ = 11.2 (s, P), 14.5 (s, P′′), 23.0 (s, P′); **^{31}P{} NMR (CDCl$_3$, in ppm)**: δ = 11.2 (td, $^2J_{PH}$ = 23.7 Hz, $^3J_{PH}$ = 7.6 Hz, P), 14.5 (t, $^3J_{PH}$ = 8.3 Hz, P′′), 23.0 (t, $^3J_{PH}$ = 8.3 Hz, P′); **ESI-MS (in m/z)**: 281.3 [M+H]$^+$, 303.3 [M+Na]$^+$

Synthesis of [LaL₃HL]·3CH₃CN·4H₂O (3·3CH₃CN·4H₂O)
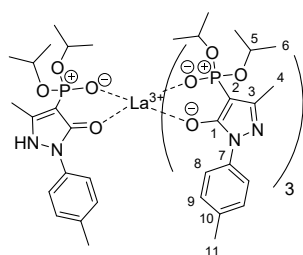
To prepare the La(III) complex **3**·3CH₃CN·4H₂O ([LaL₃HL]·3CH₃CN·4H₂O) 377.4 mg (1.00 mmol, 4 eq) of HL (91%) dissolved in 8 mL CH₃CN, 30.0 mg (0.75 mmol, 3 eq) of NaOH (99 %) and 94.4 mg (0.25 mmol, 1 eq.) of LaCl₃·7H₂O (98%) were dissolved in 1.5 ml and 2.0 ml H₂O, respectively. The NaOH solution was added to HL under stirring. Subsequent, the LaCl₃·7H₂O solution was added into the HL and NaOH mixture dropwise at 80 °C. During the addition of LaCl₃·7H₂O, some light yellow solid precipitated. After the addition was completed, the reaction mixture was stirred for 1 h at 80 °C, cooled down to room temperature, put it in fridge for another 2 h. The light yellow powder was collected after filtration. Suitable crystals for single crystal X-ray diffraction analysis were recrystallized from the acetonitrile and H₂O (6:1) mixture.

Yield: 416.2 mg, 96%, **Raman (80 mW, in cm⁻¹)**: v = 3080 (15), 3039 (14), 3029 (14), 3014 (17), 2979 (32), 2921 (62), 2871 (27), 2730 (16), 1614 (61), 1566 (13), 1516 (38), 1452 (32), 1415 (19), 1375 (34), 1355 (49), 1311 (18), 1294 (31), 1215 (19), 1182 (21), 1143 (13), 1109 (13), 1060 (20), 854 (26), 788 (14), 721 (24), 704 (12), 626 (13), 596 (11), 270 (8), 258 (9), 208 (14), 185 (15), 79 (100); **IR (ATR, in cm⁻¹)**: v = 2976 (w), 2926 (w), 2870 (vw), 1634 (vw), 1616 (w), 1585 (m), 1556 (s), 1514 (s), 1464 (w), 1450 (w), 1421 (m), 1371 (m), 1352 (m), 1310 (w), 1294 (w), 1177 (s), 1142 (w), 1103 (m), 1059 (vw), 972 (vs), 885 (m), 820 (m), 775 (s), 762 162 (m), 739 (m), 717 (w), 704 (w), 644 (w), 625 (m), 590 (vs), 548 (w), 530 (m), 509 (m), 442 (w), 420 (m); **¹H NMR (CD₃OD, in ppm)**: δ = 1.06 (24H, d, ³J_{HH} = 5.2 Hz, H6a), 1.20 (24H, d, ³J_{HH} = 5.9 Hz, H6b), 2.17 (12H, s, H4), 2.21 (12H, s, H11), 4.61 (8H, d sept, ³J_{HP} = 7.7 Hz, ³J_{HH} = 6.3 Hz, H5), 6.95 (8H, s(br), H9), 7.73 (8H, d, ³J_{HH} = 7.7 Hz, H8); **¹³C{¹H} NMR (CD₃OD, in ppm)**: δ = 14.1 (4C, s, C4), 20.9 (4C, s, C11), 24.0 (8C, d, ³J_{CP} = 4.8 Hz, C6a), 24.4 (8C, d, ³J_{CP} = 4.1 Hz, C6b), 71.7 (8C, d, ²J_{CP} = 4.6 Hz, C5), 84.8 (4C, d, ¹J_{CP} = 237.9 Hz, C2), 121.8 (8C, s, C8), 130.0 (8C, s, C9), 135.3 (4C, s, C10), 137.6 (4C, s, C7), 151.4 (4C, d, ²J_{CP} = 14.2 Hz, C3), 166.6 (4C, s(br), C1); **³¹P{} NMR (CD₃OD, in ppm)**: δ = 16.6 (s(br)); **Elemental analysis** for C₇₄H₁₁₄LaN₁₁O₂₀P₄ (**[LaL₃HL]·3CH₃CN·4H₂O**), calculated: C 51.06, N 8.85, H 6.60; found: C 51.15, N 8.56, H 6.35; **ESI-MS (in m/z)**: 1193.3 [M − HL+ H]⁺.
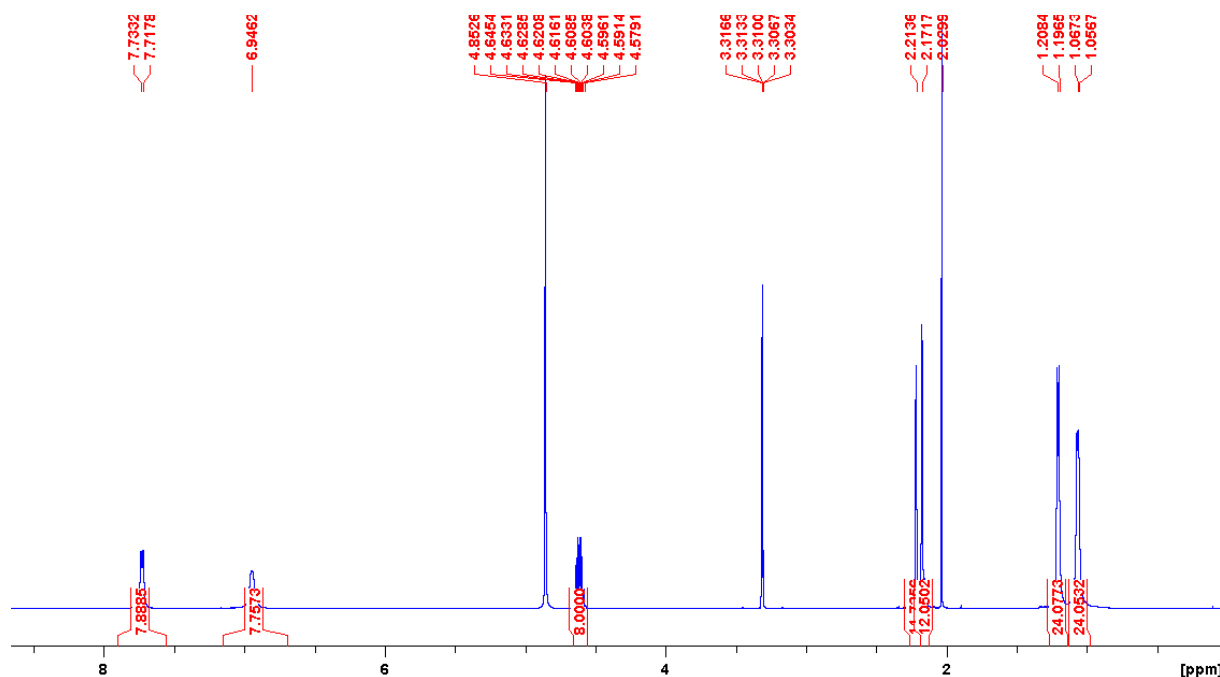
Fig. S1 ¹H NMR spectrum of La(III) complex (CD₃OD, 300 K).
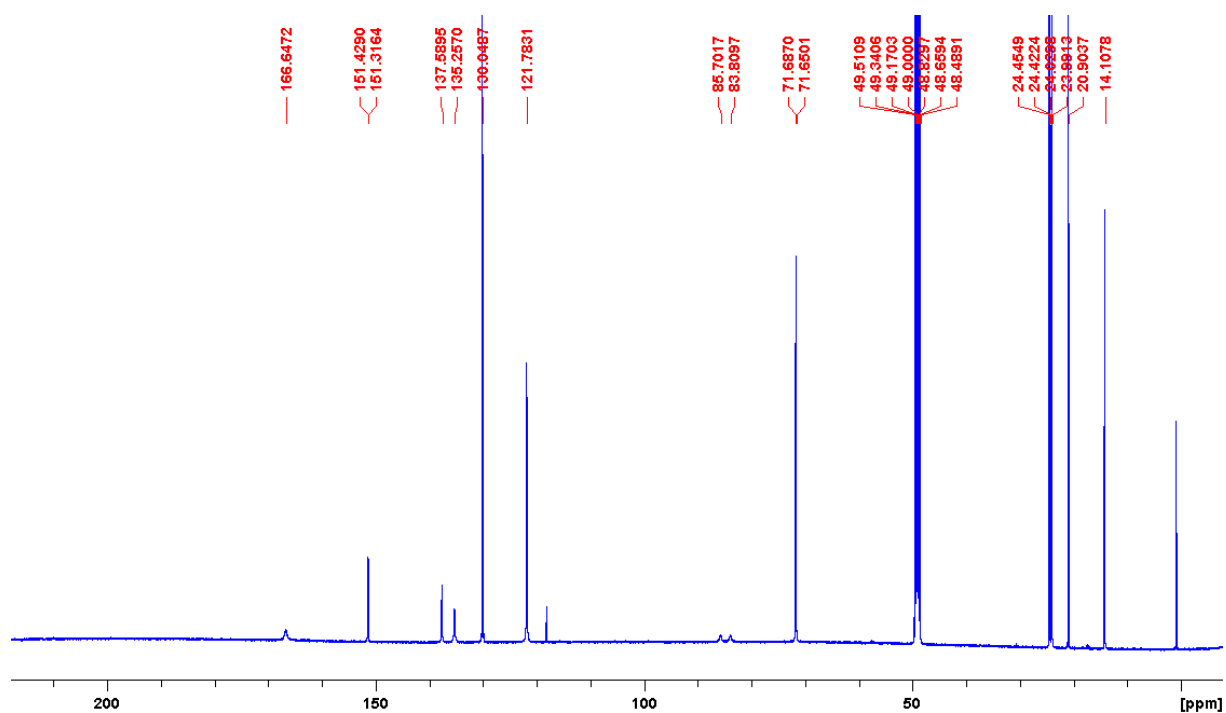
Fig. S2 $^{13}C\{^1H\}$ NMR spectrum of La(III) complex (CD$_3$OD, 300 K).
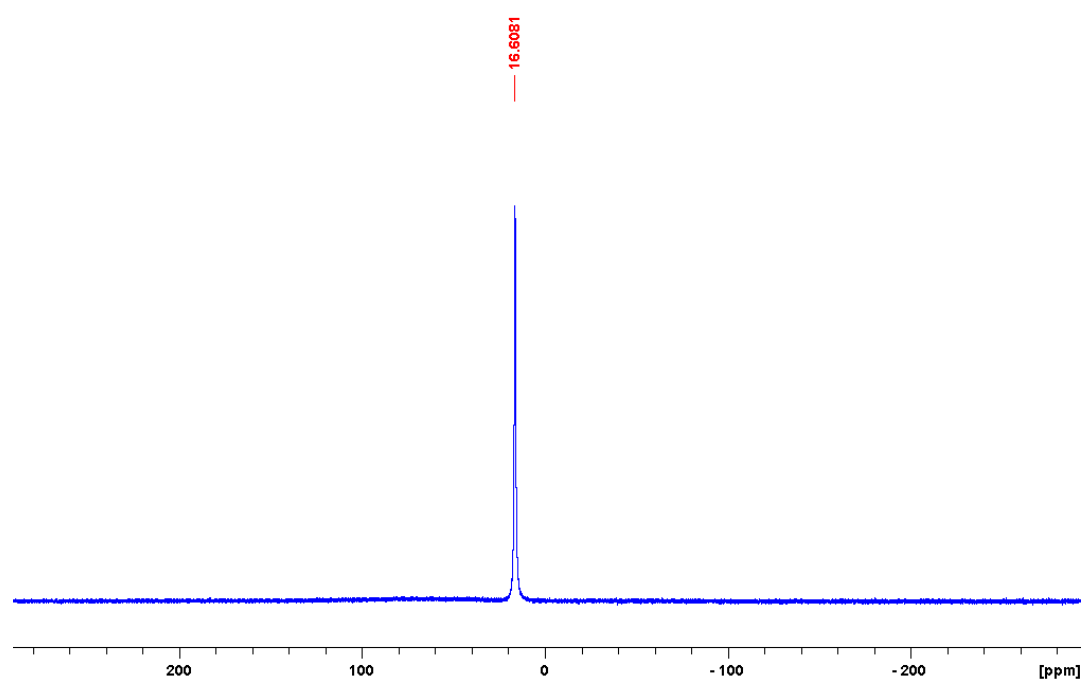
Fig. S3 ^{31}P NMR spectrum of La(III) complex (CD$_3$OD, 300 K).

Synthesis of [CeL₃] (4)
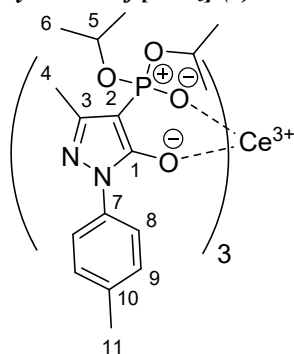
To prepare the Ce(III) complex [Ce**L**₃] (**4**) 335.6 mg (0.90 mmol, 3 eq:) of H**L** (91%) were dissolved in 8 ml acetonitrile and 40.0 mg (0.99 mmol, 3 eq:) of NaOH (99%) in 6 ml degassed H_2O were added under argon atmosphere. The reaction mixture was heated to 80 °C and 87.1 mg (0.15 mmol, 0.5 eq.) $Ce_2(SO_4)_3$ (99.9%) in 6 ml degassed H_2O were added dropwise under stirring. During the addition of $Ce_2(SO_4)_3$, a yellow precipitate is generated which indicates the formation of complex. The reaction mixture was stirred for 1 h at 80 °C, cooled down to room temperature, put in the fridge for 2 h. The yellow precipitate was filtrated, washed with a water/acetonitrile mixture (3:2) and dried overnight.

Yield: 170.5 mg, 49%, **Raman (100 mW, in cm⁻¹)**: v = 3078 (17), 3038 (13), 3016 (14), 2978 (37), 2921 (89), 2871 (27), 2732 (8), 1615 (100), 1516 (48), 1452 (30), 1416 (11), 1377 (60), 1361 (55), 1311 (18), 1298 (40), 1214 (13), 1180 (17), 1143 (7), 1102 (7), 1061 (24), 889 (5), 856 (23), 791 (12), 758 (5), 717 (17), 650 (6), 627 (10), 595 (7), 422 (6), 390 (5), 327 (6); **IR (ATR, in cm⁻¹)**: v = 3649 (vw), 2976 (vw), 2926 (vw), 1615 (vw), 1586 (vw), 1542 (s), 1514 (s), 1423 (m), 1373 (m), 1297 (vw), 1152 (m), 1094 (m), 1060 (vw), 1003 (m), 975 (vs), 888 (w), 854 (vw), 820 (w), 777 (m), 736 (w), 715 (vw), 625 (w), 592 (s), 577 (m), 551 (w), 529 (w), 512 (w), 495 (vw), 421 (vw); **¹H NMR (CD₂Cl₂, in ppm)**: δ = 0.25 (18H, s, H6a), 1.01 (18H, s, H6b), 1.92 (9H, s, H4), 3.77 (9H, s, H11), 5.21 (6H, s, H5), 6.54 (6H, s, H9), 8.16 (6H, s, H8); **¹³C{¹H} NMR (CD₂Cl₂, in ppm)**: δ = 16.7 (3C, s, C4), 20.6 (3C, s, C11), 23.3 (6C, s, C6a), 23.8 (6C, s, C6b), 71.8 (6C, s, C5), 91.2 (3C, d, $^1J_{CP}$ = 228.5 Hz, C2), 121.4 (6C, s, C8), 129.2 (6C, s, C9), 133.9 (3C, s, C10), 139.9 (3C, s, C7), 153.3 (3C, s, C3), 187.7 (3C, s (br), C1); **³¹P{¹H} NMR (CD₂Cl₂, in ppm)**: δ = 41.0 (s); **³¹P{} NMR (CD₂Cl₂, in ppm)**: δ = 41.0 (s); **Elemental analysis** for $C_{51}H_{76}CeN_6O_{14}P_3$ *([CeL₃]·2H₂O)*, calculated: C 49.79, N 6.83, H 6.23; found: C 49.87, N 6.81, H 5.99; **ESI-MS (in m/z)**: 1194.4 [M+H]⁺.
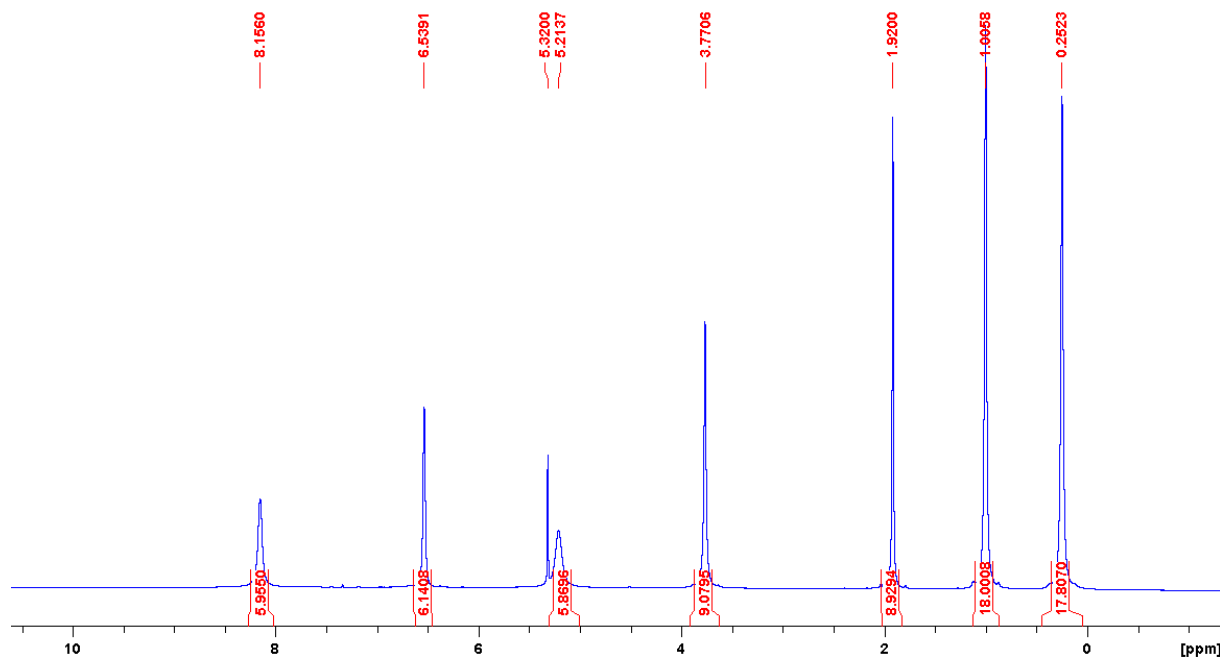
Fig. S4 ¹H NMR spectrum of [Ce**L**₃] complex (CD₂Cl₂, 300 K).
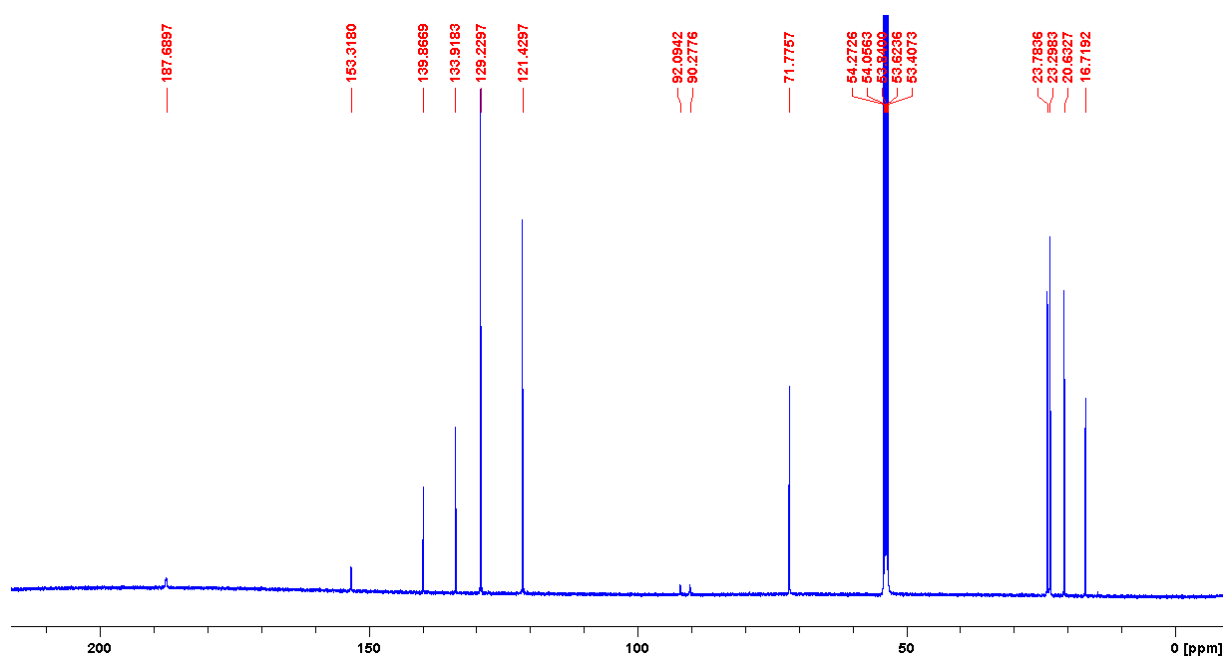
Fig. S5 $^{13}C\{^{1}H\}$ NMR spectrum of [Ce**L**$_3$] complex (CD$_2$Cl$_2$, 300 K).
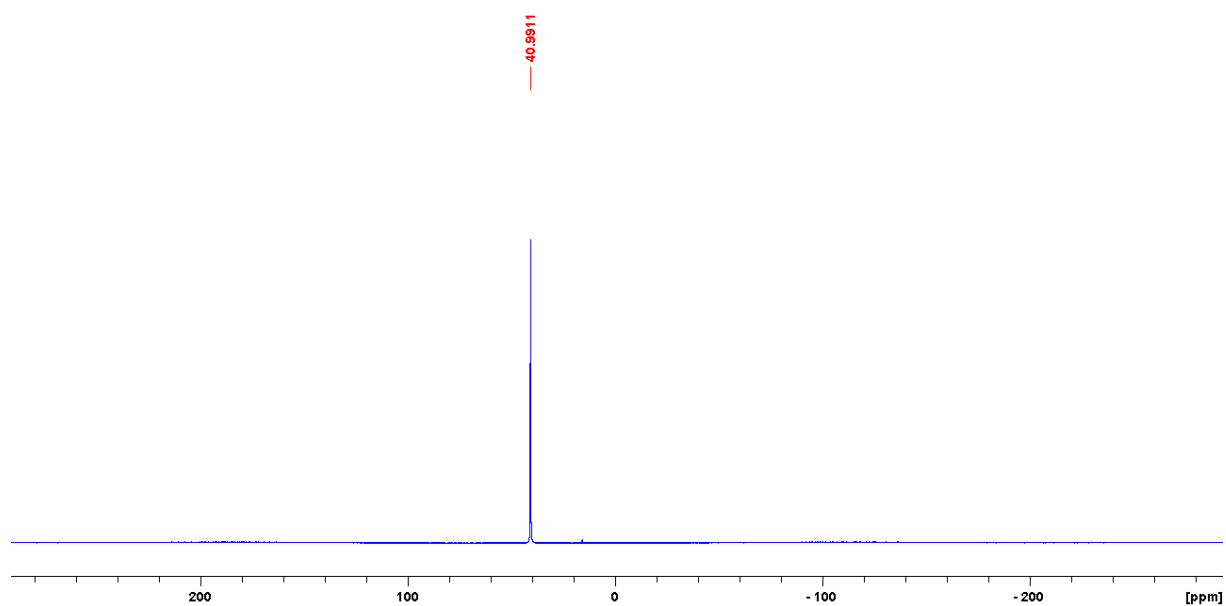
Fig. S6 ^{31}P NMR spectrum of [Ce**L**$_3$] complex (CD$_2$Cl$_2$, 300 K).

Suitable crystals for single crystal X-ray diffraction analysis were obtained by recrystallization in the glove box involving diethyl ether diffusion into a solution of the complex in acetonitrile with the composition [Ce**L**$_3$CH$_3$CN] (CH$_3$CN⊂**4**).

Synthesis of [CeL₃HL]·(5)
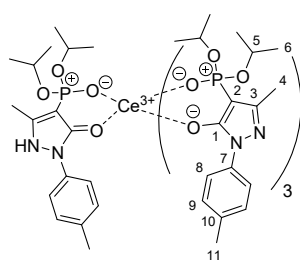
To prepare the complex **5** ([Ce**L₃**H**L**]) 776.7 mg (2.0 mmol, 4 eq.) of H**L** (91%) were dissolved in 16 ml acetonitrile and 59.9 mg (1.5 mmol, 3 eq.) of NaOH (99%) dissolved in 8 ml degassed H_2O were added under argon atmosphere. The reaction mixture was heated to 80 °C and 142.1 mg (0.25 mmol, 0.5 eq.) $Ce_2(SO_4)_3$ (99.9%) dissolved in 8 ml degassed H_2O were added dropwise to the stirred solution. Upon the addition of $Ce_2(SO_4)_3$, light yellow precipitate was formed. The reaction mixture was stirred for another 2 h at 80 °C to complete the reaction, cooled down to room temperature and put in the fridge for another 2 h. The yellow precipitate was filtrated, washed with a water acetonitrile (1:1) mixture and dried overnight.

Yield: 659.4 mg, 85%, **Raman (100 mW, in cm⁻¹)**: v = 3080 (12), 2979 (42), 2922 (100), 2871 (29), 2730 (8), 1615 (91), 1516 (40), 1452 (26), 1416 (6), 1372 (32), 1356 (52), 1310 (11), 1294 (28), 1213 (15), 1180 (18), 1143 (6), 1107 (8), 1059 (18), 853 (25), 788 (9), 760 (5), 719 (20), 644 (6), 626 (11), 595 (8); **IR (ATR, in cm⁻¹)**: v = 2976 (vw), 2925 (vw), 1615 (vw), 1585 (w), 1555 (w), 1513 (w), 1422 (w), 1371 (w), 1352 (w), 1309 (vw), 1296 (vw), 1175 (w), 1142 (vw), 1104 (w), 973 (s), 886 (w), 819 (w), 775 (w), 739 (vw), 716 (vw), 644 (vw), 625 (w), 591 (m), 548 (vw), 531 (vw), 510 (vw), 422 (vw); **¹H NMR (CD₂Cl₂, in ppm)**: δ = 0.01 (24H, s (br), H6a), 0.80 (24H, s (br), H6b), 2.13 (12H, s, H4), 2.46 (12H, s (br), H11), 3.52 (8H, s (br), H5), 6.89 (8H, d, ³J_{HH} = 5.4 Hz, H9), 8.40 (8H, s, H8); **¹³C{¹H} NMR (CD₂Cl₂, in ppm)**: δ = 15.1 (4C, s, C4), 20.9 (4C, s, C11), 22.8 (8C, s, C6a), 23.2 (8C, s, C6b), 70.5 (8C, s, C5), 84.7 (4C, d, ¹J_{CP} = 229.6 Hz, C2), 121.5 (8C, s, C8), 129.4 (8C, s, C9), 134.6 (4C, s, C10), 138.4 (4C, s, C7), 150.3 (4C, s, C3), 173.2 (4C, s (br), C1); **³¹P{¹H} NMR (CD₂Cl₂, in ppm)**: δ = 32.1 (s(br)); **³¹P{} NMR (CD₂Cl₂, in ppm)**: δ = 32.1 (s(br)); **Elemental analysis** for $C_{68}H_{97}CeN_8O_{16}P_4$ (Ce**L₃**H**L**), calculated: C 52.81, N 7.25, H 6.32; found: C 52.65, N 7.11, H 5.98; **ESI-MS (in m/z)**: 1194.6 [M-HL+H]⁺ (ESI⁺), 1544.6 [M-H]⁻ (ESI⁻).
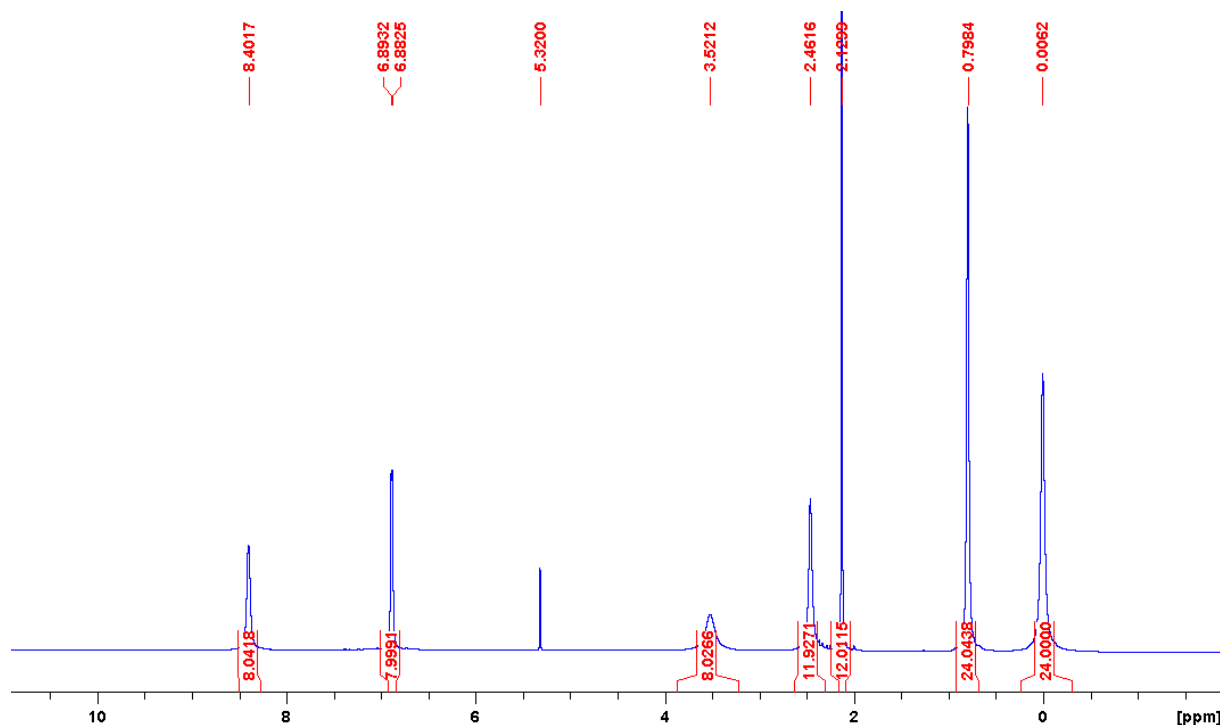
Fig. S7 ¹H NMR spectrum of **5** (CD₂Cl₂, 300 K).
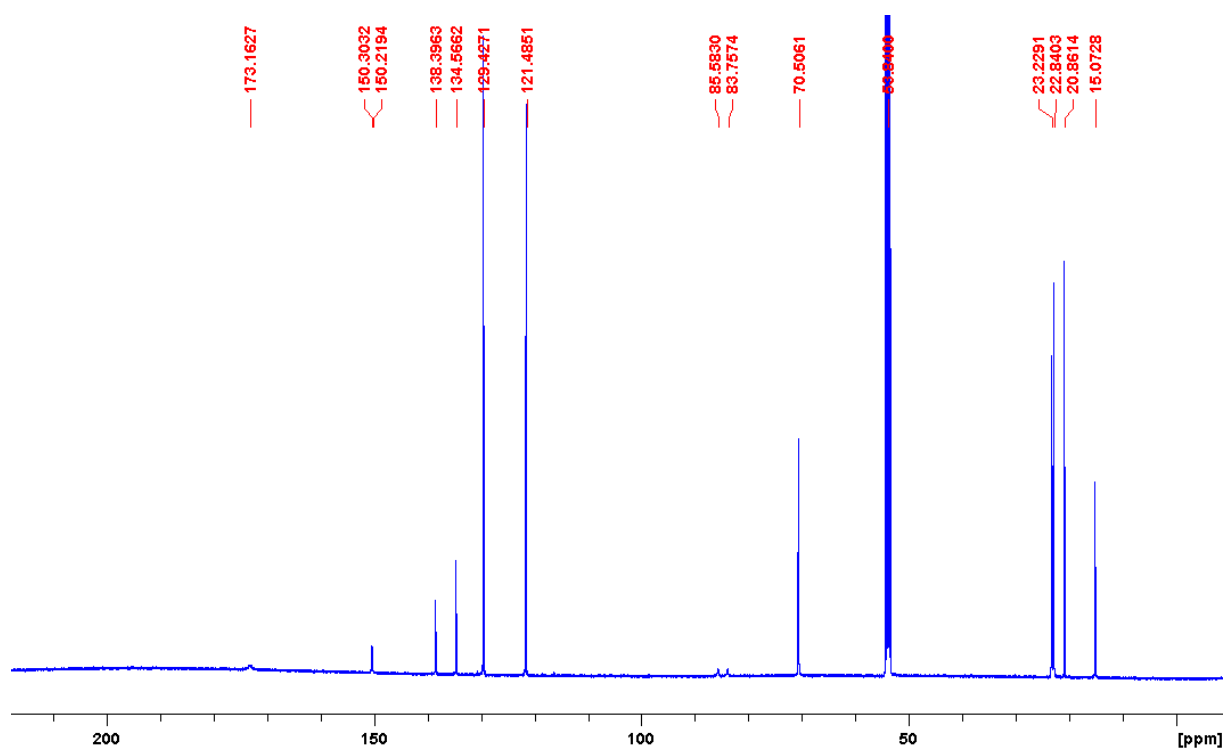
Fig. S8 ^{13}C{H} NMR spectrum of **5** (CD$_2$Cl$_2$, 300 K).
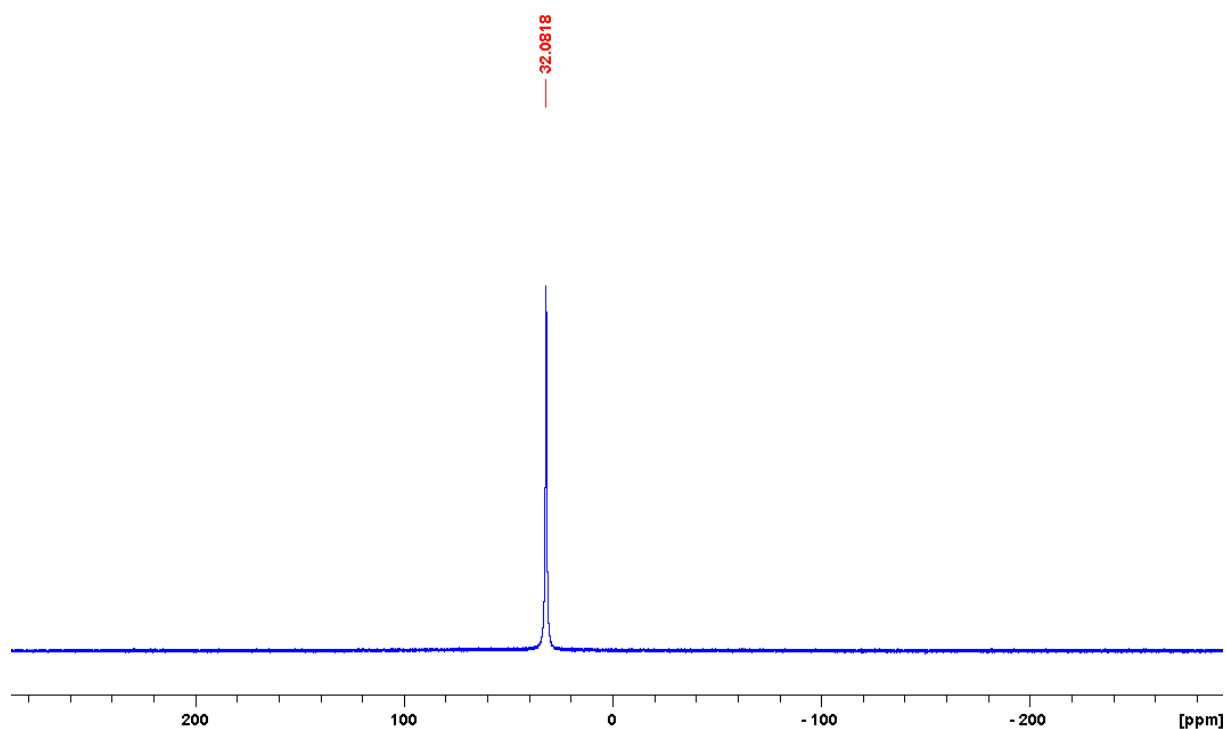
Fig. S9 ^{31}P NMR spectrum of **5** (CD$_2$Cl$_2$, 300 K).

Recrystallization in the glove box involved diethyl ether diffusion into a solution of the complex in acetonitrile to give suitable crystals for single crystal X-ray diffraction analysis as the acetonitrile and diethyl ether solvate of the composition [CeL$_3$HL]·CH$_3$CN·(C$_2$H$_5$)$_2$O (**5**·CH$_3$CN·(C$_2$H$_5$)$_2$O).

As depicted in **Fig. S9**, a single ^{31}P resonance of **5**·is observed at δ = 32.1 ppm, which is 8.9 ppm shifted to higher field compared to the single resonance observed for **4** at δ = 41.0 ppm (**Fig. S6**). The latter is the complex isolated from the reaction of Ce(III) with three equivalents of H**L**. Presumable the change in coordination number of the

metal centre results in the obtained shift of the ^{31}P resonance. In order to proof this hypothesis a solution of **4** was reacted with 1 eq. of H**L** and monitored by ^{31}P NMR spectroscopy. The obtained results are displayed in **Fig. S10** and **Fig. 7** showing that the change in the Ce(III) to ligand ration in the solution leads to shift of about 8 ppm of the resonance in the ^{31}P NMR spectra, presumable cause by the change in the coordination of the Ce(III) metal centre.
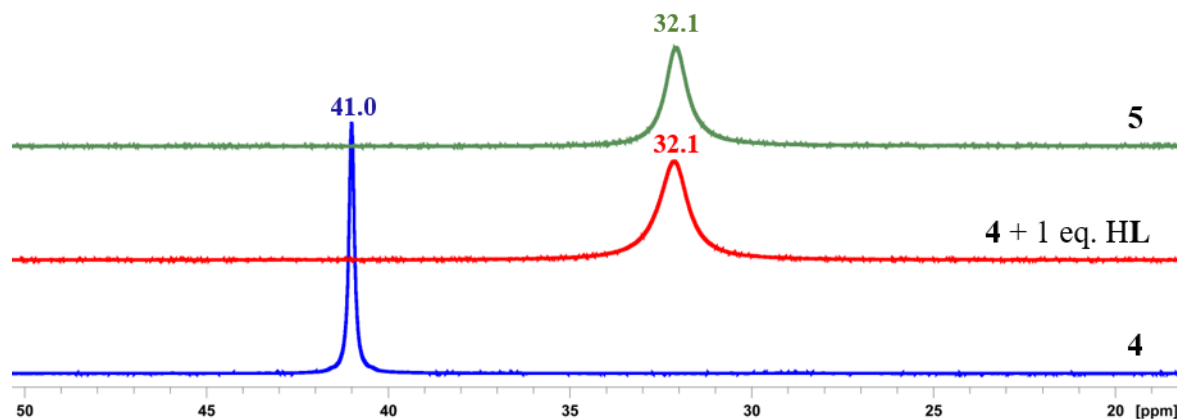
Fig. S10 Stack of the ^{31}P NMR spectra of **4**, the reacting of **4** with 1 eq. H**L** and **5** (CD$_2$Cl$_2$, 300 K).

Synthesis of the complexes of Ce(IV), Th(IV), U(IV), and Np(IV)

The synthesis of the 4*f* and 5*f* block metal(IV) complexes [M**L**$_4$] were performed in acetonitrile or methanol water mixtures with moderate yields. The ligand H**L** (4 eq.) was dissolved in acetonitrile or methanol and a 1 eq. water solution of the corresponding metal salt (Ce(SO$_4$)$_2$ ·4H$_2$O, Th(NO$_3$)$_4$·5H$_2$O, NpCl$_4$, and UCl$_4$, respectively) was added. For the synthesis of the Ce(IV) and U(IV) complex NaOH was added to promote the deprotonation of H**L**, suggesting that the *Lewis* acidity of Th(IV) and Np(IV) is strong enough to induce the deprotonation of the ligand without further addition of a base under the present conditions. Due to radiation safety not elemental analysis were conducted for the obtained Th(IV) and Np(IV) complex.

Synthesis of [CeL$_4$] (6)
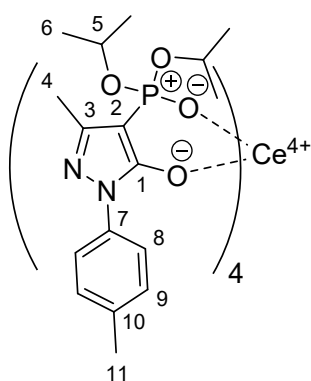
For the synthesis of the Ce(IV) complex 385.3 mg (1.0 mmol, 4 eq.) of H**L** (91%) were dissolved in 8 ml acetonitrile and 40.6 mg (1.0 mmol, 4 eq.) of NaOH (99%) were dissolved in 6 ml H$_2$O. Ce(SO$_4$)$_2$·4H$_2$O (99.8%, 102.3 mg, 0.25 mmol, 1 eq.) was suspended in 4 ml H$_2$O. After the addition of the NaOH solution to the solution of H**L** the Ce(SO$_4$)$_2$ suspension was added dropwise at 80 °C to the stirred solution. After some time a colour changed to dark violet on the surface of the residual Ce(SO$_4$)$_2$ particles hint to a start of the complex formation. The reaction mixture was stirred for another hour at 80 °C, cooled down to room temperature, put it in fridge for another 2h. The dark violet powder was collected after filtration. The obtained ^1H NMR and ^{31}P NMR are shown in **Fig. S11** and **Fig. S12**.

Chemical Science
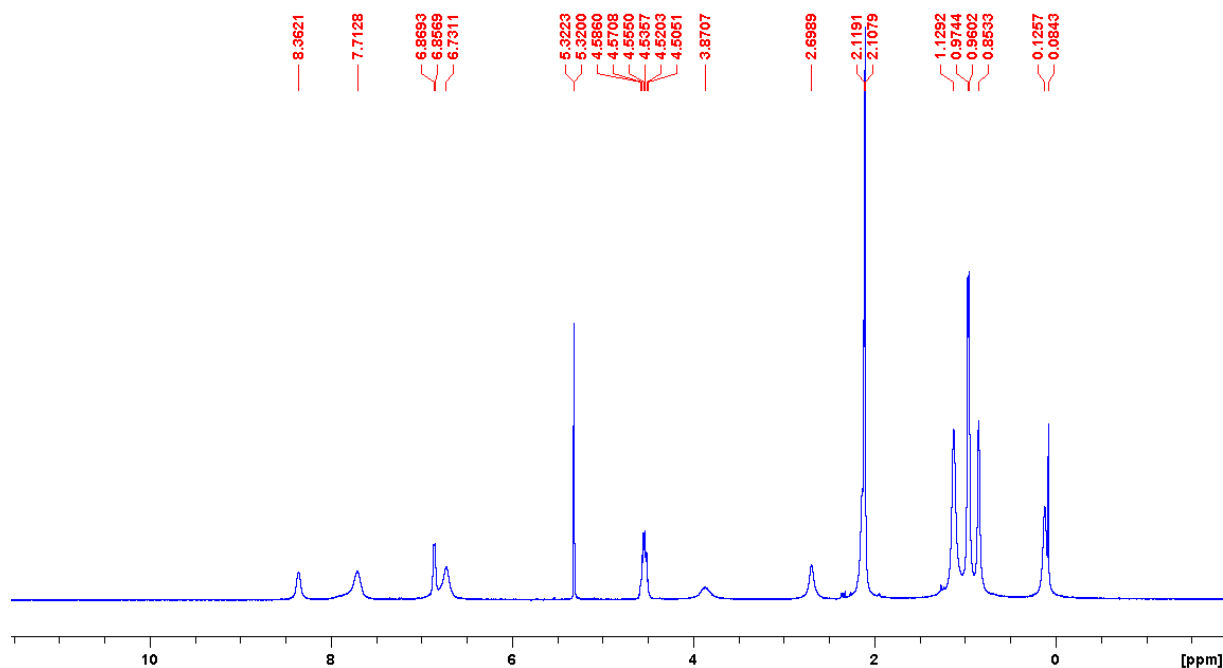
Fig. S11 ^{1}H NMR spectrum of Ce(IV) complex (CD$_2$Cl$_2$, 300 K).
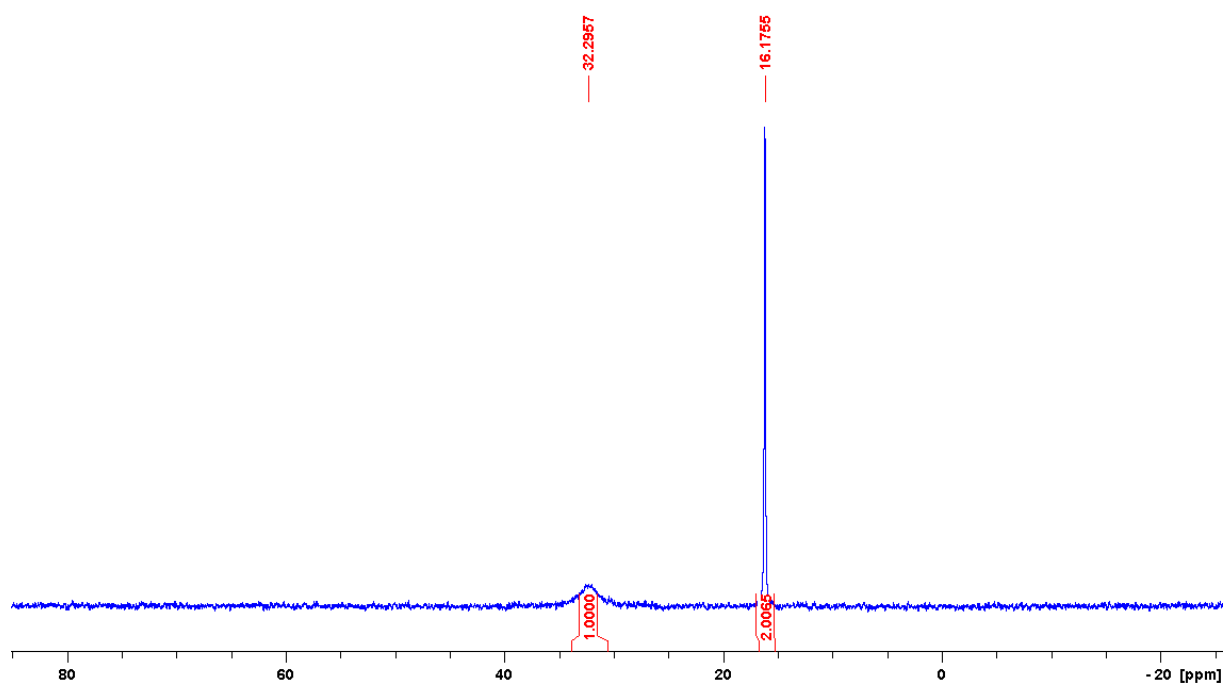
Fig. S12 ^{31}P NMR spectrum of Ce(IV) complex (CD$_2$Cl$_2$, 300 K).

From ^{1}H NMR and ^{31}P NMR spectra, we concluded that there are two species of the cerium complex in a 1:2 ratio present. From the analytical date of **5** the broad resonance at δ = 32.3 ppm may be assigned to the complex of Ce(III) with the metal centre coordinated by four ligands (^{31}P NMR of [CeL$_3$HL]: δ = 32.1 ppm, **Fig. S9**). Thus, the resonance at δ = 16.2 ppm can be assigned to the desired Ce(IV) complex. To further prove this assumption, 5 mM KMnO$_4$ solution was used as oxidant to wash the above NMR sample (1:1 ratio). The obtained ^{1}H, ^{31}P and ^{13}C{^{1}H} NMR spectra are shown in **Fig. S13** to **Fig. S15**.
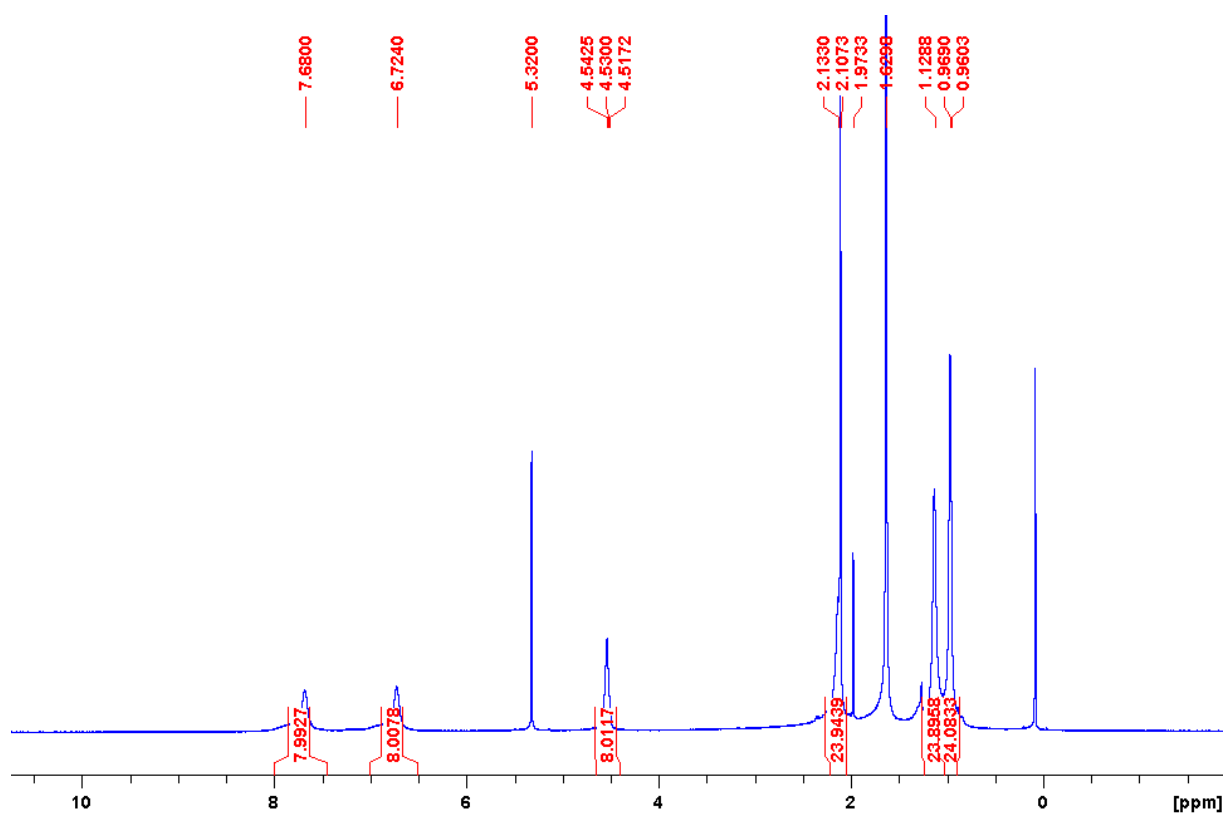
Fig. S13 ^{1}H NMR spectrum of Ce(IV) complex after washing with 5 mM KMnO$_4$ (CD$_2$Cl$_2$, 300 K).
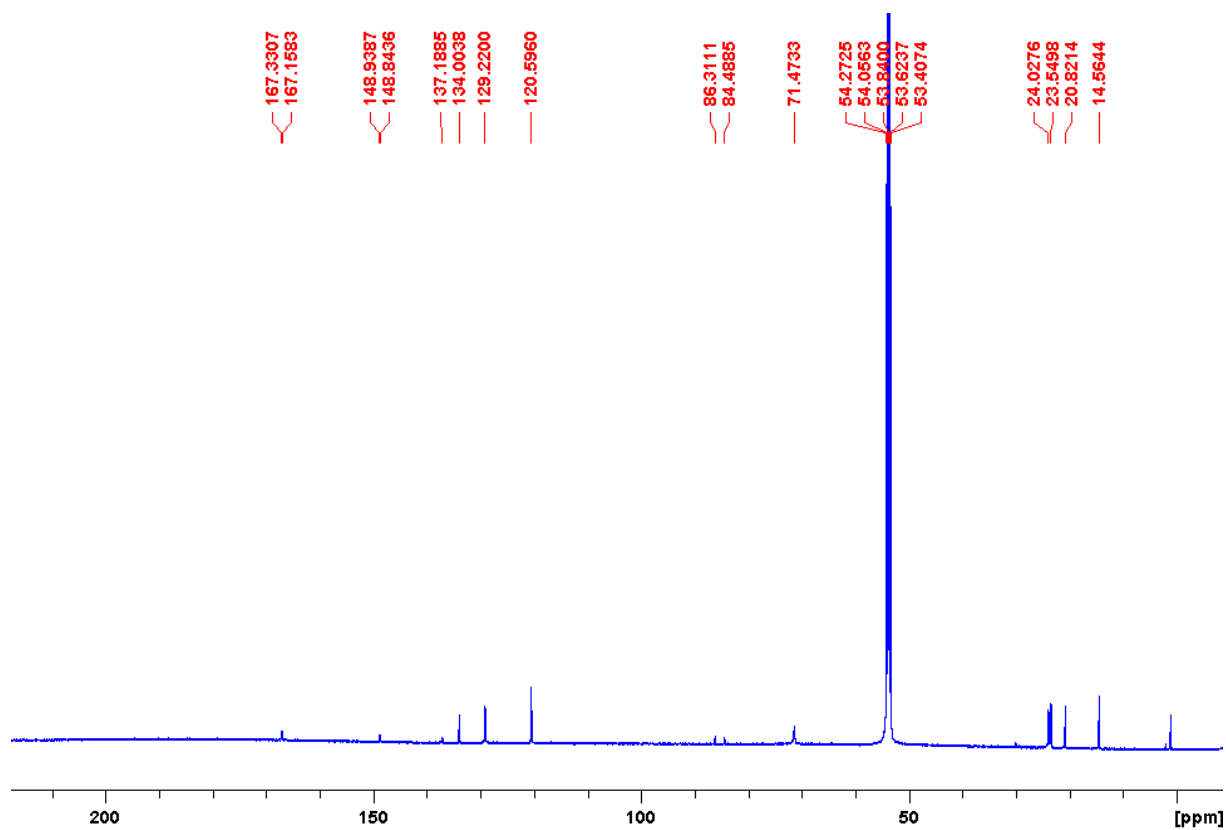
Fig. S14 ^{13}C{^{1}H} NMR spectrum of Ce(IV) complex after washing with 5 mM KMnO$_4$ (CD$_2$Cl$_2$, 300 K).
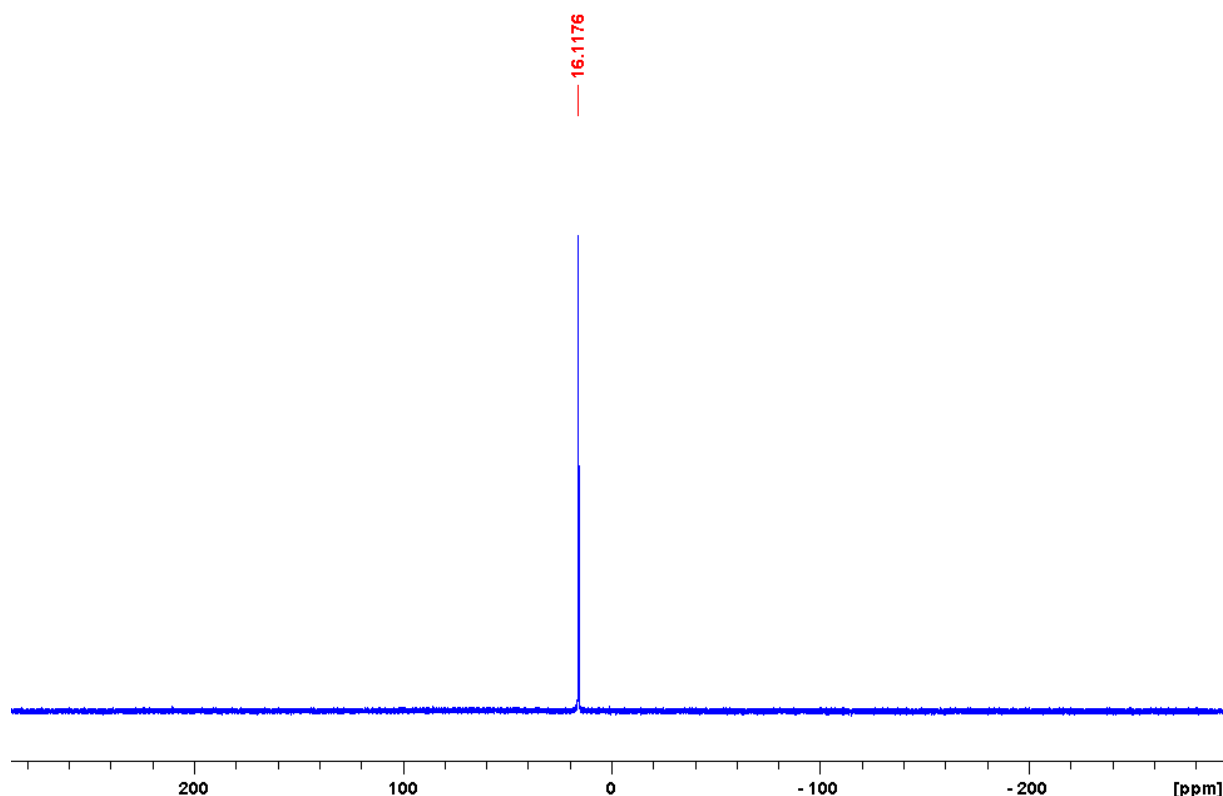
Fig. S15 ^{31}P NMR spectrum of Ce(IV) complex after washing with 5 mM KMnO$_4$ (CD$_2$Cl$_2$, 300 K).

As shown in **Fig. S15**, after oxidation, in the ^{31}P NMR only one resonance at $\delta = 16.1$ ppm is obtained, pointing at a complete oxidization to Ce(IV) species. Control experiments with pure H$_2$O were also performed. In the obtained ^{31}P NMR spectra after washing with H$_2$O no change was observed, pointing at the presence of both complexes.

Yield: 294.3 mg, 75%; **Raman (80 mW, in cm^{-1})**: ν = 3080 (22), 3064 (20), 3033 (24), 3010 (27), 2977 (44), 2923 (95), 2885 (52), 2871 (56), 2736 (28), 1649 (28), 1614 (78), 1587 (51), 1564 (100), 1516 (75), 1452 (51), 1357 (53), 1313 (33), 1294 (38), 1213 (29), 1180 (39), 1155 (30), 1141 (28), 1097 (31), 1060 (31), 891 (21), 854 (35), 790 (36), 760 (20), 717 (29), 640 (18), 626 (19), 598 (27), 434 (25), 426 (24), 412 (23), 405 (23), 362 (22), 227 (21), 220 (22), 77 (64); **IR (ATR, in cm^{-1})**: ν = 2976 (w), 2926 (w), 2870 (vw), 1645 (vw), 1614 (w), 1583 (m), 1558 (m), 1529 (m), 1512 (s), 1450 (w), 1423 (m), 1383 (m), 1373 (m), 1352 (m), 1308 (w), 1296 (w), 1221 (w), 1198 (w), 1178 (s), 1144 (m), 1101 (m), 1047 (w), 976 (vs), 887 (m), 845 (w), 820 (m), 777 (s), 739 (m), 717 (w), 685 (w), 642 (w), 627 (m), 592 (s), 577 (s), 569 (s), 548 (m), 530 (m), 509 (m), 453 (w), 422 (m); **^{1}H NMR (CD$_2$Cl$_2$, in ppm)**: δ = 0.97 (24H, d, $^3J_{HH}$ = 4.4 Hz, H6a), 1.13 (24H, s (br), H6b), 2.11 (12H, s, H4), 2.13 (12H, s (br), H11), 4.54 (8H, m, H5), 6.72 (8H, s (br), H9), 7.68 (8H, s (br), H8); **^{13}C{^{1}H} NMR (CD$_2$Cl$_2$, in ppm)**: δ = 14.6 (4C, s, C4), 20.8 (4C, s, C11), 23.5 (8C, d, $^3J_{CP}$ = 3.4 Hz, C6a), 24.0 (8C, s, C6b), 71.5 (8C, s, C5), 85.4 (4C, d, $^1J_{CP}$ = 229.2 Hz, C2), 120.6 (8C, s, C8), 129.2 (8C, s, C9), 134.0 (4C, s, C10), 137.2 (4C, s, C7), 148.9 (4C, d, $^2J_{CP}$ = 12.0 Hz, C3), 167.2 (4C, d, $^2J_{CP}$ = 21.7 Hz, C1); **^{31}P{^{1}H} NMR (CD$_2$Cl$_2$, in ppm)**: δ = 16.1 (s); **^{31}P{} NMR (CD$_2$Cl$_2$, in ppm)**: δ = 16.1 (t, $^3J_{PH}$ = 7.7 Hz); **Elemental analysis** for C$_{68}$H$_{98}$CeN$_8$O$_{17}$P$_4$ ([CeL$_4$]·H$_2$O), calculated: C 52.24, N 7.17, H 6.32; found: C 52.26, N 7.18, H 6.05; **ESI-MS (in m/z)**: 1194.54 [M–L]$^+$.

To obtain single crystals suitable for X-ray diffraction analysis the dark violet powder was dissolved in acetonitrile/H$_2$O mixture and 10 ml ethanol were added. After slow evaporation of all volatiles, square dark violet (almost black) crystalline plates grow on the walls of the vial of the composition [CeL$_4$]·2CH$_3$CN·4H$_2$O (**6**·2CH$_3$CN·4H$_2$O).

Synthesis of [ThL$_4$]·3CH$_3$CN·4H$_2$O (7·3CH$_3$CN·4H$_2$O)
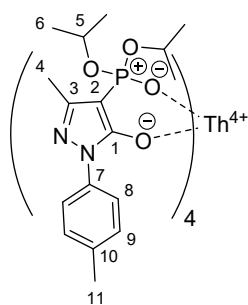
50.33 mg (0.133 mmol, 4 eq) of HL (91%) were dissolved in 3 ml acetonitrile. Then 19.17 mg (0.033 mmol, 1 eq) of (Th(NO$_3$)$_4$·5H$_2$O) dissolved in 1 mL of deionized water were added to the solution. At the interphase of the aqueous and the organic phase the immediate formation of colourless precipitate, which immediately re-dissolves, could be observed. The reaction was thoroughly mixed by a vortex apparatus and after some seconds a colourless precipitate formed. The precipitate was recrystallized by heating the reaction mixture at 50 °C for 2 h in a microwave and slowly cooling down stepwise from 40 °C to r.t. without stirring, yielding in 29.81 mg of the target compound **7**.

Yield: 29.81 mg, 55%, **Raman (80 mW, in cm^{-1})**: ν = 3078 (12), 3037 (10), 3016 (12), 2985 (31), 2937 (54), 2919 (62), 2740 (4),2734 (7), 1616 (90), 1591 (11), 1573 (8), 1519 (47), 1489 (7), 1450 (28), 1419 (13), 1381 (60), 1365 (50), 1317 (14), 1298 (47), 1213 (17), 1182 (11), 1145 (10), 1099 (8), 1062 (24), 893 (8), 858 (32), 790 (19), 736 (13), 719 (28), 706 (14), 650 (18), 626 (12), 424 (13), 397 (11), 366 (18), 320 (10), 260 (19), 229 (13), 212 (13), 168 (15), 77 (100); **IR (ATR, in cm^{-1})**: ν = 2980 (w), 2926 (vw), 2870 (vw), 1616 (vw), 1585 (w), 1535 (s), 1514 (s), 1423 (m), 1375 (m), 1311 (vw), 1298 (w), 1288 (w), 1178 (w), 1144 (s), 1092 (m), 1061 (w), 980 (vs), 889 (m), 854 (w), 822 (m), 773 (m), 760 (m), 731 (w), 714 (w), 704 (w), 648 (w), 640 (w), 627 (m), 598 (vs), 582 (s), 548 (w), 530 (m), 511 (m), 496 (w), 424 (m); **^{1}H NMR (CDCl$_3$, in ppm)**: δ = 0.94 (24H, d, $^3J_{HH}$ = 5.5 Hz, H6a), 1.09 (24H, s (br), H6b), , 2.16 (12H, s(br), H4), 2.21 (12H, s, H11), 4.49 (8H, d sept, $^3J_{HP}$ = 8.1 Hz,$^3J_{HH}$ = 6.3 Hz, H5), 6.92 (8H, s (br), H9), 7.89 (8H, s (br), H8); **^{13}C{^{1}H} NMR (CDCl$_3$, in ppm)**: δ = 14.4 (4C, s, C4), 20.9 (4C, s, C11), 23.3 (8C, s, C6a), 23.7 (8C, s, C6b), 71.8 (8C, s (br), C5), 81.6 (4C, d, $^1J_{CP}$ = 230.3 Hz, C2), 120.4 (8C, s, C8), 129.2 (8C, s, C9), 134.1 (4C, s, C10), 136.9 (4C, s, C7), 148.9 (4C, d, $^2J_{CP}$ = 12.9 Hz, C3), 166.5 (4C, d, $^2J_{CP}$ = 22.2 Hz, C1); **^{31}P{^{1}H} NMR (CDCl$_3$, in ppm)**: δ = 17.9 (s); **^{31}P{} NMR (CDCl$_3$, in ppm)**: δ = 17.9 (s(br)); **ESI-MS (in m/z)**: 1637.8 [M + H]$^+$.
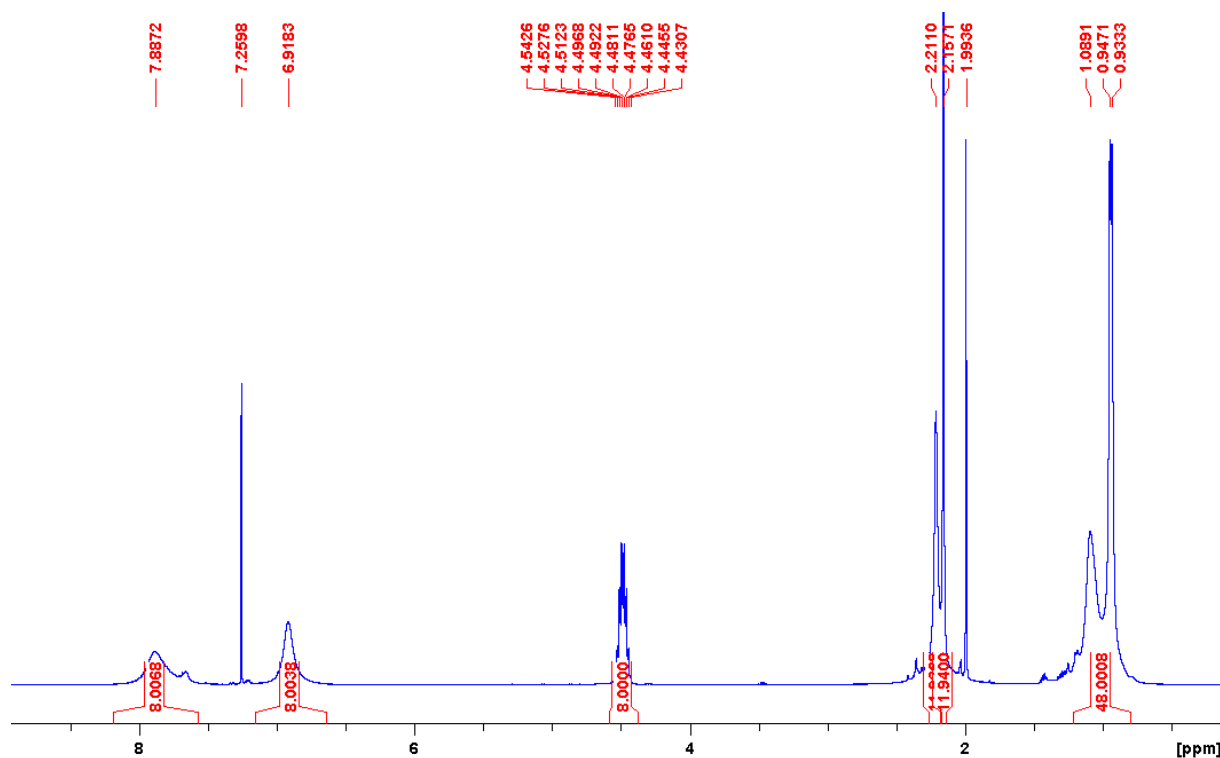
Fig. S16 ^{1}H NMR spectrum of Th(IV) complex (CDCl$_3$, 300 K).
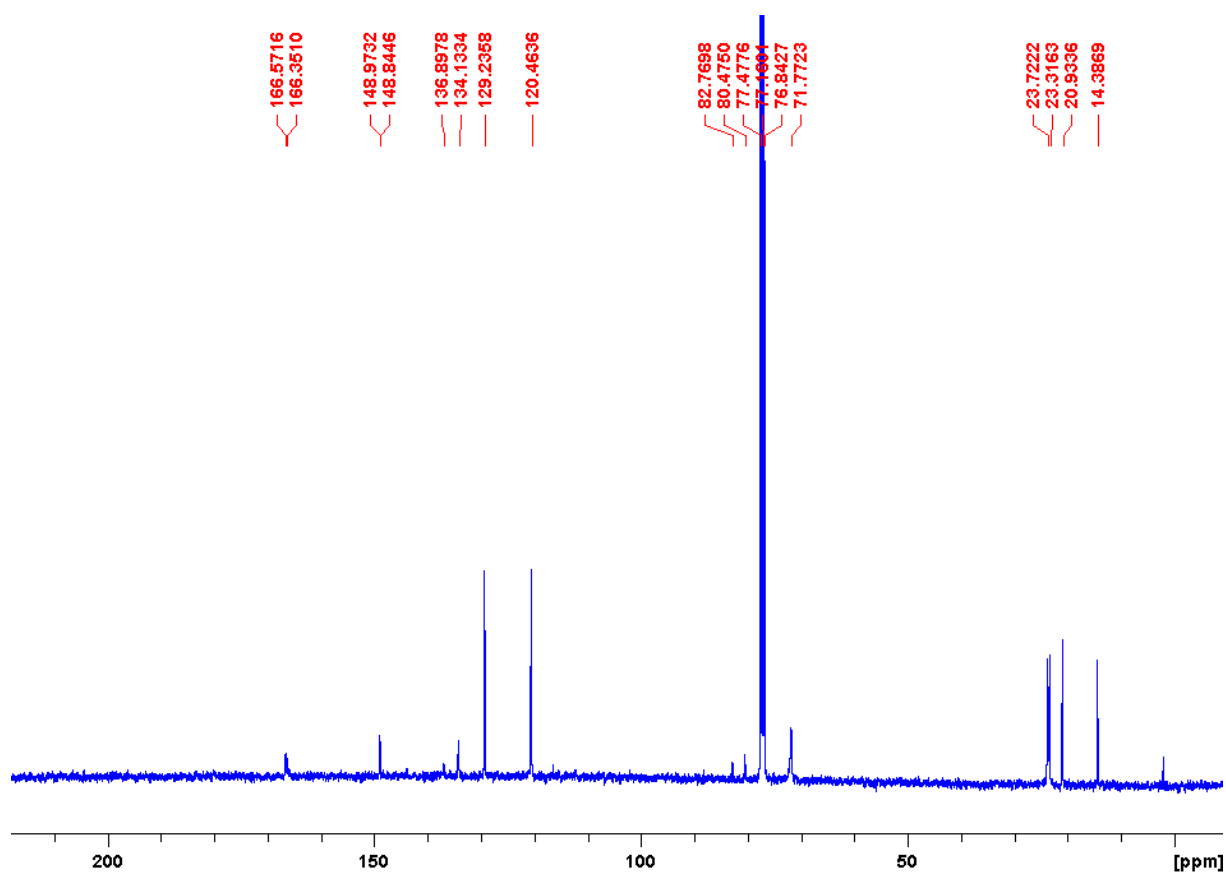
Fig. S17 ^{13}C{^{1}H} NMR spectrum of Th(IV) complex (CDCl$_3$, 300 K).
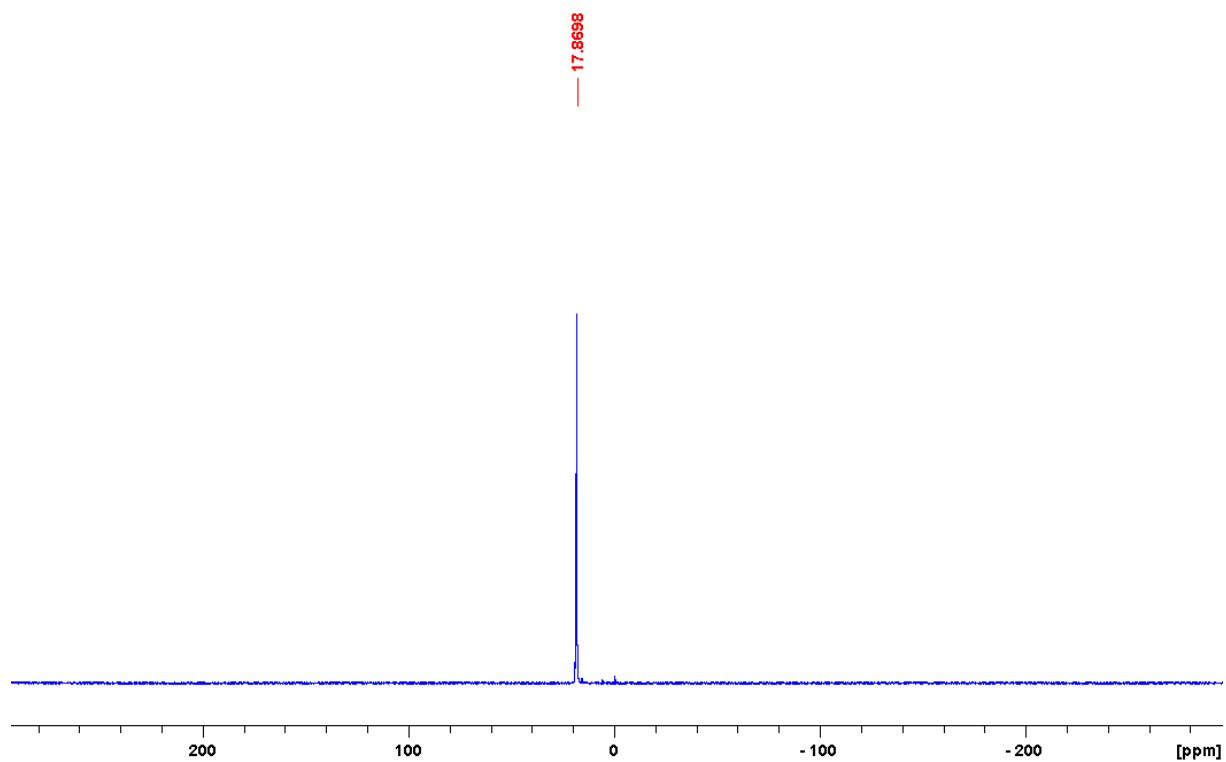
Fig. S18 ^{31}P NMR spectrum of Th(IV) complex (CDCl$_3$, 300 K).

Synthesis of [UL₄]
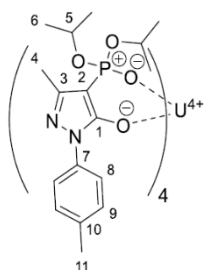
The manipulations were performed under N_2 atmosphere. The formed complex is stable in air. The ligand H**L** (48.6 mg, 0.130 mmol, 4 eq.) were dissolved in 2 mL CH_3OH and reacted with 1 eq. of UCl_4 (16.0 mg, 0.032 mmol) in H_2O in the presence of 4 eq. NaOH. The addition of water to the reaction mixture resulted in the precipitation of the formed complex. The obtained suspension was heated 80°C, stirred for 1 h, filtered and recrystallized upon cooling to room temperature to give 11.0 mg of **8**.

Yield: 11.0 mg, 21%, **IR (ATR, in cm⁻¹)**: v = 2978 (w), 2926 (w), 2872 (vw), 2869 (vw), 1615 (w), 1586 (w), 1532 (s), 1512 (vs), 1466 (m), 1444 (m), 1423 (m), 1374 (s), 1312 (w), 1299 (w), 1288 (w), 1275 (w), 1180 (m), 1142 (s), 1093 (s), 1061 (w), 977 (vs), 898 (m), 888 (s), 854 (w), 844 (w), 819 (s), 774 (s), 760 (s), 729 (m), 715 (m), 704 (m), 685 (m). **¹H NMR (CD₂Cl₂ in ppm)**: δ = -5.29 (s (br)), -3.88 (s (br)), -0.85 (s (br)), -0.26 (s (br)), 0.19 (s (br)), 0.57 (s (br)), 1.23 (s (br)), 1.34 (s (br)), 2.19 (s (br)), 2.34 (s (br)), 4.22 (s (br)), 4.54 (s (br)), 6.25 (s (br)), 6.97 (s (br)), 7.20 (s (br)), 7.60 (s (br)), 8.94 (s (br)), 11.08 (s (br)); **¹³C{¹H} NMR (CD₂Cl₂, in ppm)**: δ = 15.0 (s, (br)), 15.5 (s, (br)), 17.6 (t, (br)), 19.4 (s, (br)), 21.2 (s, (br)), 21.6 (m, (br)), 23.3 (s, (br)), 28.1 (s, (br)), 62.0 (s, (br)), 66.1 (s, (br)), 66.9 (s, (br)), 72.7 (s, (br)), 77.7 (s, (br)), 79.4 (s, (br)), 119.3 (s, (br)), 122.9 (s, (br)), 127.9 (s, (br)), 129.9 (s, (br)), 130.7 (s, (br)), 131.5 (s, (br)), 134.5 (s, (br)), 142.5 (s, (br)), 143.8 (s, (br)), 147.1 (s, (br)), 151.1 (s, (br)), 167.3 (s, (br)); **³¹P{¹H}19NMR (CD₂Cl₂ in ppm)**: δ = -40.5 (s (br)), -29.9 (s (br)). **Elemental analysis** for $C_{68}H_{96}N_8O_{16}P_4U$ ([U**L**₄]), calculated: C 49.70, N 6.82, H 5.89; found: C 49.34, N 6.83, H 5.91.
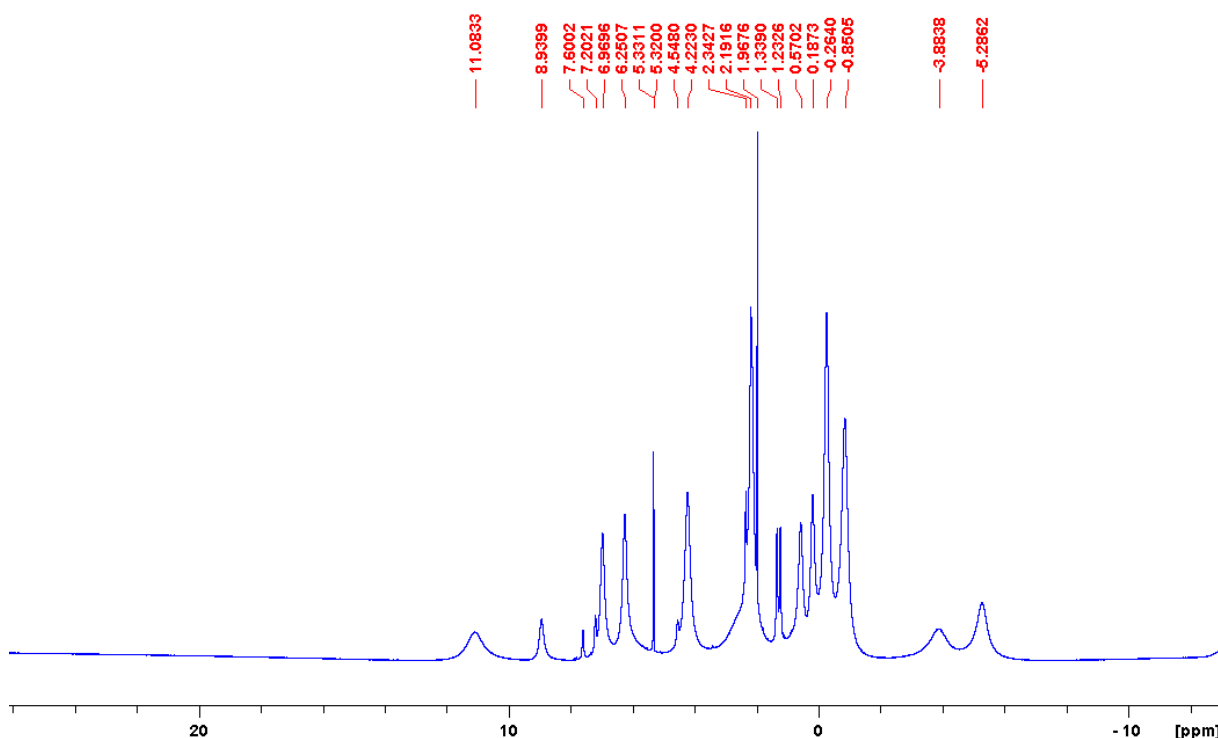
Fig. S19 ¹H NMR spectrum of U(IV) complex (CD₂Cl₂, 300 K).
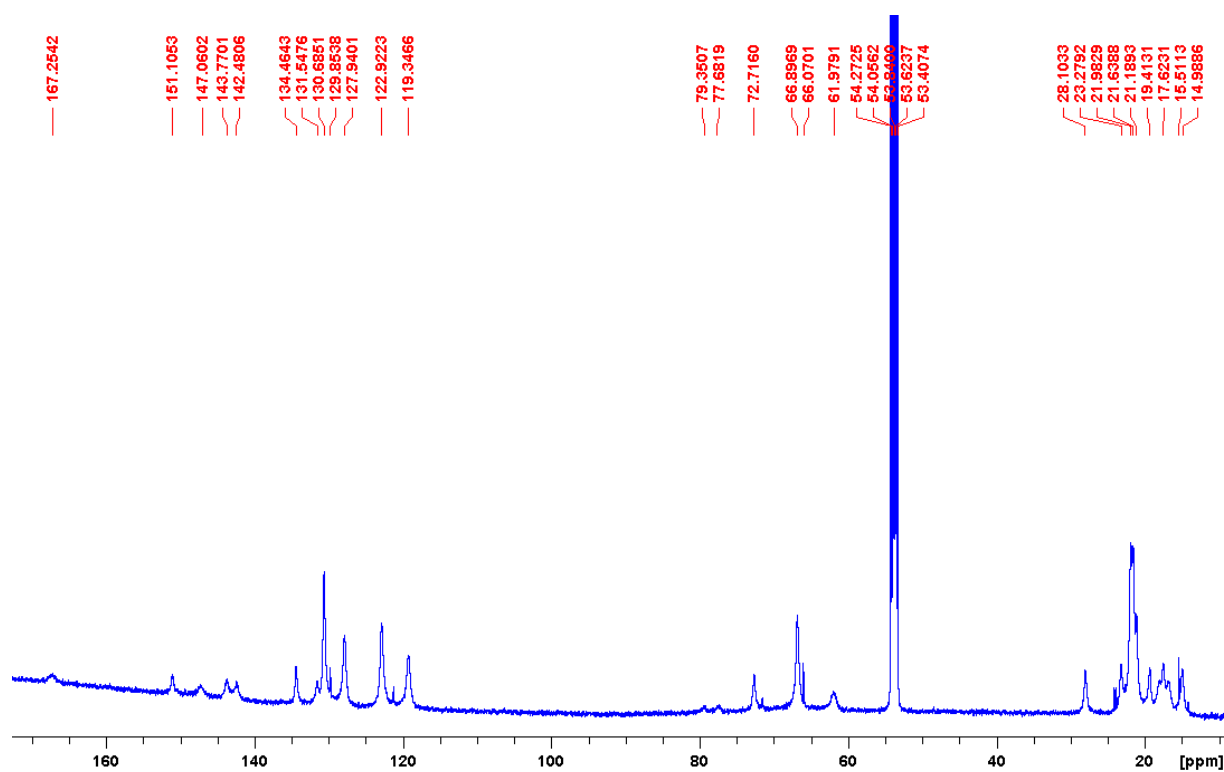
Fig. S20 $^{13}C\{^1H\}$ NMR spectrum of U(IV) complex (CD$_2$Cl$_2$, 300 K).
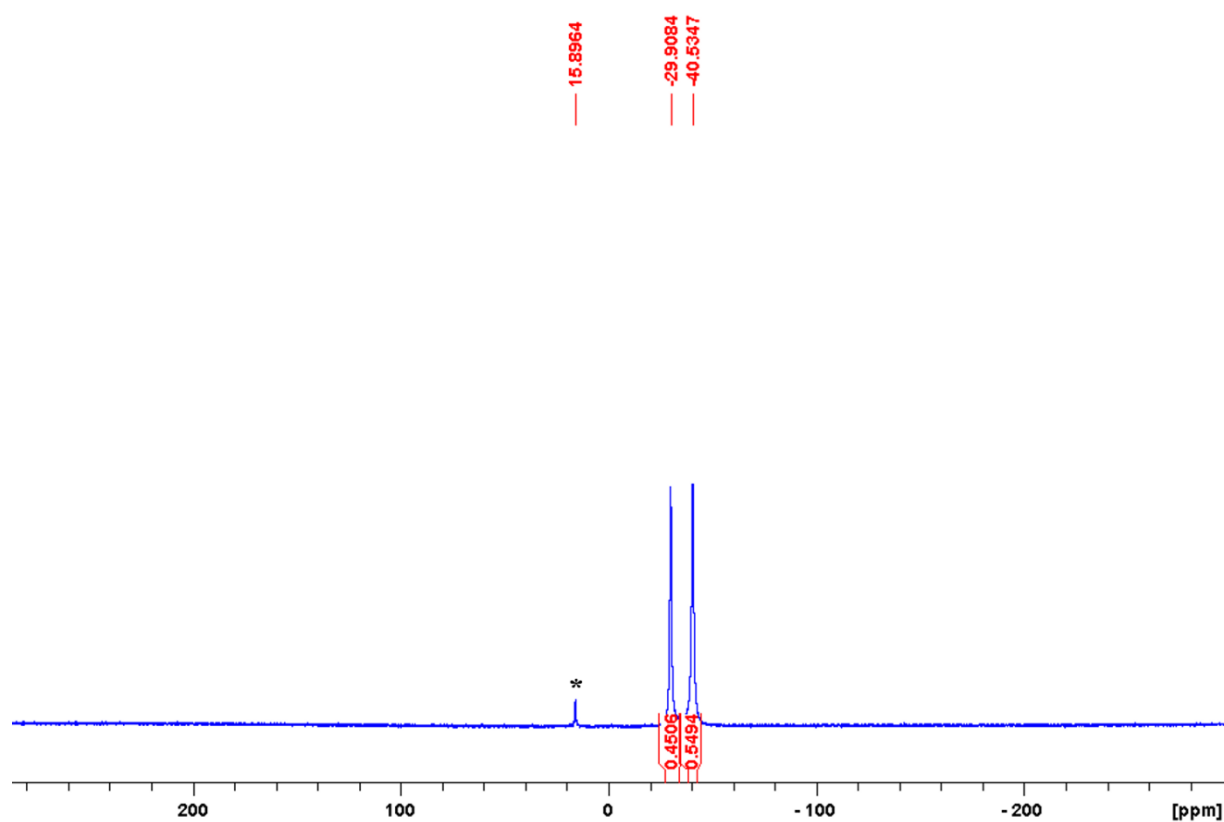
Fig. S21 ^{31}P NMR spectrum of U(IV) complex (CD$_2$Cl$_2$, 300 K, * free ligand).

Employing different solvents results in the insolation of single crystals suitable for X-ray diffraction with an altered placement of the ligands coordinating the U(IV) metal centre. If CH$_3$CN is used during the crystallisation the complex with the composition [UL$_4$]·3CH$_3$CN·4H$_2$O (**8**·3CH$_3$CN·4H$_2$O) is obtained. From CH$_2$Cl$_2$ in the absence

of CH_3CN [UL_4]·CH_2Cl_2 (**8**·CH_2Cl_2) and from toluene [UL_4] (**8**) were obtained. In all cases has the metal centre a coordination number of eight formed by the coordination of the two O-donor atoms of four deprotonated ligands. Whereas **8**·$3CH_3CN$·$4H_2O$ exhibits a strictly square-antiprismatic coordination environment due to the tetragonal space group *P*4/*n*, the structures **8**·CH_2Cl_2 and **8** are distorted towards a bicapped trigonal geometry (**Fig. 5**). The coordination polyhedron is best determined by measuring the angles δ and φ according to Porai-Koshits and Aslanov,[5] indicating a square-antiprismatic arrangement for **8**·CH_2Cl_2 but a bicapped trigonal geometry for **8**. Furthermore, a different arrangement of the ligands is observable for all three isomers. **8**·$3CH_3CN$·$4H_2O$ adopts the *llll*-configuration with all ligands linking the two square faces of the polyhedron and thereby pointing all in the same direction. In contrast the ligands in solvent-free **8** occupy two edges each of quadrangle closest to square shape, which is described as *ssss*-configuration. In the bicapped trigonal geometry this configuration is described as $t_1t_1p_2p_2$. Potential pathways for interconversion between the three isomers are shown in **Fig. S22**.
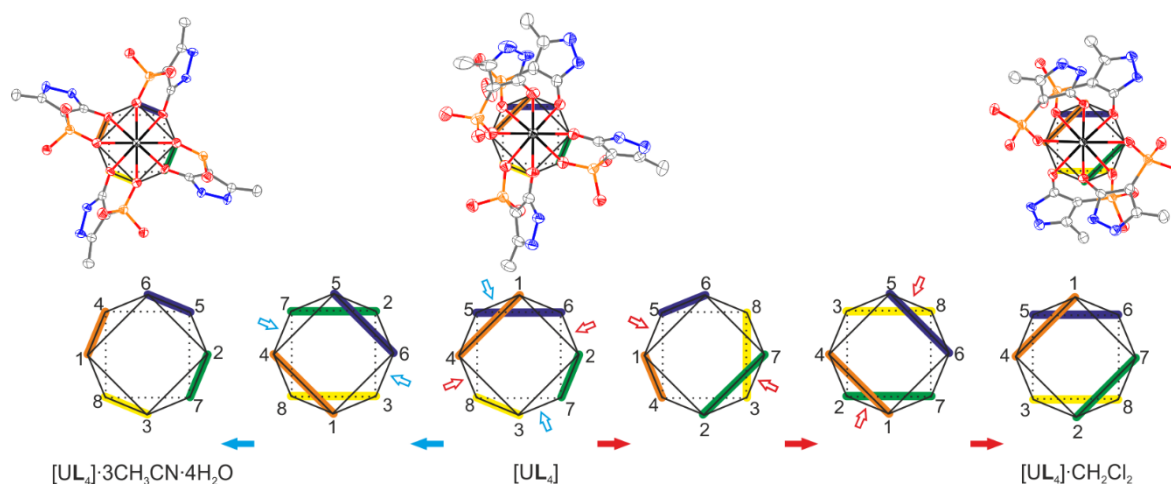
Fig. S22 Potential pathways for interconversion between the three isomers [UL_4]·$3CH_3CN$·$4H_2O$ (**8**·$3CH_3CN$·$4H_2O$), [UL_4]·CH_2Cl_2 (**8**·CH_2Cl_2) and [UL_4] (**8**).

Extended ^{31}P NMR studies of the U(IV) complex **8** were performed motivated by the presence of two broad resonances at δ = -40.5 ppm (s (br)) and δ = -29.9 ppm (s (br)) (**Fig. 6**).

Variable temperature ^{31}P NMR in CD_2Cl_2 were performed between 300 K and 190 K. The obtained spectra at 300 K, 280 K, 260 K, 240 K, 220 K, 200 K and 190 K are displayed in **Fig. S23** and reveal a broadening of the two resonances upon cooling. At 240 K an extremely broad signal appears, whereas at 220 K, 200 K and 190 K more complex spectra are observable. The two major resonances shift upon cooling to 190 K to δ = -2.3 ppm (s (br)) and δ = -46.1 ppm (s (br)). Presumable, the more complex spectra is a result of a reduced movement of the *iso*-propyl groups of the ligand at low temperature and hence a series of resonances can be observed. In contrast, the resonance attributed to the free ligand at δ = -15.9 ppm (s (br) does not shift with the temperature variation.
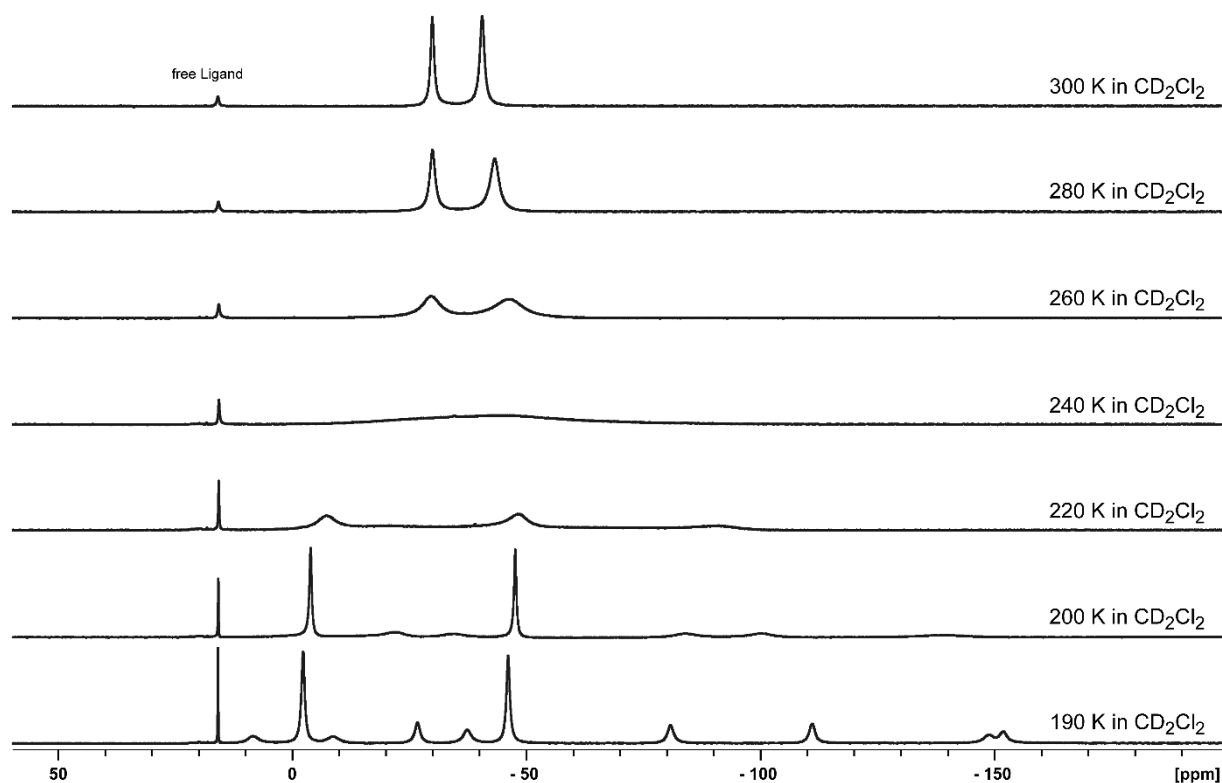
Fig. S23 ^{31}P NMR spectra of U(IV) complex at variable temperatures in CD_2Cl_2.

In order to investigate potential interaction between the present species ^{31}P-^{31}P- exchange spectroscopy (EXSY) experiment were performed at 300 K (**Fig. 8**) and 190 K (**Fig. S24**). In both a mixing time of 0.025 seconds was employed. The presence of exchange peaks between the two resonances at δ = -40.5 ppm and -29.9 ppm at 300 K indicates a dynamic exchange between the present species. Also at 190 K multiple exchange peaks are obtained showing an exchange of the different species. In contrast, no exchange peaks are observed involving the free ligand, pointing at an exchange between the complex species only.
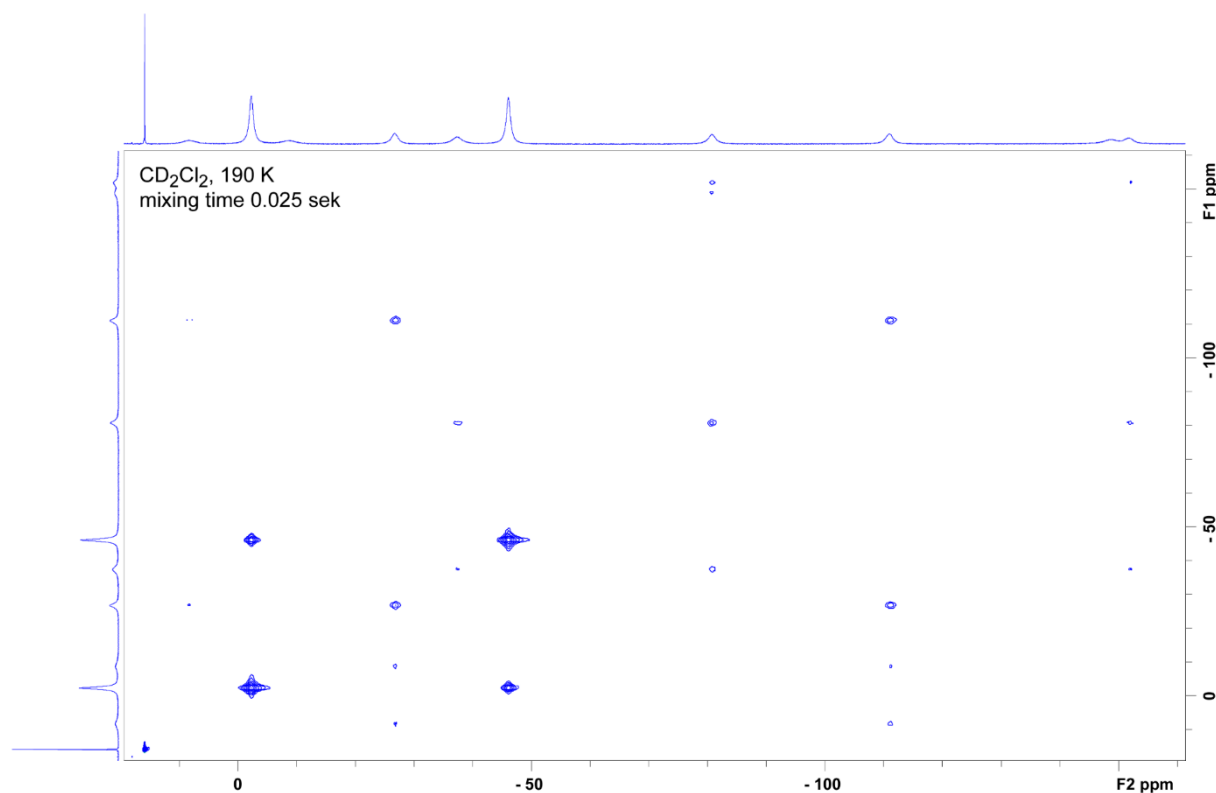
Fig. S24 ^{31}P-^{31}P- EXSY NMR spectrum of a solution of the U(IV) complex at 190 K in CD$_2$Cl$_2$ with a mixing time of 0.025 seconds.

In a second set of experiments toluene-d_8 was used as solvent and the ^{31}P NMR spectra of the U(IV) complex were recorded between 190 K and 360 K in increments of 10 K (**Fig. S25** – **Fig. S27**). In addition, the spectra were recorded in the presence of various amounts of CD$_3$CN at 300 K. As shown in **Fig. S28** the ratio between normalised integrals of the two resonance as δ = -28.2 ppm and δ = -38.9 ppm change from 0.68 to 0.32 in the absence of CD$_3$CN to 0.47 to 0.53 in the presence of an excess of CD$_3$CN. In ^{31}P NMR experiments using hexafluorobenzene a comparable change of the integral ratios for the two resonances at δ = -23 ppm and δ = -43 ppm is observable (**Fig. S29**). In the absence of CD$_3$CN the ratio is approximately 0.70 to 0.30 upon consideration of the very broad resonance at 23 ppm, whereas in the presence of an excess of CD$_3$CN a ratio of 0.38 to 0.62 is obtained.
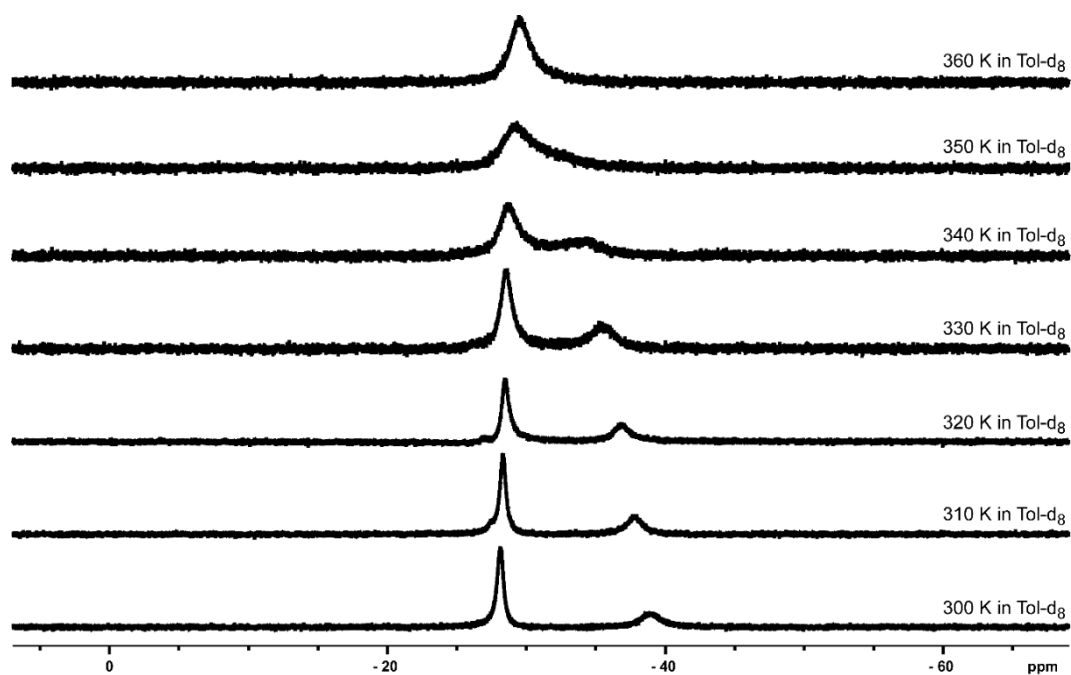
Fig. S25 ^{31}P NMR spectra of U(IV) complex in dependence of the temperature in toluol-d_8 between 360 and 300 K.
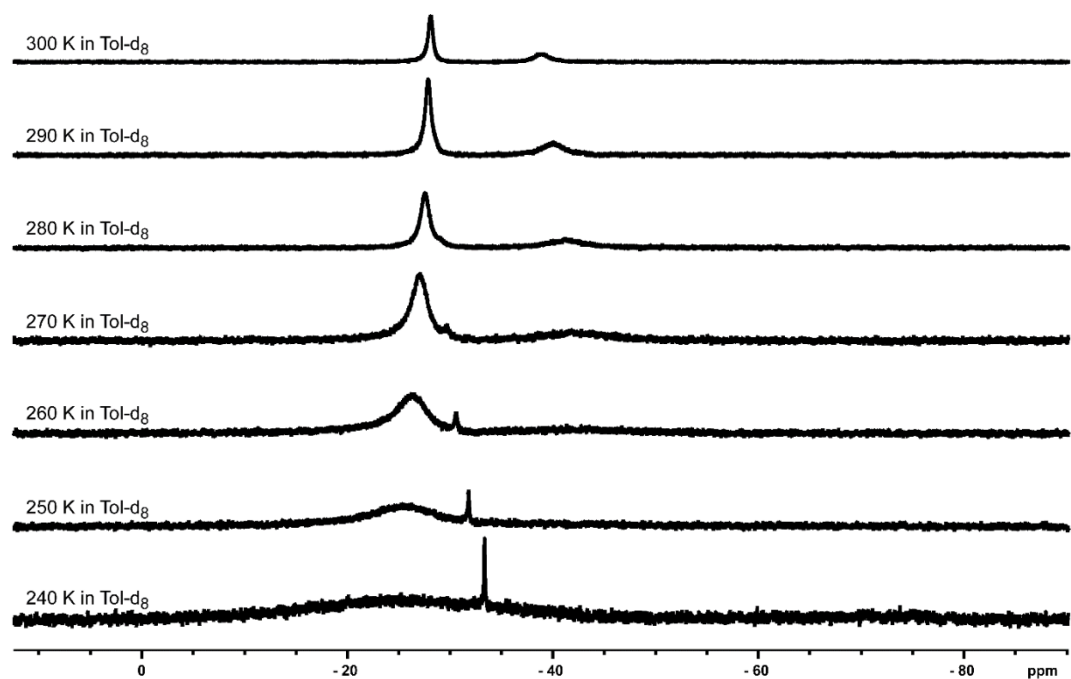
Fig. S26 ^{31}P NMR spectra of U(IV) complex in dependence of the temperature in toluol-d_8 between 300 and 240 K.
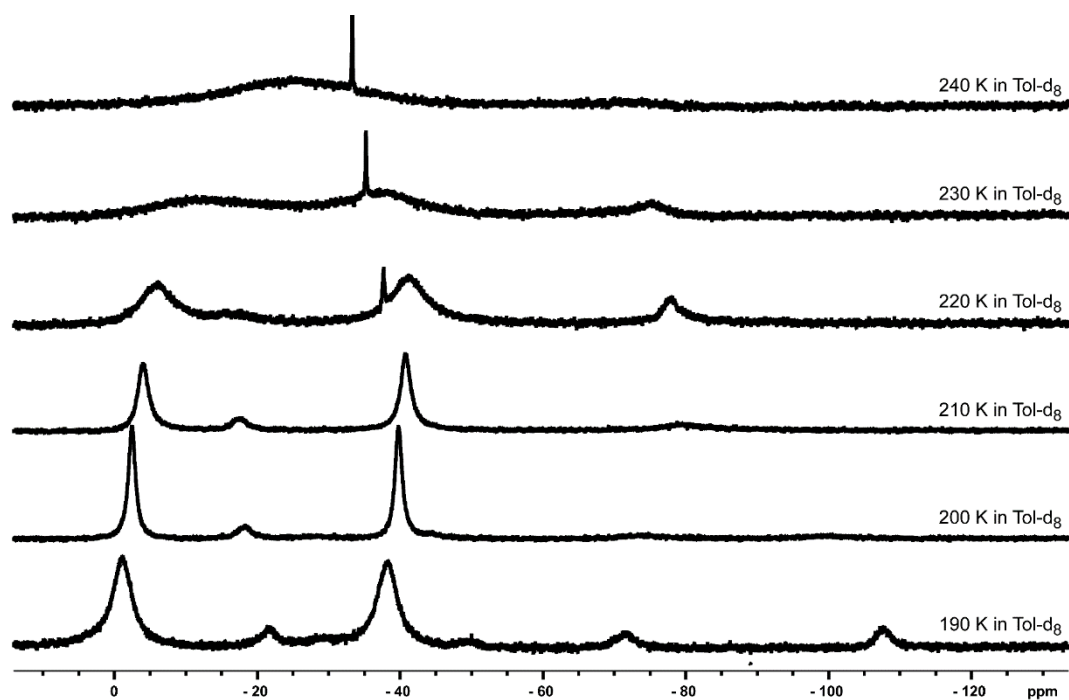
Fig. S27 ^{31}P NMR spectra of U(IV) complex in dependence of the temperature in toluol-d_8 between 240 and 190 K.
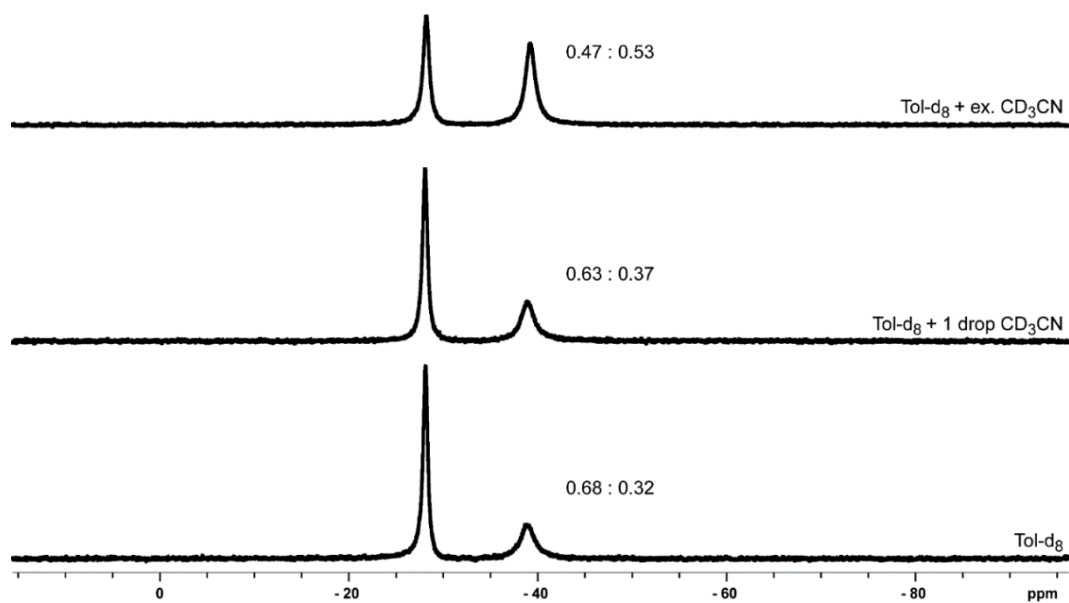
Fig. S28 ^{31}P NMR spectra of U(IV) complex at 300 K in toluene-d_8 with increasing amount of CD$_3$CN with the normalised integral to 1.0 of the resonances at -28.2 and -38.9 ppm..
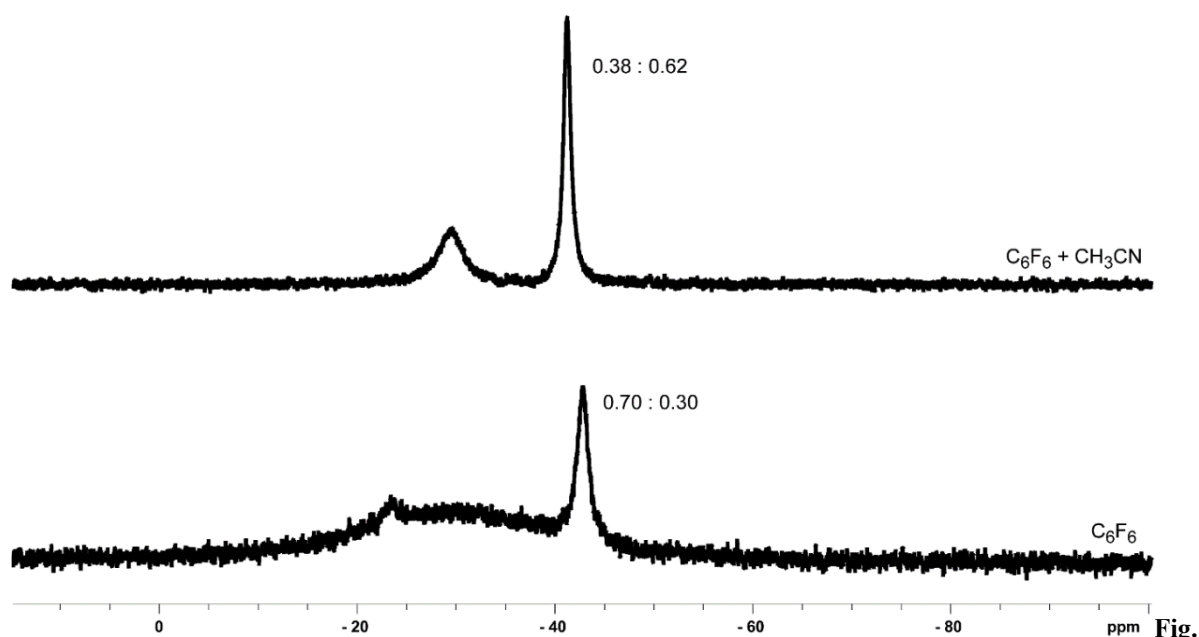
Fig. S29 ^{31}P NMR spectra of U(IV) complex at 300 K in hexafluorobenzene in the absence and presence of CD$_3$CN with the normalised integral to 1.0 of the resonances at δ = -23 ppm and δ = -43 ppm.

Synthesis of [NpL$_4$]·3CH$_3$CN·4H$_2$O (9·3CH$_3$CN·4H$_2$O)

Caution! Neptunium (^{237}Np) consists of radioactive nuclides including long-lived α-emitters (^{237}Np; $T_{1/2}$ = 2.14 × 10^6 years). Special precautions as well as appropriate equipment and facilities for radiation protection are required for handling this material. All experiments were carried out in a controlled laboratory at the Institute of Resource Ecology, Helmholtz-Zentrum Dresden - Rossendorf.
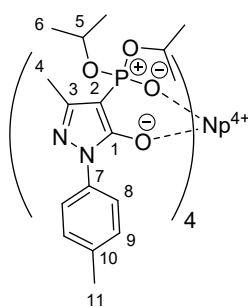
The complex [NpL$_4$]·3CH$_3$CN·4H$_2$O (9·3CH$_3$CN·4H$_2$O) was prepared by the reaction of 4 eq. of H**L** (91%; 48.3 mg, 0.130 mmol), dissolved in 3 mL of acetonitrile with 1 eq. of NpCl$_4$ (12.5 mg, 0.032 mmol) dissolved in 1 mL deionized water (turquoise coloured solution) at room temperature. An immediate colour change and the formation of a microcrystalline precipitate indicate the starting complex formation. After filtration of the microcrystalline precipitate the residual liquor was collected and left without stirring. Overnight green yellowish coloured crystals of **9**, suitable for X-ray single crystal analysis were grown from the mother liquor. After removing the crystals from their mother liquor they rapidly lose solvent molecules, resulting in a pale non-crystalline solid.

Yield: 17 mg, 30%, **IR (ATR, in cm^{-1})**: v = 2978 (w), 2951 (vw), 2926 (vw), 2887 (vw), 2882 (vw), 2875 (vw), 2870 (vw), 2866 (vw), 1726 (vw), 1724 (vw), 1615 (w), 1586 (w), 1534 (s), 1513 (s), 1465 (w), 1422 (m), 1383 (m), 1374 (m), 1313 (w), 1300 (w), 1288 (w), 1179 (w), 1144 (s), 1138 (s), 1092 (s), 1060 (w), 1045 (m), 983 (vs), 936 (m), 897 (m), 889 (m), 855 (w), 834 (w), 821 (s), 789 (m), 772 (s), 758 (m), 727 (m), 716 (m), 704 (m); **^{13}C{^{1}H} NMR (CDCl$_3$, in ppm)**: δ = 15.2 (s), 21.1 (s), 21.8 (s), 24.1 (s), 70.0 (s), 121.3, 129.5 (s), 129.9 (s), 134.4 (s), 142.3 (s (br)), 143.8 (s (br)); **^{31}P{} NMR (CDCl$_3$ in ppm)**: δ = -53.4 (s (br)).
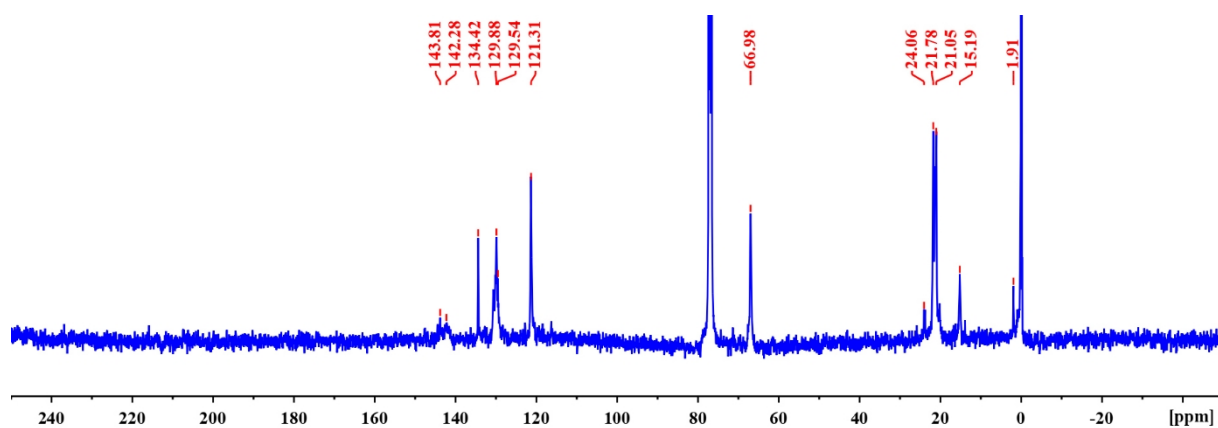
Fig. S30 $^{13}C\{^1H\}$ NMR spectrum of Np(IV) complex **9** in CDCl$_3$ (300 K).
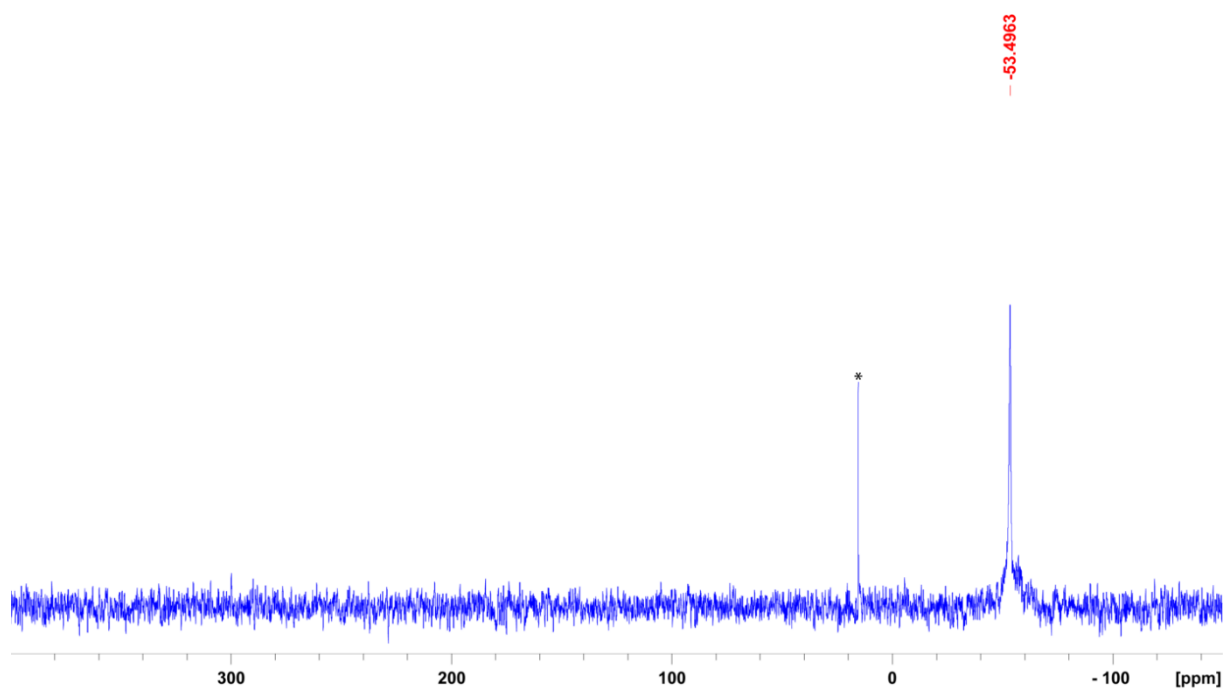
Fig. S31 ^{31}P NMR spectrum of Np(IV) complex **9** in CDCl$_3$ (300 K, * free ligand).

X-ray crystal structure analyses

Suitable single crystals were coated with Paratone-N oil or Fomblin Y25 PFPE oil and mounted using either a glass fiber or a nylon loop. In the diffractometer the mounted single crystals were exposed to a cold nitrogen stream. Crystal and data collection details are given in Table S1-S3. The single crystals analysis of [NpL$_4$]·3CH$_3$CN·4H$_2$O (**9**·3CH$_3$CN·4H$_2$O) was performed at the Helmholz-Zentrum-Dresden-Rossendorf (HZDR) on a Bruker D8 VENTURE diffractometer with a PHOTON 100 CMOS detector at 100 K and microfocus Mo Kα radiation (λ = 0.71073 Å). Suitable single crystals were selected under a polarizing optical microscope and mounted on a Micro-LoopTM (MiTiGen, USA) with mineral oil. The remaining X-ray diffraction data was collected on a Rigaku Oxford Diffraction SuperNova diffractometer using Cu Kα radiation (λ = 1.54184 Å) generated by a Nova micro-focus source. For **9**·3CH$_3$CN·4H$_2$O the data reduction was accomplished performed using SAINT (Version 8.37A).[6] The data correction for absorption effects was performed by using the Numerical Mu Calculated method (SADABS-2016/2).[7] The development of the structure was achieved by successive difference Fourier syntheses and the refinement was obtained by full-matrix least-squares on all F^2 data using SHELXL program suite (Version 2014-7)[8] and ShelXle.[9] Data reduction and absorption correction of the residual compounds was accomplished either with CrysAlisPro[10] software or Bruker SMART[11] or Bruker SADABS[12]. Employing Olex2[13], the structures were solved with SHELXT[14] and refined with SHELXL[8] by least-square minimization against F^2 using first isotropic and later anisotropic thermal parameters for all non-hydrogen atoms. Hydrogen atoms bonded to carbon atoms were added to the structure models on calculated positions using the riding model. All other hydrogen atoms were localized in the difference Fourier map. If necessary, disorders of solvent molecules were treated with appropriate restraints (SADI, SIMU, DELU, ISOR, DFIX, SUMP, SAME, FLAT, EADP, EXYZ, DFIX). Images of the structures were created with Olex2[13] software. All structures have been deposited with the Cambridge Crystallographic Data Centre (CCDC) and can be accessed free of charge under the numbers 1995660-1995663, 1997488 and 2020834-2020837.

Table S1 Crystallographic Data of [LaL₃HL]·3CH₃CN·4H₂O (**3**·3CH₃CN·4H₂O) and [CeL₃CH₃CN] (CH₃CN⊂**4**).

	3·3CH₃CN·4H₂O	CH₃CN⊂**4**
formula	$C_{74}H_{114}LaN_{11}O_{20}P_4$	$C_{53}H_{75}CeN_7O_{12}P_3$
M_r in g mol^{-1}	1740.55	1235.23
colour, habit	light yellow, block	clear colourless, block
crystal system	tetragonal	triclinic
space group	*P*4/*n*	*P*-1
a in Å	17.80376(5)	11.6391(3)
b in Å	17.80376(5)	13.3055(3)
c in Å	13.75097(7)	20.5728(3)
α in °	90	91.504(2)
β in °	90	90.766(2)
γ in °	90	111.160(2)
V in Å^3	4358.70(3)	2969.24(12)
Z	2	2
T in K	100.0(3)	100.0
crystal size in mm^3	0.257 × 0.154 × 0.104	0.143 × 0.105 × 0.033
ρ_c in g cm^{-3}	1.326	1.382
F(000)	1824.0	1282.0
diffractometer	OD SuperNova	OD SuperNova
$\lambda_{XK\alpha}$ in Å	X = Cu 1.54184	X = Cu 1.54184
θ_{min} in °	6.428	7.128
θ_{max} in °	153.386	77.206
index range	−22 ≤ h ≤ 20 −22 ≤ k ≤ 15 −16 ≤ l ≤ 17	−14 ≤ h ≤ 14 −16 ≤ k ≤ 16 −22 ≤ l ≤ 25
μ in mm^{-1}	5.072	7.208
abs. correction	gaussian	gaussian
reflections collected	48464	69638
reflections unique	4588	12352
R_{int}	0.0249	0.0565
reflections obs. [F>2σ(F)]	4556	11755
residual density in e Å^{-3}	0.31 / –0.64	1.58/−1.73
parameters	320	704
GOOF	1.051	1.071
R_1 [I>2σ(I)]	0.0227	0.0377
wR_2 (all data)	0.0631	0.1009
CCDC	1995661	2020835

Table S2 Crystallographic Data of [CeL$_3$HL]·CH$_3$CN·Et$_2$O (**5**·CH$_3$CN·Et$_2$O) and [CeL$_4$]·2CH$_3$CN·4H$_2$O (**6**·2CH$_3$CN·4H$_2$O).

	5·CH$_3$CN·Et$_2$O	**6**·2CH$_3$CN·4H$_2$O
formula	C$_{74}$H$_{110}$CeN$_9$O$_{17}$P$_4$	C$_{72}$H$_{110}$CeN$_{10}$O$_{20}$P$_4$
M$_r$ in g mol^{-1}	1661.70	1699.69
colour, habit	clear colourless, block	dark violet, plate
crystal system	monoclininc	tetragonal
space group	$P2_1$	$P4/n$
a in Å	13.16990(10)	17.60897(13)
b in Å	18.44880(10)	17.60897(13)
c in Å	17.90400(10)	13.59834(15)
α in °	90	90
β in °	106.0730(10)	90
γ in °	90	90
V in Å^3	4180.07(5)	4216.52(8)
Z	2	2
T in K	100.0	99.98(16)
crystal size in mm^3	0.149 × 0.108 × 0.078	0.245 × 0.196 × 0.016
ρ_c in g cm^{-3}	1.320	1.339
F(000)	1742.0	1780.0
diffractometer	OD SuperNova	OD SuperNova
$\lambda_{XK\alpha}$ in Å	X = Cu 1.54184	X = Cu 1.54184
θ_{min} in °	5.136	6.5
θ_{max} in °	76.835	153.672
index range	−14 ≤ h ≤ 16 −23 ≤ k ≤ 21 −22 ≤ l ≤ 22	−22 ≤ h ≤ 21 −19 ≤ k ≤ 21 −17 ≤ l ≤ 16
μ in mm^{-1}	5.486	5.482
abs. correction	gaussian	gaussian
reflections collected	49599	30443
reflections unique	15854	4427
R$_{int}$	0.0396	0.0384
reflections obs. [F>2σ(F)]	15680	4355
residual density in e Å^{-3}	0.93/−0.82	0.51 / −0.81
parameters	973	275
GOOF	1.046	1.051
R$_1$ [I>2σ(I)]	0.0377	0.0293
wR$_2$ (all data)	0.0990	0.0835
CCDC	2020834	1995660

Table S3 Crystallographic Data of $[ThL_4]\cdot 3CH_3CN\cdot 4H_2O$ (**7**$\cdot 3CH_3CN\cdot 4H_2O$) and $[UL_4]\cdot 3CH_3CN\cdot 4H_2O$ (**8**$\cdot 3CH_3CN\cdot 4H_2O$).

	7$\cdot 3CH_3CN\cdot 4H_2O$	**8**$\cdot 3CH_3CN\cdot 4H_2O$
formula	$C_{74}H_{113}N_{11}O_{20}P_4Th$	$C_{74}H_{113}N_{11}UO_{20}P_4$
M_r in g mol^{-1}	1832.67	1820.64
colour, habit	yellowish, block	clear yellow, block
crystal system	tetragonal	tetragonal
space group	$P4/n$	$P4/n$
a in Å	17.74494(4)	17.68430(10)
b in Å	17.74494(4)	17.68430(10)
c in Å	13.70378(6)	13.7690(2)
α in °	90	90
β in °	90	90
γ in °	90	90
V in Å^3	4315.09(3)	4306.04(8)
Z	2	2
T in K	100.0(5)	100.0
crystal size in mm^3	0.094 × 0.070 × 0.056	0.107 × 0.065 × 0.025
ρ_c in g cm^{-3}	1.411	1.404
F(000)	1888.0	1872.0
diffractometer	OD SuperNova	OD SuperNova
$\lambda_{XK\alpha}$ in Å	X = Cu 1.54184	X = Cu 1.54184
θ_{min} in °	3.225	6.42
θ_{max} in °	76.813	76.916
index range	$-22 \le h \le 22$ $-21 \le k \le 22$ $-17 \le l \le 17$	$-14 \le h \le 22$ $-21 \le k \le 20$ $-17 \le l \le 16$
μ in mm^{-1}	6.870	6.592
abs. correction	multi-scan	gaussian
reflections collected	55344	29394
reflections unique	4563	4509
R_{int}	0.0721	0.0458
reflections obs. [F>2σ(F)]	4488	4509
residual density in e Å^{-3}	2.09 / −5.09	1.07 / −0.97
parameters	951	321
GOOF	1.058	1.061
R_1 [I>2σ(I)]	0.0626	0.0343
wR_2 (all data)	0.1710	0.0928
CCDC	1995662	1997488

Table S4 Crystallographic Data of $[NpL_4]\cdot 3CH_3CN\cdot 4H_2O$ (**9**·$3CH_3CN\cdot 4H_2O$) and $[UL_4]\cdot CH_2Cl_2$ (**8**·CH_2Cl_2).

	9·$3CH_3CN\cdot 4H_2O$	**8**·CH_2Cl_2
formula	$C_{74}H_{113}N_{11}NpO_{20}P_4$	$C_{69}H_{98}Cl_2N_8O_{16}P_4U$
M_r in g mol^{-1}	1837.63	1728.36
colour, habit	clear dark orange, block	clear yellow, block
crystal system	tetragonal	monoclininc
space group	$P4/n$	$P2_1/c$
a in Å	17.6551(7)	13.69468(8)
b in Å	17.6551(7)	24.32535(12)
c in Å	13.7559(6)	23.65863(10)
α in °	90	90
β in °	90	92.9022(4)
γ in °	90	90
V in Å^3	4287.7(4)	7871.24(7)
Z	2	4
T in K	100.0	100.0
crystal size in mm^3	0.334 × 0.324 × 0.278	0.138 × 0.082 × 0.035
ρ_c in g cm^{-3}	1.423	1.458
F(000)	1894.0	3528.0
diffractometer	Bruker D8 VENTURE	OD SuperNova
$\lambda_{XK\alpha}$ in Å	X = Mo 0.71073	X = Cu 1.54184
θ_{min} in °	4.614	5.214
θ_{max} in °	54.206	77.024
index range	$-22 \le h \le 22$ $-22 \le k \le 22$ $-17 \le l \le 17$	$-17 \le h \le 17$ $-30 \le k \le 28$ $-23 \le l \le 29$
μ in mm^{-1}	1.359	7.751
abs. correction	gaussian	gaussian
reflections collected	99347	92948
reflections unique	4740	16496
R_{int}	0.0264	0.0491
reflections obs. [$F>2\sigma(F)$]	4599	15673
residual density in e Å^{-3}	1.23 / −1.57	1.28/−2.53
parameters	315	966
GOOF	1.061	1.095
R_1 [$I>2\sigma(I)$]	0.0219	0.0403
wR_2 (all data)	0.0585	0.1090
CCDC	1995663	2020836

Table S5 Crystallographic Data of [UL_4] (**8**).

	(**8**)
formula	$C_{68}H_{96}N_8O_{16}P_4U$
M_r in g mol^{-1}	1643.43
colour, habit	clear green, block
crystal system	monoclininc
space group	$P2_1/n$
a in Å	32.05395(19)
b in Å	13.02519(5)
c in Å	36.6159(2)
α in °	90
β in °	101.1117(6)
γ in °	90
V in Å^3	15000.89(14)
Z	8
T in K	100.0
crystal size in mm^3	0.413 × 0.209 × 0.097
ρ_c in g cm^{-3}	1.455
F(000)	6720.0
diffractometer	OD SuperNova
$\lambda_{XK\alpha}$ in Å	X = Cu 1.54184
θ_{min} in °	4.918
θ_{max} in °	76.937
index range	$-40 \leq h \leq 40$
	$-11 \leq k \leq 16$
	$-46 \leq l \leq 45$
μ in mm^{-1}	7.463
abs. correction	gaussian
reflections collected	170311
reflections unique	31455
R_{int}	0.0510
reflections obs. [F>2σ(F)]	30867
residual density in e Å^{-3}	3.75/−1.93
parameters	1794
GOOF	1.156
R_1 [I>2σ(I)]	0.0596
wR_2 (all data)	0.1529
CCDC	2020837

Table S6: Selected bond lengths (Å), O$\cdots$O$_{chelate}$ distances (Å), dihedral angles of the planes (°) and hydrogen bonds of the La(III) complex **3**·3CH$_3$CN·4H$_2$O.

Selected bond lengths/ Å		**3**·3CH$_3$CN·4H$_2$O
La1	−O1	2.2608(11)
La1	−O2	2.5135(10)
P1	−O2	1.4847(11)
P1	−C2	1.7371(16)
C1	−O1	1.2596(18)

O$\cdots$O$_{chelate}$ distances/ Å		
O1	$\cdots$ O2	3.013(15)

Dihedral angles (°) of selected planes	
1 −2 Plane (1): O1, La1, O2 Plane (2): O1, C1, C2, P1, O2	7.03(6)

Hydrogen bonds

D-H $\cdots$ A	D $\cdots$ A / Å	D-H-A angle (°)
N2-H2 $\cdots$ O5	2.854(2)	147.3(8)
O5-H5AB $\cdots$ N2^{i}	2.854(2)	177.0(6)
O5-H5AA $\cdots$ O5^{ii}	2.829(4)	147.8(5)

^{i} (1/2+y, 1-x, 1-z); ^{ii} (3/2-x, 1/2-y, z)

The numeration of the atoms in the planes refers to the numeration assigned to the atoms in each complex species (see **Fig. 1** and **Fig. S32**)

Fig. S32 Molecular Structure of **3**·3CH$_3$CN·4H$_2$O. All hydrogen atoms and solvates are omitted for clarity; ellipsoids are drawn at 50% probability level.

Table S7: Selected bond lengths (Å), O$^{\cdots}$O$_{\text{chelate}}$ distances (Å), dihedral angles of the planes (°), δ and φ^5 of the planes (°) and hydrogen bonds of Ce(III) complexes CH$_3$CN⊂**4** ([CeL$_3$CH$_3$CN]) and **5**·CH$_3$CN·Et$_2$O ([CeL$_3$HL]·CH$_3$CN·Et$_2$O).

Selected bond lengths/ Å	CH$_3$CN⊂**4**	Selected bond lengths/ Å	**5**·CH$_3$CN·Et$_2$O
Ce1-O1	2.399(2)	Ce1-O4	2.408(3)
Ce1-O2	2.4198(19)	Ce1-O1	2.536(3)
Ce1-O5	2.3764(18)	Ce1-O8	2.395(3)
Ce1-O6	2.416(2)	Ce1-O5	2.441(3)
Ce1-O9	2.3724(18)	Ce1-O12	2.490(3)
Ce1-O10	2.427(2)	Ce1-O9	2.526(3)
Ce1-N7	2.678(3)	Ce1-O16	2.500(3)
		Ce1-O13	2.468(3)
P1-O2	1.500(2)	P1-O1	1.489(3)
P2-O6	1.495(2)	P2-O5	1.500(3)
P3-O10	1.503(2)	P3-O9	1.488(3)
		P4-O13	1.492(3)
P1-C2	1.737(3)	P1-C7	1.737(5)
P2-C19	1.733(3)	P2-C24	1.733(5)
P3-C36	1.731(3)	P3-C41	1.761(4)
		P4-C58	1.744(4)
C1-O1	1.284(3)	C9–O4	1.286(5)
C18-O5	1.282(3)	C27-O8	1.278(6)
C35-O9	1.283(3)	C44-O12	1.251(5)
		C61-O16	1.268(5)
O...O chelate distances/ Å		O...O chelate distances/ Å	
O1 $\cdots$ O2	2.918(3)	O1 $\cdots$ O4	2.926(4)
O5 $\cdots$ O6	2.933(2)	O5 $\cdots$ O8	2.981(4)
O9 $\cdots$ O10	2.917(3)	O9 $\cdots$ O12	2.983(4)
		O13 $\cdots$ O16	2.914(4)

Dihedral angles (°) of selected planes		Dihedral angles (°) of selected planes	
Plane (1): O1, Ce1, O2		Plane (1): O1, Ce1, O4	
1-2 Plane (2): O1, C1, C2, P1, O2	26.33(11)	1-2 Plane (2): O1, P1, C7, C9, O4	5.28(18)
Plane (3): O5, Ce1, O6		Plane (3): O5, Ce1, O8	
3-4 Plane (4): O5, C18, C19, P2, O6	17.94(12)	3-4 Plane (4): O5, P2, C24, C27, O8	10.47(13)

5-6	Plane (5): O9, Ce1, O10 Plane (6): O9, C35, C36, P3, O10	22.69(9)	5-6	Plane (5): O9, Ce1, O12 Plane (6): O9, P3, C41, C44, O12	3.87(15)
			7-8	Plane (7): O13, Ce1, O16 Plane (8): O13, P4, C58, C61, O16	3.69(14)
			9-10 δ_1	Plane (9): O1, O5, O6 Plane (10): O1, O5, O13	10.39(15)
			11-12 δ_2	Plane (11): O2, O10, O14 Plane (12): O9, O10, O14	20.15(14)
			13-14 δ_3	Plane (13): O5, O6, O10 Plane (14): O5, O9, O10	42.01(14)
			15-16 δ_4	Plane (15): O1, O2, O14 Plane (16): O1, O13, O14	43.90(14)
			17-18 φ_1	Plane (17): O1, Ce1, O10 Plane (18): O9, Ce1, O13	15.88(13)
			19-20 φ_2	Plane (19): O5, Ce1, O14 Plane (20): O2, Ce1, O6	16.18(11)

Hydrogen bonds	
D-H $\cdots$ A / Å	
N5-H5 $\cdots$ N7^i	2.754(5)
D-H-A angle (°)	
N5-H5 $\cdots$ N7	151.5(3)

^{i} (1-x, -1/2+y, 1-z)

The numeration of the atoms in the planes refers to the numeration assigned to the atoms in each complex species (see **Fig. 2** and **Fig. S33**).

Fig. S33 Representation of hydrogen bond interactions between N5 and N7' present in the crystal structure of **5**·CH$_3$CN·Et$_2$O ([CeL$_3$HL]·CH$_3$CN·Et$_2$O). All carbon hydrogen atoms and solvates are omitted for clarity; ellipsoids are drawn at 50% probability level.

Table S8: Selected bond lengths (Å), O···O$_{chelate}$ distances (Å), dihedral angles of the planes (°), and δ and φ[5] of the planes (°) of **6 – 9**.

Selected bond lengths/ Å		**6**·2CH$_3$CN· 4H$_2$O	**7**·3CH$_3$CN· 4H$_2$O	**8**·3CH$_3$CN· 4H$_2$O	**9**·3CH$_3$CN· 4H$_2$O
Ce1/Th1/U1/Np1–O1		2.3356(14)	2.3571(15)	2.304(2)	2.2990(12)
Ce1/Th1/U1/Np1–O2		2.4173(14)	2.4320(16)	2.388(2)	2.3766(12)
P1-O2		1.4935(15)	1.5014(16)	1.502(2)	1.4955(13)
P1-C2		1.733(2)	1.728(3)	1.724(4)	1.725(2)
C1-O1		1.280(2)	1.285(3)	1.293(4)	1.283(2)
O···O$_{chelate}$ distances/ Å					
O1 ··· O2		2.9589(19)	2.934(2)	2.916(3)	2.9269(18)
Dihedral angles (°) of selected planes					
1-2	Plane (1): O1, Ce1/Th1/U1/Np1, O2 Plane (2): O1, C1, C2, P1, O2	1.43(3)	2.02(7)	1.53(12)	2.41(6)
3-4 δ$_1$	Plane (3): O1, O1', O1'' Plane (4): O1, O1'', O1'''	0	0	0	0
5-6 δ$_2$	Plane (5): O2, O2', O2'' Plane (6): O2, O2'', O2'''	0	0	0	0
7-8 δ$_3$	Plane (7): O1, O1', O2 Plane (8): O2, O2', O1'	49.53(5)	48.13(6)	49.43(8)	50.09(3)
9-10 δ$_4$	Plane (9): O1'', O1''', O2'' Plane (10): O1''', O2'', O2'''	49.53(5)	48.13(6)	49.43(8)	50.09(3)
11-12 φ$_1$	Plane (11): O1, Ce1/Th1/U1/Np1, O2 Plane (12): O1''', Ce1/Th1/U1/Np1, O2'	26.79(4)	26.97(4)	25.89(15)	25.35(2)
13-14 φ$_2$	Plane (13): O1, Ce1/Th1/U1/Np1, O2''' Plane (14): O1', Ce1/Th1/U1/Np1, O2''	23.04(4)	21.96(4)	22.94(6)	23.46(2)

The numeration of the atoms in the planes refers to the numeration assigned to the atoms in each complex species (see **Fig. 3** and **Fig. 4**).
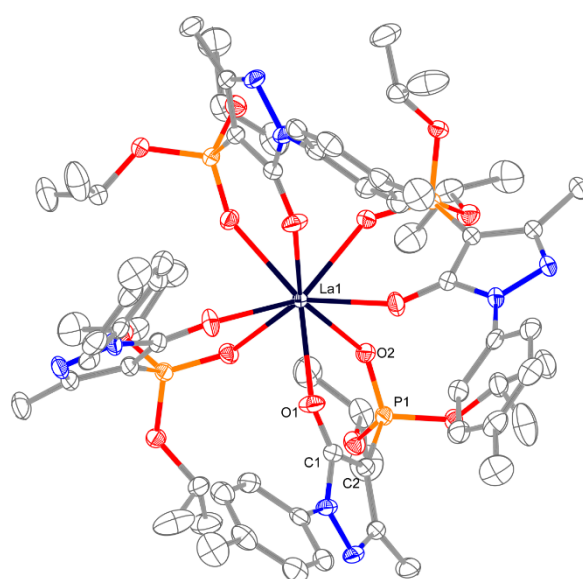
Table S9: Selected bond lengths (Å), O···O$_{chelate}$ distances (Å), dihedral angles of the planes (°), and δ and φ^5 of the planes (°) of the U(IV) complex **8**·2CH$_2$Cl$_2$.

Selected bond lengths/ Å	**8**·2CH$_2$Cl$_2$
U1–O1/O5/O9/O13	2.312(2) / 2.303(2) / 2.305(2) / 2.289(2)
U1–O2/O6/O10/O14	2.423(3) / 2.399(3) / 2.387(3) / 2.402(3)
P1-O2	1.497(3)
P1-C2	1.728(4)
P2-O6	1.502(3)
P2-C19	1.729(4)
P3-O10	1.500(3)
P3-C36	1.723(4)
P4-O14	1.510(3)
P4-C53	1.738(3)
C1-O1	1.295(5)
C18-O5	1.284(5)
C35-O9	1.285(4)
C52-O13	1.281(4)
O···O$_{chelate}$ distances/ Å	
O1 ··· O2	2.811(4)
O5 ··· O6	2.803(4)
O9 ··· O10	2.876(4)
O13 ··· O14	2.863(4)

Dihedral angles (°) of selected planes		
1-2	Plane (1): O1, U1, O2 Plane (2): O1, C1, C2, P1, O2	2.17(14)
3-4	Plane (3): O5, U1, O6 Plane (4): O5, C18, C19, P2, O6	11.75(14)
5-6	Plane (5): O9, U1, O10 Plane (6): O9, C35, C36, P3, O10	15.38(13)
7-8	Plane (7): O13, U1, O14 Plane (8): O13, C52, C53, P4, O14	12.45(12)
9-10 δ$_1$	Plane (9): O1, O2, O9 Plane (10): O1, O9, O13	2.61(14)
11-12	Plane (11): O5, O6, O14	4.75(14)

δ_2	Plane (12): O6, O10, O14	
13-14	Plane (13): O1, O5, O6	
δ_3	Plane (14): O1, O2, O6	48.20(12)
15-16	Plane (15): O9, O13, O14	
δ_4	Plane (16): O9, O10, O14	46.35(12)
17-18	Plane (17): O10, U1, O2	
φ_1	Plane (18): O1, U1, O14	20.93(9)
19-20	Plane (19): O6, U1, O9	
φ_2	Plane (20): O5, U1, O13	19.46(8)

The numeration of the atoms in the planes refers to the numeration assigned to the atoms in the complex species (see **Fig. S34**).
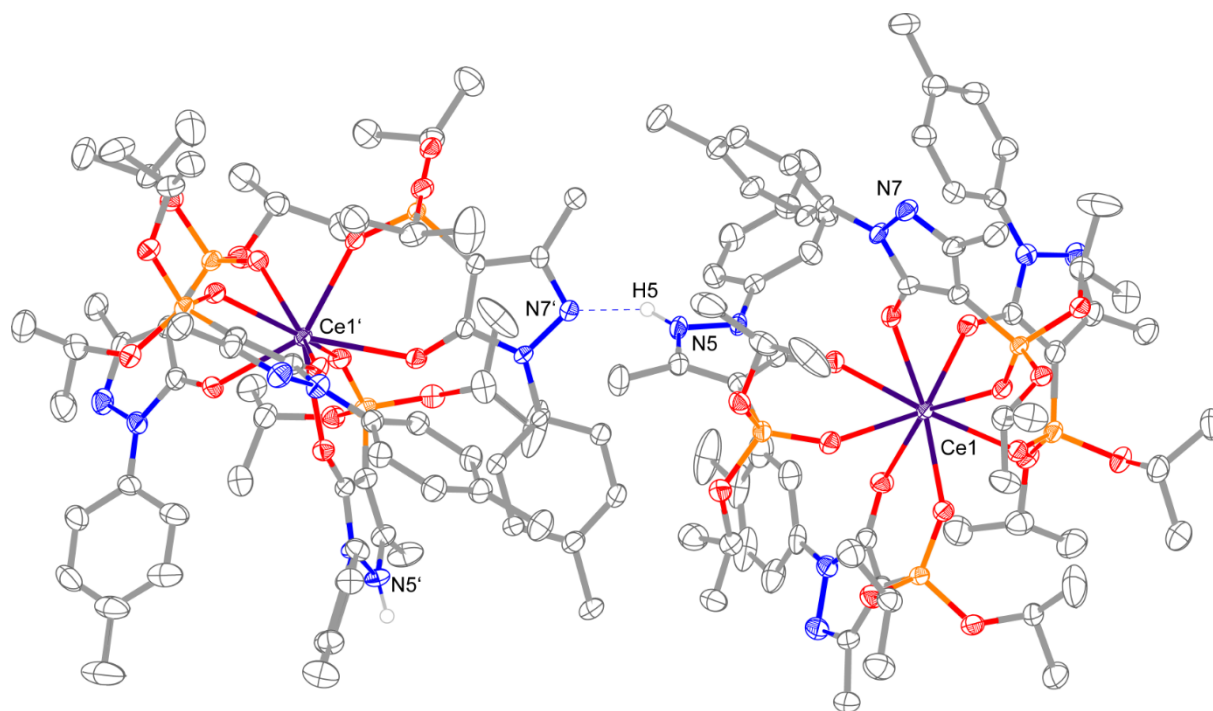

Fig. S34 Molecular structure of **8**·2CH$_2$Cl$_2$ with selected atom labelled. All hydrogen atoms and solvates are omitted for clarity; ellipsoids are drawn at 50% probability level.

Table S10: Selected bond lengths (Å), O$\cdots$O$_{chelate}$ distances (Å), dihedral angles of the planes (°), and δ and φ^5 of the planes (°) of the U(IV) complex **8**.

Selected bond lengths/ Å	**8**
U1A–O1A/O5A/O9A/O13A	2.260(4) / 2.278(4) / 2.301(4) / 2.357(4)
U1B–O1B/O5B/O9B/O13B	2.279(4) / 2.347(4) / 2.284(4) / 2.327(5)
U1A–O2A/O6A/O10A/O14A	2.443(4) / 2.416(4) / 2.385(4) / 2.393(4)
U1B–O2B/O6B/O10B/O14B	2.370(4) / 2.379(4) / 2.364(4) / 2.389(4)
P1A-O2A / P1B-O2B	1.503(5) / 1.510(5)
P1A-C2A / P1B-C2B	1.730(7) / 1.731(7)
P2A-O6A / P2B-O6B	1.513(5) / 1.508(5)
P2A-C19A / P2B-C53B	1.728(6) / 1.733(7)
P3A-O10A / P3B-O10B	1.510(4) / 1.505(4)
P3A-C36A / P3A-C19B	1.729(7) / 1.717(7)
P4A- O14A / P4B-O14B	1.505(5) / 1.510(5)
P4A-C53A / P4B-C36B	1.729(6) / 1.727(7)
C1A-O1A / C1B-O1B	1.301(7) / 1.299(8)
C18A-O5A / C18B-O5B	1.298(8) / 1.295(7)
C35A-O9A / C35B-O9B	1.291(7) / 1.299(8)
C52A-O13A / C52B-O13B	1.299(8) / 1.288(8)
O$\cdots$O$_{chelate}$ distances/ Å	
O1A $\cdots$ O2A / O1B $\cdots$ O2B	2.784(6) / 2.774(6)
O5A $\cdots$ O6A / O5B $\cdots$ O10B	2.786(6) / 2.773(6)
O9A $\cdots$ O10A / O9B $\cdots$ O14B	2.739(7) / 2.760(6)
O13A $\cdots$ O14A / O13B $\cdots$ O6B	2.827(7) / 2.757(6)

Dihedral angles (°) of selected planes

1-2	Plane (1): O1A, U1A, O2A Plane (2): O1A, C1A, C2A, P1A, O2A	9.2(2)
3-4	Plane (3): O5A, U1A, O6A Plane (4): O5A, C18A, C19A, P2A, O6A	6.5(2)
5-6	Plane (5): O9A, U1A, O10A Plane (6): O9A, C35A, C36A, P3A, O10A	2.3(2)
7-8	Plane (7): O13A, U1A, O14A Plane (8): O13A, C52A, C53A, P4A, O14A	12.2(2)

9-10	Plane (9): O1B, U1B, O2B	2.2(2)
	Plane (10): O1B, C1B, C2B, P1B, O2B	
11-12	Plane (11): O5B, U1B, O10B	11.2(2)
	Plane (12): O5B, C18B, C19B, P3B, O10B	
13-14	Plane (13): O9B, U1B, O14B	8.02(2)
	Plane (14): O9B, C35B, C36B, P4B, O14B	
15-16	Plane (15): O13B, U1B, O6B	0.9(2)
	Plane (16): O13B, C52B, C53B, P2B, O6B	
17-18 δ_1	Plane (17): O1A, O2A, O5A	17.6(2)
	Plane (18): O1A, O5A, O6A	
19-20 δ_2	Plane (19): O9A, O10A, O14A	9.7(2)
	Plane (20): O10A, O13A, O14A	
21-22 δ_3	Plane (21):O5A, O9A, O10A	45.62(19)
	Plane (22): O5A, O6A, O10A	
23-24 δ_4	Plane (23): O1A, O2A, O14A	44.85(19)
	Plane (24): O1A, O13A, O14A	
25-26 φ_1	Plane (25): O5A, U1A, O14A	20.08(19)
	Plane (26): O6A, U1A, O13A	
27-28 φ_2	Plane (27): O2A, U1A, O9A	16.20(15)
	Plane (28): O1A, U1A, O10A	
29-30 δ_5	Plane (29): O1B, O2B, O9B	12.9(3)
	Plane (30): O1B, O9B, O14B	
31-32 δ_6	Plane (31): O5B, O6B, O10B	18.6(3)
	Plane (32): O6B, O10B, O13B	
33-34 δ_7	Plane (33): O1B, O2B, O6B	43.7(2)
	Plane (34): O1B, O6B, O13B	
35-36 δ_8	Plane (35): O9B, O5B, O10B	40.3(2)
	Plane (36): O9B, O10B, O14B	
37-38 φ_3	Plane (37): O1B, U1B, O10B	11.09(18)
	Plane (38): O2B, U1B, O5B	
39-40 φ_4	Plane (39): O6B, U1B, O9B	15.86(16)
	Plane (40): O13B, U1B, O14B	

The numeration of the atoms in the planes refers to the numeration assigned to the atoms in the complex species (see **Fig. S35**).
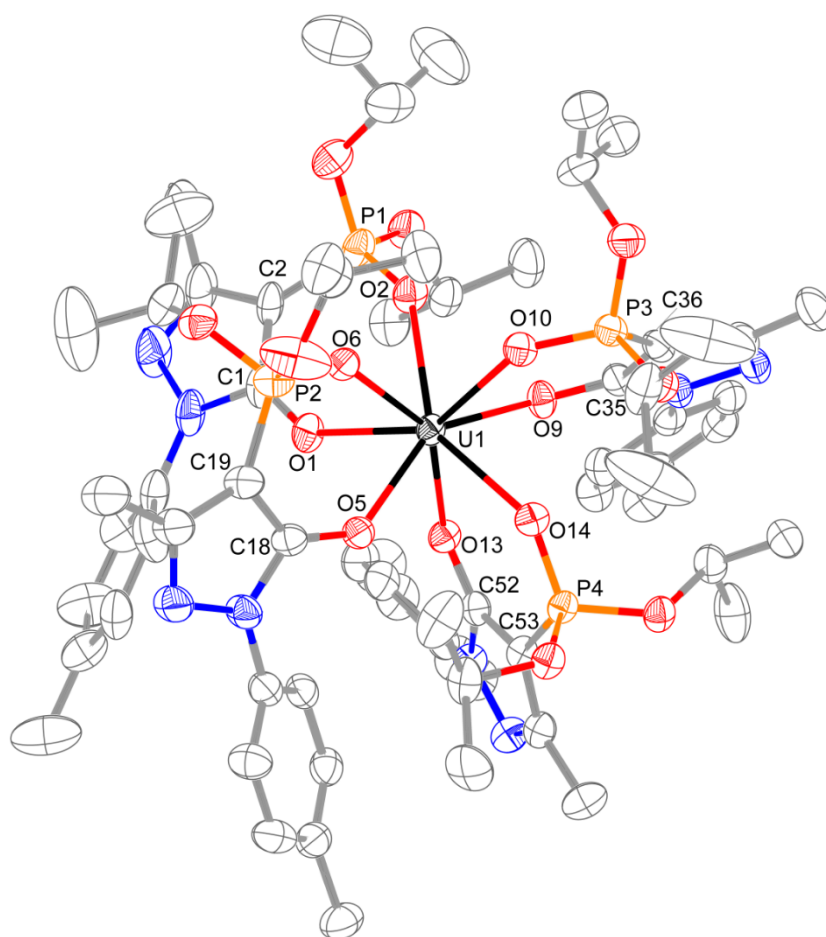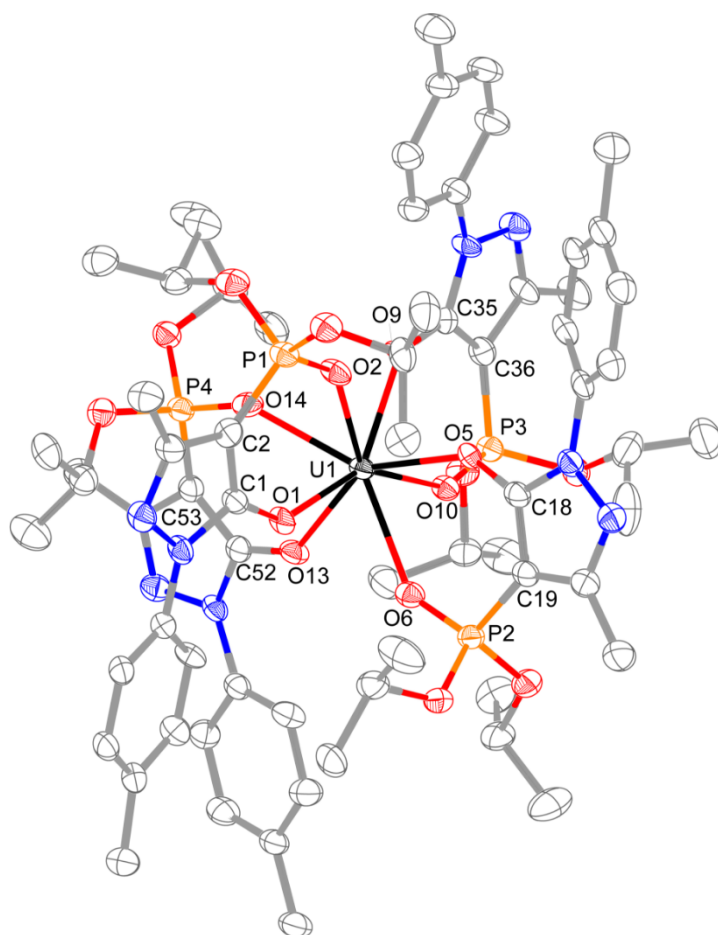
Fig. S35 Representation of the molecule A of the molecular structure of **8** with selected atom labelled. All hydrogen atoms are omitted for clarity; ellipsoids are drawn at 50% probability level.

EXAFS

The Np and UL_{III} –edge (17610 eV (Np), 17166 eV (U)) extended X-ray absorption fine structure (EXAFS) spectra were collected at the Rossendorf beamline (ROBL, BM20) at the European Synchrotron Radiation Facility (ESRF)[15] under dedicated ring operation conditions of an electron energy of 6 GeV and a beam current of 200 mA. Two Rh-coated mirrors and a water cooled Si(111) double crystal monochromator were used for rejection of higher order harmonics and to monochromatize the incident white X-ray beam. The signal of the $L\alpha_{1,2}$ fluorescence lines was recorded with a 13-element Ge detector. For each sample multiple energy scans were performed in order to reach a sufficient signal-to-noise ratio after averaging (Np: 18 scans, U: 13 scans). For each energy scan the Y K-edge (17038 eV) absorption spectrum of a Y metal foil was measured simultaneously. The incident photon flux and the absorption spectrum of the Y metal foil was measured with gas filled ionization chambers. The data treatment, which includes the energy calibration, statistical weighting of the 13 fluorescence channels and their dead-time correction, averaging of the multiple sample scans, extraction of the EXAFS signal, and the shell fitting was accomplished with the program suite of EXAFSPAK.[16] In order to calculate the photoelectron kinetic energy the ionization potential (E_0) of the Np and UL_{III} –edge was set arbitrary to 17620 eV and to 17185 eV, respectively, and was defined as a free parameter as $\Delta E_0 = E_0 - E_t$ (ΔE_0 – shift in energy threshold, E_t – theoretical ionization potential) in the shell fit procedure. The expected EXAFS radial resolution is 0.12 Å and 0.13, as given by the maximum available k-interval of 1.0 - 13.6 $Å^{-1}$ (U) and 1.7 - 13.6 $Å^{-1}$ (Np), respectively. Theoretical scattering phase and amplitude functions where calculated with the ab-initio scattering code FEFF8.20[17] based on the XRD structural data of **8**·$3CH_3CN·4H_2O$ and **9**·$3CH_3CN·4H_2O$ in the case of the U(IV) complexes and the Np(IV) complex, respectively.

Shell fit procedure

In equation (1) the structural parameter S_0^2, N, σ^2, and r can be fitted by common algorithms like the Levenberg-Marquardt algorithm. All other scattering phase and amplitude functions are available by theoretical *ab-initio* calculations on structural models or XRD data. For inspection of structural features a k-interval (k_{min}, k_{max}) of the EXAFS signal is Fourier-transformed by equation (2), whereby commonly the power spectrum is used (equation (3)) for visualization.

$$\chi(k) = S_0^2 \sum_{j=1}^{types} N_j S_j(k,r_j) F_j(k,r_j) e^{-2\sigma_j^2 k^2} e^{-2r_j/\lambda_j(k,r_j)} \frac{\sin(2kr_j + \varphi_j(k,r_j) + \varphi_c(k))}{kr_j^2} \tag{1}$$

$\chi(k)$ - experimental EXAFS spectrum; S_0^2- amplitude reduction factor; j – number of the backscattering atom; N_j – coordination number; $S_i(k,r_j)$ - total atomic loss factor; $F_j(k,r_j)$ - effective backscattering amplitude; σ_j - Debye-Waller factor; r_j – distance between absorbing atom and backscattering atom; $\lambda_j(k,r_j)$ – effective free path length of the photoelectron; $\phi_j(k,r_j)$ – phase shift of the photoelectron due to the interaction with the potential of the backscattering atom; $\phi_c(k)$ – phase shift of the photoelectron due to the interaction with the potential of the absorbing atom.

$$p(r) = \frac{1}{2\pi} \int_{k_{min}}^{k_{max}} \chi(k) e^{i(2kr)} dk \tag{2}$$

$$|p(r)| = \left\{ [p_{real}(r)]^2 + [p_{imag}(r)]^2 \right\}^{1/2} \tag{3}$$

An important property of the Fourier transform (FT) is possibility that structural features, which fall in a given r-interval (r_1, r_2), can be back transformed (equations (4) – (6)).

$$z(k) = \frac{1}{2\pi} \int_{r_1}^{r_2} p(r) e^{-i(2kr)} dr \tag{4}$$

$$A(k) = \left\{ [z_{real}(k)]^2 + [z_{imag}(k)]^2 \right\}^{1/2} \tag{5}$$

$$\Phi(k) = \arctan\left\{ \frac{z_{imag}(k)}{z_{real}(k)} \right\}, \text{ with } \Phi(k) = 2kr + \phi(k) \tag{6}$$

The EXAFS signal is then reconstructed as:

$$\chi_{r1-r2}(k) = A(k)\sin(\Phi(k)) \tag{7}$$

The EXAFS equation (equation (1)) has some general drawbacks. The radial particle distribution function $n(r)$, describing the density of interatomic distances in matter, is approximated by pure Gaussians shapes. The full width at the half maximum (FWHM) of $n(r)$ is given by σ, which measures the radial structural and thermal atomic disorder. In the case that $n(r)$ is non-Gaussian strong deviations between $\chi(k)$ and the fit can occur so that an accurate determination of structural parameter (r, N) is spoiled. Although, common shell fit analysis enables the inclusion of single scattering (SS) events, but also higher order scattering events, i.e. multiple scattering (MS) of the electron wave on more than one backscattering atom can be included. However, due to the strong angular dependency of the scattering amplitude of the MS contributions the results of the shell fit would be strongly influenced by the structural model used for prior calculation of the scattering phases and amplitudes. If the structural model is inaccurate, a shell fit will probably result in a poor description of the experimental $\chi(k)$, while unknown deviations between the true structure, probed by EXAFS, and the structural parameter gained by the shell fit must be considered.

Monte-Carlo (MC) simulation of EXAFS spectra

Basing on equation (1) the EXAFS oscillation of a backscattering atom i of the type j at the radial distance $r_{j,i}$ can be rewritten as:

$$\chi_j(k,r_{j,i}) = S_0^2 S_j(k,r_{j,i}) F_j(k,r_{j,i}) e^{-2r_j/\lambda_j(k,r_{j,i})} \frac{\sin(2kr_{j,i} + \varphi_j(k,r_{j,i}) + \varphi_c(k))}{kr_{j,i}^2} \tag{8}$$

were the radial absorber-backscatter distance is given by:

$$r_{j,i} = \left(dx_{j,i}^2 + dy_{j,i}^2 + dz_{j,i}^2\right)^{1/2} \tag{9}$$

For more than one molecule ($N_{molecule}$) and with N_{atoms}^j being the total number of atoms of type j, the total EXAFS signal becomes:

$$\chi(k) = \frac{1}{N_{molecule}} \sum_{j=1}^{types} \sum_{i=1}^{N_{atoms}^j} \chi_j(k,r_{j,i}) \tag{10}$$

The radial particle distribution function $n_j(r)$ can be calculated for each type of backscattering atoms by

$$n_j(r) = \frac{1}{N_{molecule}} \sum_{j=1}^{types} \sum_{i=1}^{N_{atoms}^j} \delta(r - \bar{r}_{j,i}) \tag{11}$$

where δ is the Kronecker delta function and $\bar{r}_{j,i} = r$ if $r-dr/2<r_{j,i}<r+dr/2$, while dr is the predefined bin-width used for the histogram of $n_j(r)$.

By inspection of equations (8) and (9) it is obvious that for each type of an atom and for each set of Cartesian coordinates a theoretical EXAFS spectrum can be calculated, owing the possibility to calculate for a large number of molecules the total EAXFS signal (equation (10)). Moreover, opposite to shell fit methods, for each arbitrary atomic configuration the scattering phases and amplitudes can be precisely calculated for SS and MS events by *ab-initio* calculations. At the moment, only MC approaches enables both, the calculation of $n(r)$ without assumptions about its shape and the inclusion of MS, while their scattering phase and amplitude functions can be updated in dependence on the structural changes during the simulation. The MC approach does not include gradient descent algorithms, like the Levenberg-Marquardt algorithm as used in shell fit procedures, which does not guaranty the convergence to a global minimum in the case of an extensive multi-shell fit scenario.

MC starts with a statistical ensemble of metal complexes which is gained by the replication of the initial complex structure. For the whole set of backscattering atoms the theoretical $\chi(k)_{theo}$ is calculated (equation (10)) and compared with the experimental $\chi(k)$. If a randomly picked atom is moved by a random distance from its origin the new $\chi(k)_{theo}$ will result in a better or poorer fit. If only the proposed movements, which lead to an improvement of the fit would be accepted, then an over-fitting will take place, while $n(r)$ become unstable in respect to the experimental error. Moreover, the risk of a convergence into a local minimum could not be avoided. Here we use the Markov chain Monte-Carlo (MCMC) algorithm[18] where the Markov chain is accomplished by introducing the Metropolis algorithm,[19] which measures for each proposed move of an atom its relative probability to be accepted or rejected. As an acceptance criterion, the relative probability of a move is calculated according the Boltzmann factor for which the difference in energy is replaced by the change of the sum of squared errors, caused by the particular move, and by replacing k_bT (k_b - Boltzmann constant, T - temperature) by a multiple of the expected experimental error. Various studies have shown that this kind of *importance sampling* is well suited for analysing XAS spectra and data from other spectroscopic techniques.[20-25] After numerous atomic movements the Markov chain converges to a stationary distribution for which $\chi(k)_{theo}$ should fluctuate around a constant average in the size of the expected experimental error.

The Metropolis algorithm was included in our MCTFA code [26] as proposed by Gurman et al.[25] and McGreevy[23] For SS paths the $\chi_j(k,r_{j,i})$ is calculated according our procedure as described in the literature.[27] MS paths up to the 4th order are calculated and updated during the simulation with a pre-defined spatial precision by using FEFF8.20.[17]

Shell Fit

Figure S36 displays the most important scattering paths for shell fit, which are also summarized in **Table S11.**
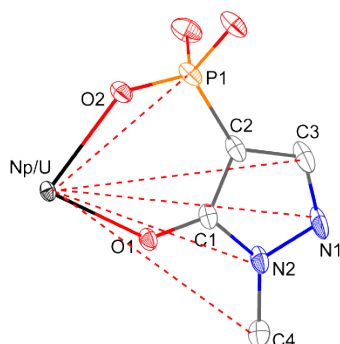

Fig. S36 Structural fragment taken from XRD structure of **8**·3CH$_3$CN·4H$_2$O and **9**·3CH$_3$CN·4H$_2$O. Ellipsoids are drawn at 50% probability level.

Table S11 Single scattering (SS) and multiscattering (MS) paths used for the shell fit.

Path	r / Å	n
U/Np–O1	2.30/2.30	4
U/Np–O2	2.39/2.38	4
U/Np–C1	3.37/3.34	4
U/Np–O1–C1	3.48/3.46	8
U/Np–O1–C1–O1	3.60/3.58	4
U/Np–P	3.66/3.63	4
U/Np–O2–P	3.78/3.75	8
U/Np–O2–P–O2	3.89/3.87	4
U/Np–C2	3.93/3.91	4

r – radial distance, *n* – coordination number.

Since the three mixed isomers of the U(IV) complex (**8**·3CH$_3$CN·4H$_2$O, **8**·CH$_2$Cl$_2$, **8**) are structurally similar with **9** we fitted the spectra (**Fig. S37**) of both samples with identical settings for the EXAFS structural parameter. All coordination numbers were fixed according to the structural model (**Table S11**). For paths with r > r$_{Np/U\text{-}O2}$ several parameter are highly correlated and were kept constant or linked during the fit to avoid physically unrealistic results (**Table S12**). For the first shell (maximum at 1.8 Å in the FT), which consists of O1 and O2, all parameter, except for *n*, could be fitted freely and resulted in physically reliable σ^2 for both samples. In the case of both samples the resulting *r* agrees with the average of the XRD structural data up to a maximum deviation of 0.035 Å and 0.031 Å for the U-P and the Np-P interaction, respectively. Note that the common uncertainty in determination of radial distances by EXAFS is 0.02 Å[28], hence the shell fit radial distances support the XRD structural data.
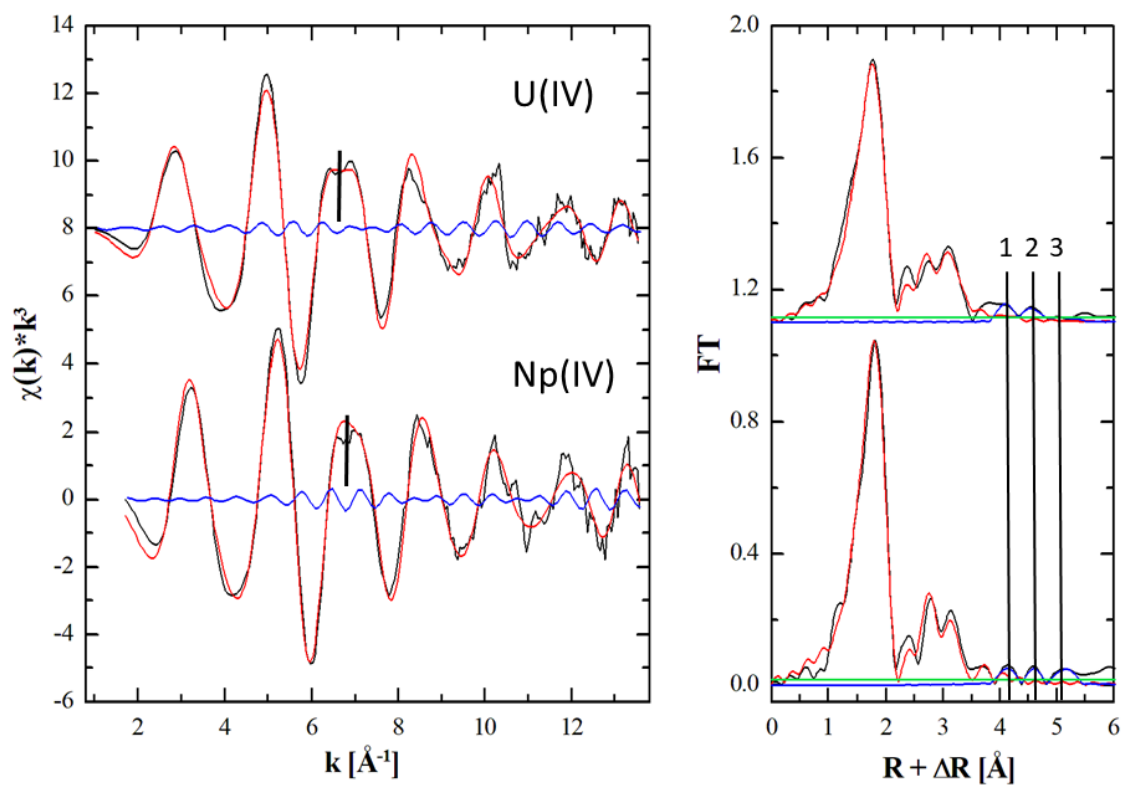
Fig. S37 Experimental (black) k^3-weighted EXAFS spectra of the U(IV) and Np(IV) complexes in toluene solution with shell fit (red) and corresponding FT (right). Level of experimental error (green line). The three marked MS peaks in the FT are FT-filtered in range of 3.94 Å – 5.40 Å and FT back transformed (blue).

Chemical Science

Table S12 EXAFS shell fit parameter for the U(IV) and Np(IV) complexes in solution.

Path/sample	n	r /Å	Δr/Å	σ^2/Å^2	ΔE_0/Ev
8·3CH$_3$CN·4H$_2$O, 8·CH$_2$Cl$_2$, 8					
U–O1	4	2.30(1)	0.00^a	0.0059(9)	1.9(3)
U–O2	4	2.39(1)	0.00^a	0.008(2)	1.9/
U–C1	4	3.361(8)	0.022^a	0.0034(5)	1.9/
U–O1–C1	8	3.480/		0.0034/	1.9/
U–O1–C1–O1	4	3.598/		0.0034/	1.9/
U–P	4	3.647(5)	0.035^a	0.0064(8)	1.9/
U–O2–P	8	3.72(1)		0.0064/	1.9/
U–O2–P–O2	4	3.83/		0.0064/	1.9/
U–C2	4	3.97(1)	0.00^a	0.005	1.9/
9·3CH$_3$CN·4H$_2$O					
Np–O1	4	2.278(7)	0.020	0.0052(9)	9.87(4)
Np–O2	4	2.369(9)	0.008	0.006(1)	9.87/
Np–C1	4	3.337(5)	0.007	0.0017(4)	9.87/
Np–O1–C1	8	3.455/		0.0017/	9.87/
Np–O1–C1–O1	4	3.572/		0.0017/	9.87/
Np–P	4	3.605(6)	0.031	0.0060(9)	9.87/
Np–O2–P	8	3.69(2)		0.0060/	9.87/
Np–O2–P–O2	4	3.809/		0.0060/	9.87/
Np–C2	4	3.94(1)	-0.03	0.005	9.87/

/-linked parameter. n – coordination number, r – radial distance, σ^2 – Debye-Waller factor, ΔE_0 - shift in energy threshold, Δr - modulus of the difference between shell fit distances and the corresponding distances supplied by the XRD structure. ^{a} – calculated with average distances taken from XRD structural data of **8·3CH$_3$CN·4H$_2$O**, **8·CH$_2$Cl$_2$**, and **8**, respectively. Estimated standard deviations of the variable parameter as given from EXAFSPAK in parenthesis.

The shell fitting might suffer from several drawbacks so that slight differences between the fit and the experiment can be caused by an intrinsic property of the shell fit method. However, the XRD structural data are not only supported by the shell fitted structural parameter, since the spectra of both systems are very similar and since they show the same strong structural features, which were taken into account for shell fitting. Especially the back transformation of the FT interval in the range of 3.94 Å – 5.40 Å (**Fig. S37**) contains a negative oscillation, which is responsible for the fine structure observed at 6.8 Å^{-1} and 6.6 Å^{-1} in the case of both systems, respectively. Following the numbering of the MS peaks as given in **Fig. S37** and with **Fig. S35**, the back transformed EXAFS signal consists of: peak 1: U/Np–O1–N2; peak 2: U/Np–O1–C4, U/Np–C2–C3; peak 3: U/Np–C1–N1. In total and with inclusion of SS and all related MS paths, twelve additional paths would be necessary for the description of these spectral features. Note that all these MS paths show focusing effect, hence a strong spectral amplitude due

to the small scattering angle and are therefore of high relevance. However, the scattering amplitudes and phases of these paths are very similar so that the fitted structural parameter would have strong correlations, thus a shell fit would be not conclusive.

Monte-Carlo simulation

The starting structural model for U(IV) complex was constructed by using the XRD structural data of the three isomers **8**·3CH$_3$CN·4H$_2$O, **8**·CH$_2$Cl$_2$ and **8** (**Fig. S38**), while for the Np(IV) complex we used the XRD structural data of **9**·3CH$_3$CN·4H$_2$O (**Fig. S39**). Hydrogen atoms where removed due to their small EXAFS scattering amplitude, and only atoms in radial distances less than 7 Å were included, so that the models contain 258 and 87 backscattering atoms in the case of the U(IV) complexes and the Np(IV) complex, respectively. To get a statistically proper distribution of $n(r)$ the models were replicated 200 times, hence in total the models for the U(IV) complexes and the Np(IV) complex consist of 51600 and 17400 backscattering atoms, respectively. For all types of backscattering atoms all SS paths where calculated with a resolution of 0.02 Å up to 6 Å, while the MS paths up to the fourth order with scattering angles $\geq 125°$ and r $\leq$ 6 Å were included and automatically updated by *ab-inito* calculations performed by FEFF8.20.[17] The backscattering atoms were moved successively along a random vector with a random length of 0.03 Å. The convergence of the Markov chain was reached after ~1x10^7 ~4x10^6 atomic movements in the case of the U(IV) and the Np(IV) system, respectively. For receiving a smooth $n(r)$ and a stable average structure the MC was performed for the U(IV) and the Np(IV) system further up to 1.6x10^7 and 6x10^6 atomic movements, respectively, for which all atomic coordinates were stored 6 times in between. In total about 1.1x10^7 and 1.3x10^6 MS events were automatically calculated and updated for the simulation of the U(IV) complexes and the Np(IV) complex, respectively.

The MC resulted in the 3D particle distribution shown in **Fig. S38** and **Fig. S39** and in the fit of the experimental EXAFS spectra shown in **Fig. S40**. According equation (9) and equation (11) the radial pair distributions for all scattering atoms, inclusively for all MS paths are available in 2- and 3D Euclidean space (not shown here). The quality of the MC fit outperforms the shell fit procedure (**Fig. S37**) as visible in the low residual, which mainly consists in contributions stemming from effects of background subtraction, hence visible in the lower r-range of the FT (**Fig. S40**). As expected, the influence of the MS contributions above ~2.5 Å is very strong as shown in **Fig. S40**.
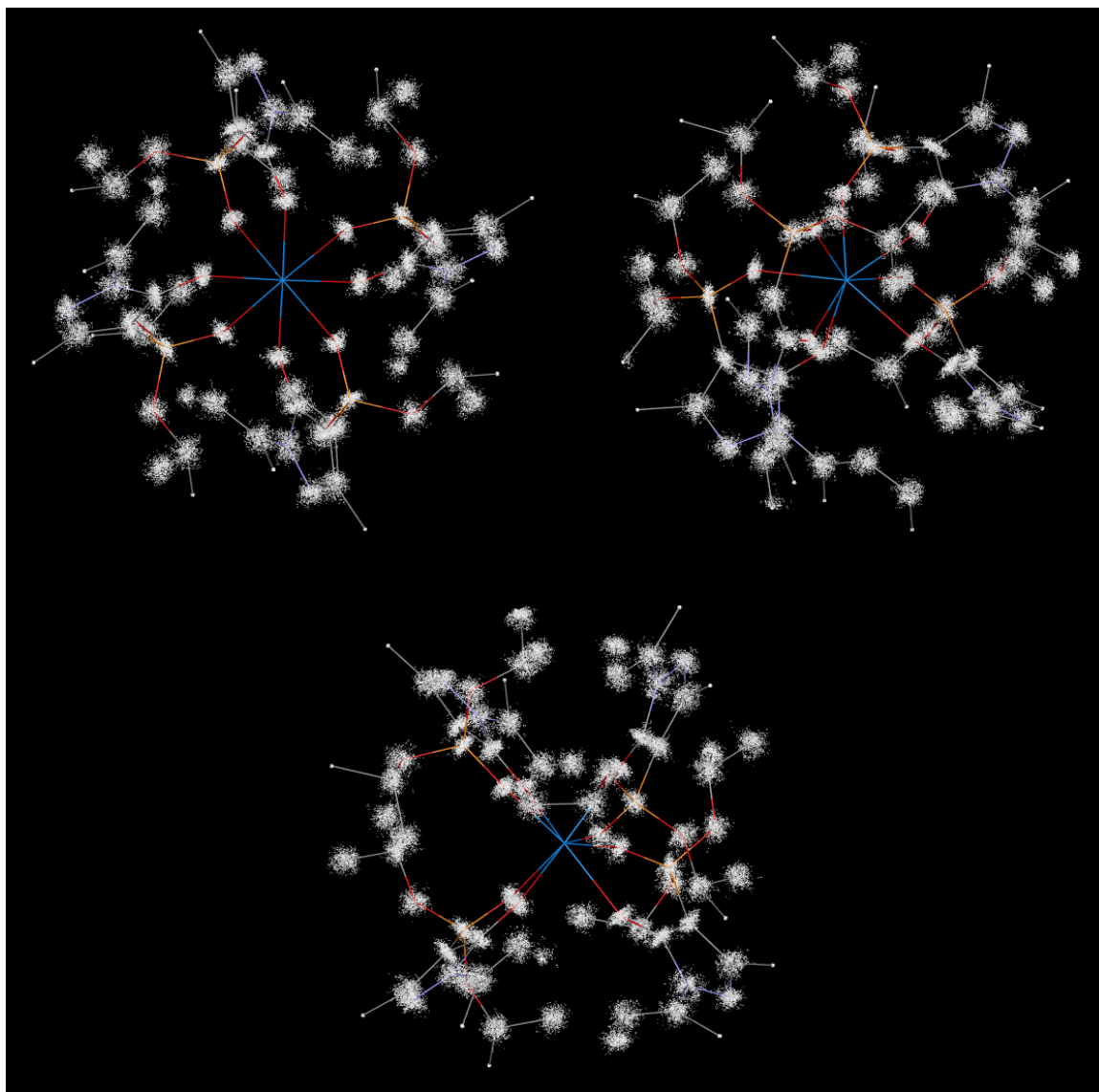
Fig. S38 3D Particle distribution gained by MC simulation of the U(IV) complexes solved in toluene solution. **8**·3CH$_3$CN·4H$_2$O (upper left), **8**·CH$_2$Cl$_2$ (upper right), and **8** (lower middle). CH$_3$CN entity in **8**·3CH$_3$CN·4H$_2$O omitted for better visualization.
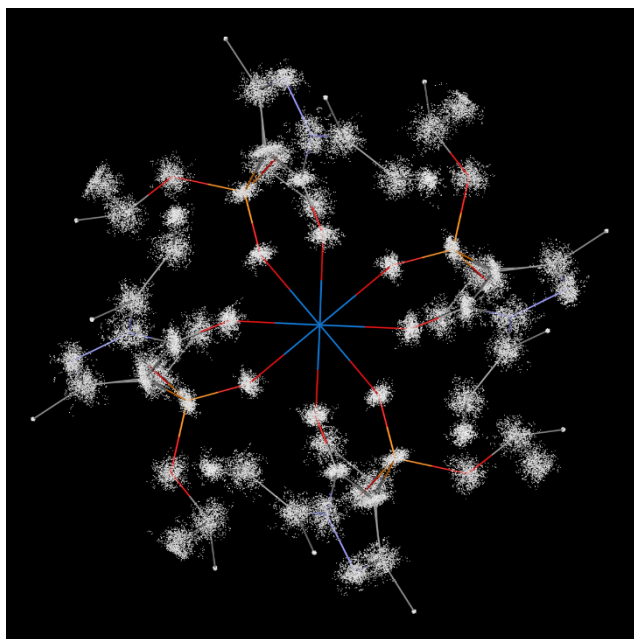
Fig. S39 3D Particle distribution gained by MC simulation of the Np(IV) complex (**9**·3CH$_3$CN·4H$_2$O) solved in toluene solution.

The fine structure at 6.8 Å^{-1} and 6.6 Å^{-1} in the k-space, which is typical for both systems, is well reproduced by the MC fit (vertical line **Fig. S40**), hence supports again that the structures in the liquid phase are up to 6 Å in accordance with the solid phase structures provided by the XRD measurements.

Fig. S40 Experimental (black) k^3-weighted EXAFS spectra of the U(IV) and Np(IV) complexes acquired as toluene solution with MC-fit (red), corresponding FT (right) and MS contributions (blue). Residual between MC fit and the experimental shown in the FT (green).

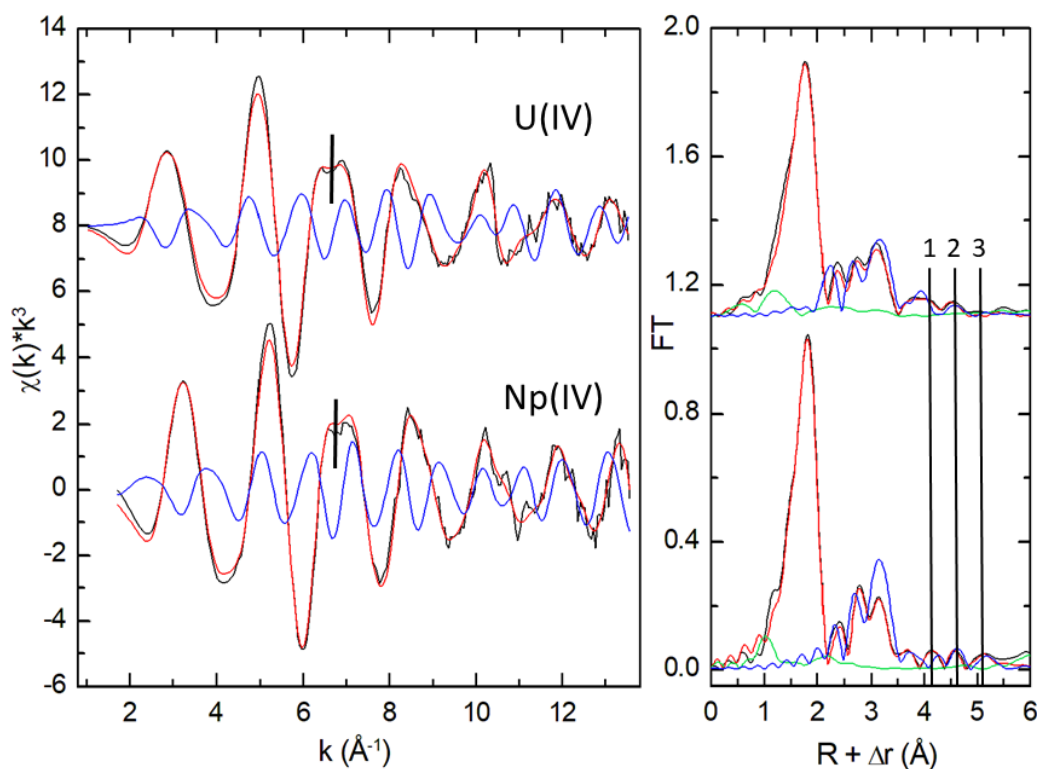Moreover, the average atomic positions gained by the MC simulations agree very well with the XRD structures (**Fig. S41)**, thus MC supports the findings of NMR. The analysis of the first and second moments of $n(r)$, i.e. r and σ^2, are given in **Table S13**. The structural parameter gained by the MC simulation are in favourable agreement with the shell fit results (**Table S12**) and they match the XRD structural data within the common error in determination of radial distances of 0.02 Å by EXAFS [28], except for the U–P interaction. Only for this interaction small structural deviations from the XRD structural data are observed. In the case of U(IV) the presence of the three isomers is supported by the decreased amplitude of the MS events above ~2.5 Å in the FT (**Fig. S40**), since the complex structures of **8**·CH_2Cl_2 and **8** are structurally more disordered than the complex structures of the complexes **8**·$3CH_3CN$·$4H_2O$ and **9**·$3CH_3CN$·$4H_2O$, respectively.
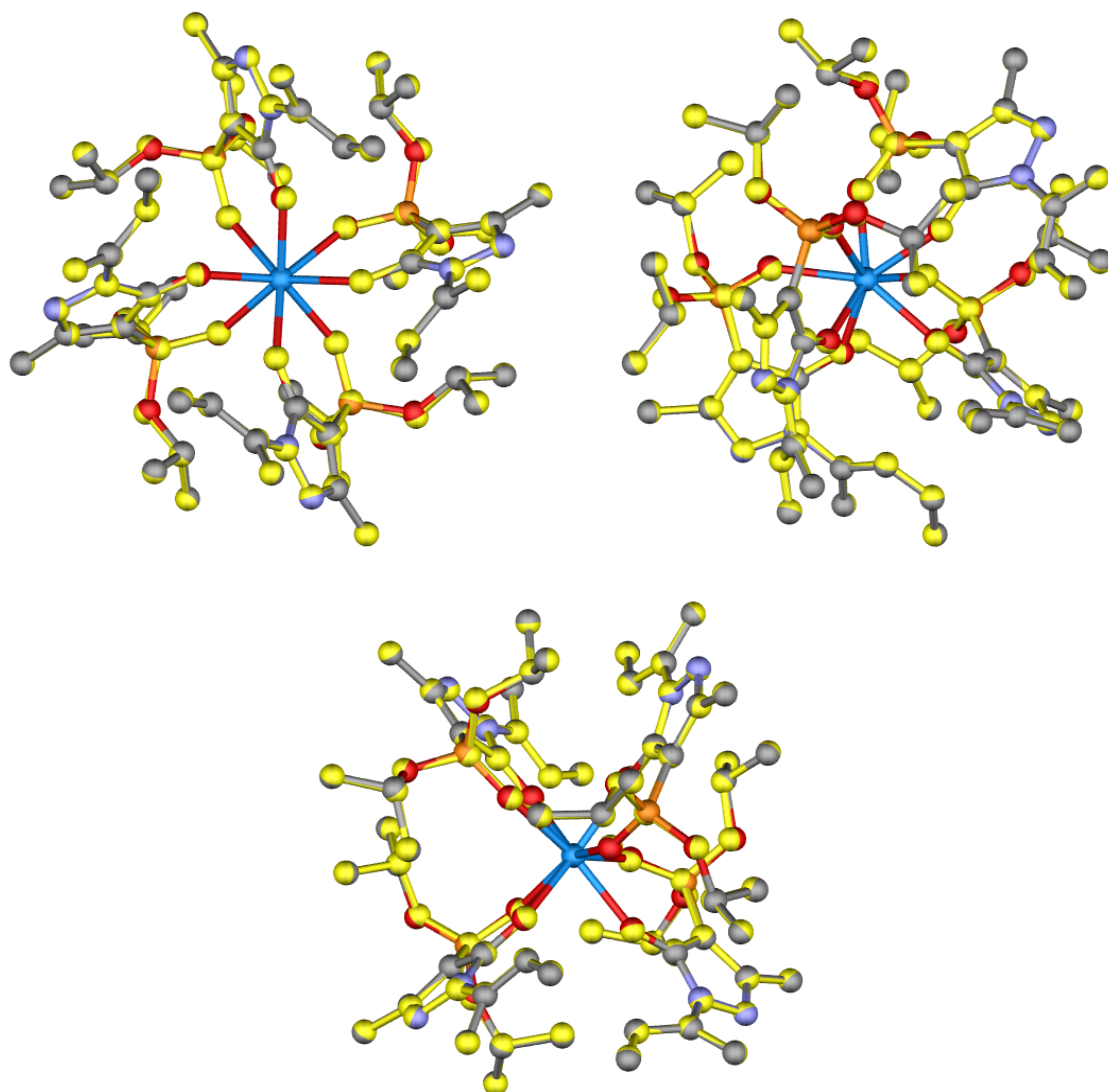
Fig. S41 Structure of **8**·3CH₃CN·4H₂O (upper left), **8**·CH₂Cl₂ (upper right), and **8** (lower middle) provided by XRD structural data (coloured) and the determined average atomic positions by using MC simulation (yellow). CH₃CN entity in **8**·3CH₃CN·4H₂O omitted for better visualization.

Table S13 Structural parameter of the U(IV) and Np(IV) complexes in toluene solution determined by the MC simulation.

Path/sample	n	r_{MC}/r_{XRD} /Å	Δr/Å	σ^2/Å^2	ΔE_0/Ev
8·3CH$_3$CN·4H$_2$O, 8·CH$_2$Cl$_2$, 8					
U–O1/2	8.0(8)	2.346(2)/2.347[a]	0.001	0.0064(3)	1.9
U–C1	4.0(7)	3.3747(4)/3.3832[a]	0.0085	0.007(2)	1.9
U–P	4.0(7)	3.6416(5)/3.6820[a]	0.0404	0.0039(7)	1.9
U–C2	4.2(6)	3.9830(8)/3.9694[a]	-0.0136	0.0052(8)	1.9
9·3CH$_3$CN·4H$_2$O					
Np–O1/2	8(1)	2.329(7)/2.338[a]	0.009	0.0066(4)	9.87
Np–C1	4.0(9)	3.353(2)/3.344	-0.009	0.006(2)	9.87
Np–P	4.0(7)	3.5894(4)/3.6364	0.0470	0.0039(9)	9.87
Np–C2	4.4(9)	3.938(3)/3.910	-0.028	0.004(1)	9.87

n – coordination number, r_{MC} and r_{XRD} – radial distances determined by MC simulation and XRD measurements, $\Delta r = r_{XRD} - r_{MC}$, [a] – calculated with average distances from XRD structural data of **8·3CH$_3$CN·4H$_2$O**, **8·CH$_2$Cl$_2$**, and **8**, respectively. σ^2 – Debye-Waller factor, ΔE_0 - shift in energy threshold.

Fourier filtering algorithm

As a third method we used a Fourier filtering algorithm (FFA), which was recently developed with the aim to compare experimental EXAFS spectra directly with theoretical EXAFS spectra calculated by FEFF using structures as gained by quantum chemical calculations or supplied by XRD measurements [29]. However, a direct comparison of the theoretical with the experimental spectrum is spoiled due to the fact that the amplitude function of the theoretical spectrum is not comparable with the experimental amplitude function since the σ^2 are unknown *a priory*.

In the first step of the FFA theoretical EXAFS spectra are calculated with the FEFF code basing on XRD structural data. In the case of the three mixed U(IV) isomers and with the XRD structural data of **8·3CH$_3$CN·4H$_2$O**, **8·CH$_2$Cl$_2$**, and **8** the resulting three theoretical spectra are averaged and weighted by a factor of 1/3, while for the Np(IV) complex the theoretical spectrum is calculated by using the XRD structural data from **9·3CH$_3$CN·4H$_2$O**. In order to adjust the theoretical EXAFS spectra in respect to the experimental Fermi level, the FEFF code allows the implementation of ΔE_0 provided by the shell fit.

By taking equation (5) and (6) into account, the phase and amplitude functions are available for the experimental (exp.) and the theoretical (theo.) EXAFS spectrum basing on the XRD structural data. Applying

$$\chi_{r1-r2}^{theo.\,*}(k) = \frac{A_{exp.}(k)}{A_{theo.}(k)} A_{theo.}(k) \sin(\Phi_{theo.}(k)) \tag{12}$$

the "experimental" EXAFS spectrum based on the XRD structural data ($\chi_{r1-r2}^{theo.\,*}(k)$) can be calculated, where equation (13) represents a simplification of equation (12).

$$\chi_{r1-r2}^{theo.\,*}(k) = A_{exp.}(k) \sin(\Phi_{theo.}(k)) \tag{13}$$

Thus, equation (13) enables the direct comparison between a theoretical and an experimental EXAFS spectrum, since the amplitude function of the theoretical spectrum is replaced with the amplitude function of the experimental EXAFS spectrum. The FT filtered r-range was 0.0 Å $\leq$ r $\leq$ 5.5 Å for both theoretical EXAFS spectra.
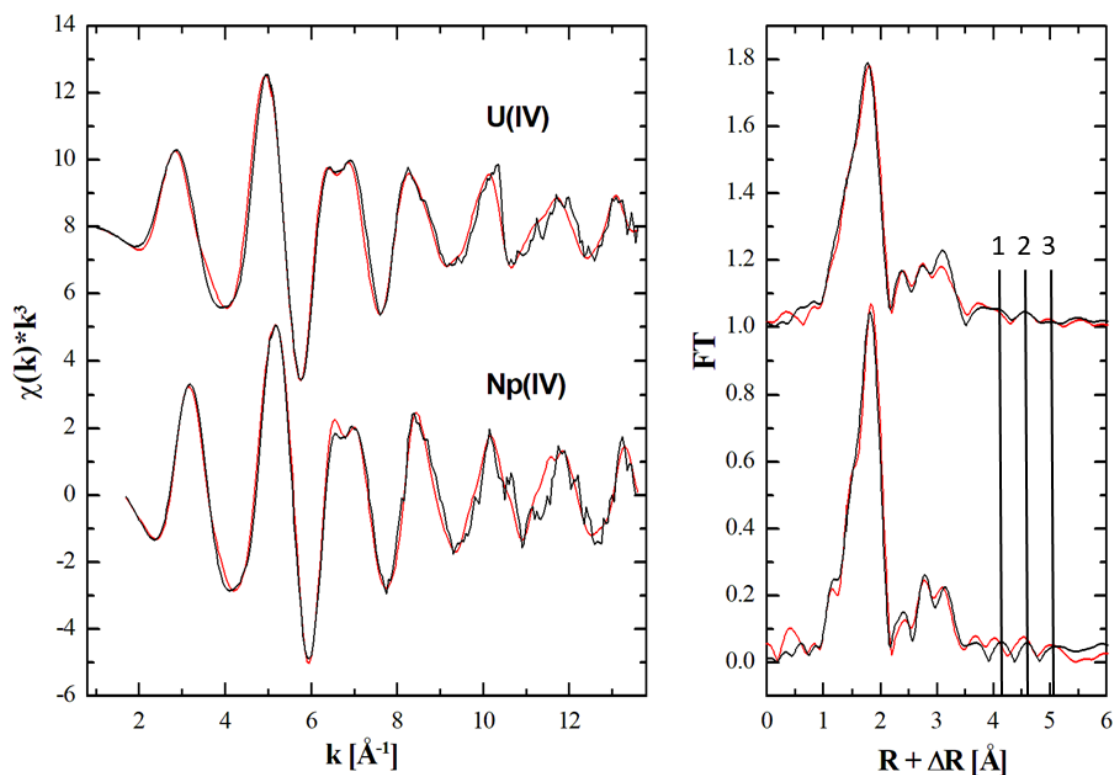
Fig. S42 Experimental (black) k^3-weighted EXAFS spectra of the U(IV) complexes and the Np(IV) complex acquired as toluene solution and the modified theoretical spectra (red (left)). Corresponding Fourier transform (FT) (right).

The result of the FFA is shown in **Fig. S42**. For both complexes in solution the theoretical EXAFS spectra are in very good agreement with the experimental EXAFS spectra. Moreover, the negative oscillation at 6.8 Å^{-1} and at 6.6 Å^{-1}, stemming from the typical MS paths U/Np–O1–N2 (1), U/Np–O1–C4 (2) and U/Np–C2–C3 (3) (FT in **Fig. S42**), is well reproduced. Thus, as a third independent method the FFA demonstrates again that the molecular structures of the complexes in solution match the XRD structural data.

References

1.   G. R. Fulmer, A. J. M. Miller, N. H. Sherden, H. E. Gottlieb, A. Nudelman, B. M. Stoltz, J. E. Bercaw and K. I. Goldberg, *Organometallics*, 2010, **29**, 2176-2179.
2.   J. Modranka, R. Jakubowski and T. Janecki, *Synlett*, 2014, **25**, 105-109.
3.   R. D. Hubbard and B. L. Miller, *J. Org. Chem.*, 1998, **63**, 4143-4146.
4.   B. Corbel, I. LHostisKervella and J. P. Haelters, *Synth. Commun.*, 1996, **26**, 2561-2568.
5.   M. A. Porai-Koshits and L. A. Aslanov, *J. Struct. Chem.*, 1972, **13**, 244-253.
6.   Bruker, *SAINT*, 2015.
7.   L. Krause, R. Herbst-Irmer, G. M. Sheldrick and D. Stalke, *J. Appl. Crystallogr.*, 2015, **48**, 3-10.
8.   G. Sheldrick, *Acta Crystallogr., Sect. C: Cryst. Struct. Commun.*, 2015, **71**, 3-8.
9.   C. B. Hübschle, G. M. Sheldrick and B. Dittrich, *J. Appl. Crystallogr.*, 2011, **44**, 1281-1284.
10.   CrysAlisPRO, *Oxford Diffraction /Agilent Technologies UK Ltd, Yarnton, England*.
11.   Bruker, *SMART. Bruker AXS Inc., Madison, Wisconsin, USA.*, 2007.
12.   Bruker, *SADABS. Bruker AXS Inc., Madison, Wisconsin, USA.*, 2001.

13.   O. V. Dolomanov, L. J. Bourhis, R. J. Gildea, J. A. K. Howard and H. Puschmann, *J. Appl. Crystallogr.*, 2009, **42**, 339-341.
14.   G. Sheldrick, *Acta Crystallogr. Sect. A: Found. Crystallogr.*, 2008, **64**, 112-122.
15.   W. Matz, N. Schell, G. Bernhard, F. Prokert, T. Reich, J. Claussner, W. Oehme, R. Schlenk, S. Dienel, H. Funke, F. Eichhorn, M. Betzl, D. Prohl, U. Strauch, G. Huttig, H. Krug, W. Neumann, V. Brendler, P. Reichel, M. A. Denecke and H. Nitsche, *J. Synchrot. Radiat.*, 1999, **6**, 1076-1085.
16.   G. N. George and I. J. Pickering, *SSRL, Stanford*, 1995.
17.   A. L. Ankudinov, B. Ravel, J. J. Rehr and S. D. Conradson, *Phys. Rev. B*, 1998, **58**, 7565-7576.
18.   W. K. Hastings, *Biometrika*, 1970, **57**, 97-109.
19.   N. Metropolis, A. W. Rosenbluth, M. N. Rosenbluth, A. H. Teller and E. Teller, *J. Chem. Phys.*, 1953, **21**, 1087-1092.
20.   M. Winterer, *J. Appl. Phys.*, 2000, **88**, 5635-5644.
21.   M. Winterer, R. Delaplane and R. McGreevy, *J. Appl. Crystallogr.*, 2002, **35**, 434-442.
22.   M. Winterer and F. Farges, *Phys. Scr.*, 2005, **T115**, 923-924.
23.   R. L. McGreevy, *J. Phys.: Condens. Matter*, 2001, **13**, R877-R913.
24.   J. Timoshenko, A. Kuzmin and J. Purans, *Comput. Phys. Commun.*, 2012, **183**, 1237-1245.
25.   S. J. Gurman and R. L. McGreevy, *J. Phys.: Condens. Matter*, 1990, **2**, 9463-9473.
26.   A. Rossberg and A. C. Scheinost, *Anal. Bioanal. Chem.*, 2005, **383**, 56-66.
27.   A. Rossberg and H. Funke, *J. Synchrot. Radiat.*, 2010, **17**, 280-288.
28.   G. G. Li, F. Bridges and C. H. Booth, *Physical Review B*, 1995, **52**, 6332-6348.
29.   F. Taube, B. Drobot, A. Rossberg, H. Foerstendorf, M. Acker, M. Patzschke, M. Trumm, S. Taut and T. Stumpf, *Inorganic Chemistry*, 2019, **58**, 368-381.